LAKEHEAD UNIVERSITY

MASTERS THESIS

UWB Localization for Autonomous Indoor Position Control of VTOL UAVs

---

Author:
Zeke SEDOR

Supervisor:
Dr. Abdelhamid TAYEBI

A thesis submitted in Partial fulfillment of the requirements for the degree of Master of Science

in the

Control Engineering
Department of Electrical and Computer Engineering

September 15, 2018

"*Research is what I'm doing when I don't know what I'm doing"*

Wernher von Braun

Abstract

As the popularity of quadrotor Vertical Take-Off and Landing (VTOL) Unmanned Aerial Vehicles (UAVs) grows, the need for reliable position estimation and control grows as well. Furthermore, with the size of these quadrotors decreasing and indoor use becoming possible, the need for indoor position estimation methods where Global Position System (GPS) measurements are unavailable, is a growing topic to which many solutions have been suggested. Herein a method fusing Ultra-Wideband (UWB) range measurements and Inertial Measurement Unit (IMU) measurements is implemented to produce reliable position and velocity estimates.

The position and velocity estimates from this system are then used as inputs to a position controller for the VTOL UAV system. Due to the underactuated nature of the system the position cannot be directly controlled, as such an intermediary control signal is defined. This intermediary control is used to determine the desired orientation and thrust of the UAV, which can then be controlled to achieve the desired position control. As the true orientation of the UAV is not directly measurable an observer using the available IMU measurements is utilized to estimate the orientation of the UAV.

Simulation and implementation results for the position estimation system, as well as the position control system are given.

Acknowledgements

I sincerely thank my supervisor, Dr. Abdelhamid Tayebi during my graduate studies at Lakehead University. He has proven to be an excellent supervisor and was always happy to share his considerable experience and knowledge, his inputs were always more than helpful. I want to thank him for his patience, support and guidance, and for instilling in me a genuine passion for control engineering.

I would also like to thank my fellow graduate Geordi McGrath for his input and insights into problems we both faced. Further I would like thank Thinh Ngo for his support in undergraduate studies and continued input into graduate studies, as well for continuing his education alongside me throughout College and University.

Contents

List of Figures

List of Tables

List of Abbreviations

UAV	**U**nmanned **A**erial **V**ehicle
VTOL	**V**ertical **T**ake **O**ff and **L**anding
UWB	**U**ltra **W**ide**B**and
GPS	**G**lobal **P**ositioning **S**ysytem
RADAR	**RA**dio **D**etection **A**nd **R**anging
FPU	**F**loating **P**oint **U**nit
KF	**K**alman **F**ilter
EKF	**E**xtended **K**alman **F**ilter
MEKF	**M**ultiplicative **E**xtended **K**alman **F**ilter
AEKF	**A**dditive **K**alman **F**ilter
DCM	**D**irection **C**osine **M**atrix
PID	**P**roportional **I**ntegral **D**erivative
LQR	**L**inear **Q**uadratic **R**egulator
PD	**P**roportional **D**erivative
CRLB	**C**ramer-**R**ao **L**ower **B**ound
ToF	**T**ime **o**f **F**light
TDoA	**T**ime **D**ifference **o**f **A**rrival
AGAS	**A**lmost **G**lobal **A**symptotic **S**tability
NED	**N**orth-**E**ast-**D**own
ECS	**E**lectronic **S**peed **C**ontroller
FFT	**F**ast **F**ourier **T**ransform
EMI	**E**lectro**M**agnetic **I**nterference
RSS	**R**eceived **S**ignal **S**trength
WLAN	**W**ireless **L**ocal **A**rea **N**etwork
USART	**U**niversal **S**ynchronous/**A**synchronous **R**eceiver/**T**ransmitter
SPI	**S**erial **P**eripheral **I**nterface
I^{2}C	**I**nter-**I**ntegrateted **C**ircuit
μC	**M**icro-**C**ontroller
APM	**A**rdu**P**ilot**M**ega
IGRF	**I**nternational **G**eomagnetic **R**eference **F**ield
RC	**R**adio **C**ontrol
PPM	**P**ulse **P**osition **M**odulation
PWM	**P**ulse **W**idth **M**odulation
AS	**A**symptotically **S**table

List of Symbols

$\mathcal{I}$	Inertial Reference Frame	
$\mathcal{B}$	Body Fixed Frame	
$\mathbf{R}$	Rotation matrix from $\{\mathcal{I}\}$ to $\{\mathcal{B}\}$	
Q	Quaternion for rotation from $\{\mathcal{I}\}$ to $\{\mathcal{B}\}$	
$\mathbf{p}$	Position of drone in $\mathcal{I}$	m
$\mathbf{v}$	Velocity of drone in $\mathcal{I}$	$\mathrm{m\,s^{-1}}$
$\mathbf{z}_i$	Position of i^{th} anchor in $\mathcal{I}$	m
Ω	Angular velocity in $\mathcal{B}$	$\mathrm{rad\,s^{-1}}$
$\boldsymbol{\tau}$	Rotational torque input	$\mathrm{N\,m}$
$\overline{\omega_i}$	Speed of i^{th} rotor	$\mathrm{rad\,s^{-1}}$
$\hat{T}_{prop}$	Propagation time of UWB message	s
d_i	distance between i^{th} anchor and target	m
$\mathcal{V}$	Lyapunov candidate function	

Dedicated to my parents. . .

Chapter 1

Introduction

Recently the multirotor Unmanned Arial Vehicle (UAV) has evolved into a versatile and popular flight platform that, due to its mechanical simplicity, lends itself well to many controls focused research areas. A multirotor UAV may have anywhere from two to eight rotors. The quadrotor platform as suggested by its name consists of four rotors and will be the study of this thesis. With a higher number of rotors the UAV will be more robust and capable of handing the failure of one or more rotors, but this failure mitigation is not the focus of this thesis. Research is being conducted on the mitigation of critical failure of one or more rotors on the quadrotor platform [1], as well research into single rotor UAVs which do not require a tail rotor is being conducted [2].
The simplicity of the quadrotor UAV is due to the fact that there are only four moving parts, *i.e.* the four outboard motors. These four motors are mounted sufficiently for away from the center of the quadrotor such that they can create large lever arms to induce large torques along any axis, this, along with the large thrust-to-weight ratio make the quadrotor a highly agile platform. This benefit coupled with ease of repair and maintenance due to minimal moving parts has led to quadrotors finding uses in a variety of fields ranging from residential package delivery [3] to surveilllance operations [4], as most of these applications can be deemed too dangerous for human interaction, or too costly to be completed by a human.

1.1 History

Quadrotor UAVs have been around for many years and were among the first successful Vertical Take-Off and Landing (VTOL) Vehicles. In the early stages these vehicles did not gain popularity as they were unrefined and unable to achieve suitable flight performance. Recent advances in low-cost sensors, and lightweight materials have revived interest in the quadrotor UAV as they make it possible to construct a relatively simple and cheap platform capable of robust performance. While once only built as military prototypes quadrotors are now found as everything from research platforms to military surveillance as well as toys. The first quadrotor UAV capable of carrying a human in flight was constructed in 1907 by the Bréguet brothers. The Bréguet-Richet Gyroplane No. 1 was constructed of heavy steel girders in a cross configuration, at the end of each arm was a rotor made from 4 cloth covered surfaces. At the center sat an 8 cylinder engine which drove the rotors through a system of belts and pullys, the craft weighed a loaded weight of 1274 lbs and was reported to achieve a maximum height of $5\mathrm{m}$. As there was no way to control this vehicle other than direct control of the motors it was very unstable. The next significant attempt at building a quadrotor was made by Etienne Oemichen in 1922. His most successful vehicle was the Oemichen No. 2, this machine had 4 rotors with 8 propellers powered by one engine, this machine offered some form of stability and controllability and made

thousands of successful flights [5]. As well in 1922 the US army made its first serious attempt to develop a quadrotor aircraft. Dr. George de Bothezat designed a quadrotor vehicle in a cross configuration with 6 propellers at the end of each arm, this aircraft was only able to acheive a maximum altitude of $5\mathrm{m}$ far from the $100\mathrm{m}$ goal and as such was abandoned [6]. One of the greatest contributions to the quadrotor aircraft came in the $1950\mathrm{s}$ by D.H. Kaplan. His design was more refined that the others and utilized the differential thrust inputs for attitude control that is still utilized today. This project was as well abandoned due to lack of interest, but the effectiveness of the differential thrust method has lived on in smaller unmanned quadrotor UAVs. These smaller quadrotors have taken over as they eliminate the large trust requirements of a large manned quadrotor, as well as the difficulties encountered due to the fluid motions that a "man" produces. One of the first modern small quadrotor UAVs was the Draganflyer, built in Canada by RCToys [7], although intended as a toy, it showed that quadrotor technology could be realized on low cost mass produced platform.

1.2 Motivation

The dynamics of a quadrotor UAV are well approximated by a set of nonlinear differential equations, making them an excellent platform for research in nonlinear control design. This has led to the development of many controls-focused indoor testbeds wherein equipment is used to gather precise information for state estimation. These testbeds are often equipped with motion capture systems some such systems are; MITs' Raven [8], or ETH Zurich Flying Machine Arena [9]. The measurement precision available along with the controlled environment allows for the isolation of individual research questions. As these testbeds are often extremely expensive, one goal of this thesis is to create a reliable, precise, inexpensive, test environment for indoor UAV navigation. To this end a UWB sensor array is implemented for the re-creation of both position and linear velocity of the quadrotor UAV. Futher this system will be exploited as a precise, computationally efficient system that can be used for the needs of position control in GPS denied environments. For these environments there exist position control schemes that rely on complex vision systems, other forms of Radio Detection And Ranging (RADAR) as well as direct IMU integrations see [10] and references therein. The system proposed utilizing Ultra Wide Band (UWB) measurements will be shown to work well in these environments, at a minimal cost.

1.3 Research Challenges

As the quadrotor is a naturally unstable nonlinear system, state estimation and control can become challenging for real world systems where sensor noise and biases heavily affect the system. Further for this project as no UWB system was present before research began one must be developed. Some main challenges are listed below;

- The real world system consists of low cost sensors that are affected by noise and sensor biases, which will need to be carefully handled in the estimation process
- Testing is completed in an indoor environment where obtaining an accurate measurement of the earths magnetic field will be near impossible
- The rotational dynamic estimations and control algorithms will be implemented on a low cost $16\mathrm{MHz}$ microcontroller with no Floating Point Unit (FPU)

- The UWB system must be designed and implemented, in a way that it can be added to the existing system easily
- The UWB sample rate will be limited due to time consuming message relays
- The quadrotor platform is inherently dangerous to be around due to the high speed spinning propellers

Chapter 2

Literature Review

2.1 Attitude Estimation

Before the attitude of a UAV can be controlled it must first be estimated. As this orientation is not directly measurable, three sensors are often utilized to estimate its value, a magnetometer, accelerometer and gyroscope. The accelerometer provides a body referenced acceleration, the magnetometer provides a body referenced earth magnetic field measurement, and the gyroscope provides the body referenced angular velocity. A simple yet very ineffective method of determining the attitude of the UAV would be a direct integration of the gyroscope measurements. However, this approach is ineffective as it leads to a drift over time in the attitude estimate due to the inherent gyro bias. Another ineffective method of attitude estimation is one that relies solely on inertial vector measurements such as those proposed in [11]–[14]. Again, this approach, referred to as static attitude determination, is ineffective in the presence of measurement noise.

It is evident that sensor noise causes a large problem when trying to estimate the attitude of a rigid body and as such a filtering technique must be implemented. Filtering techniques combine the rigid body kinematic model and IMU measurements to produce a good estimate of the attitude of the rigid body. One such technique is the Kalman Filter (KF) [15], which consists of two steps; first the current state estimates are updated using the previous states and dynamical model of the system, next these estimates are further updated using weighted noisy sensor measurements. The states estimated are then utilized in the next cycle. The KF was originally designed for linear systems and does not apply directly to nonlinear systems, A common approach the deals with noisy nonlinear systems is the known as the Extended Kalman Filter (EKF). This approach is not guaranteed to provide good performance when the initial errors are large, as it relies on system linearization. Further developments led to the Multiplicative [16] and Additive [17] Kalman Filters (MEKF and AEKF respectively). Although these methods provide acceptable attitude estimation, they are computationally expensive and as such are not often implemented on small quadrotor UAVs, where processing power is limited.

A computationally efficient alternative which relies upon the nonlinear dynamics of the system may instead be implemented. Many such complementary filters can be found in the literature [18]–[21], some of which utilize the full Direction Cosine Matrix (DCM) [20], [21], and others relying only on the unit quaternion representation [18], [19]. All of these nonlinear observers utilize the assumption that the accelerometer measures the gravity vector in the body frame, which is only valid under low translational acceleration. If the UAV undergoes a large translational acceleration, the estimation from these observers will become unreliable. To overcome this problem, nonlinear observers that also include the translational velocity [22], [23], determined from say a GPS or UWB array, are utilized for UAVs expected to go through some high acceleration movements. These observers utilize an additional velocity estimate function in the

innovation term of the observer, which is governed by another estimation law derived from velocity measurements and accerometer measurements. A problem with any of these observers is that the earth's magnetic field becomes very difficult to measure once the motors of the UAV are activated, as these produce their own magnetic field further corrupting the measured vector. This problem can be mitigated with a calibration technique such as one described in [24]. Further through the vector decoupling strategy proposed with the observers of [18], [25], this coupling problem can be minimized.

2.2 UAV Attitude Control

Attitude control consists of designing an appropriate torque input,using the estimated attitude and measured angular velocity, to maintain the true attitude at a desired one. For the autonomous control of a quadrotor UAV this is an important step in the design procedure, and many approaches have been proposed in the literature, see for example [26]–[28] and the references therein for more information. Linear approaches such as the Proportional-Integral-Derivative (PID) [29] or Linear-Quadratic-regulator (LQR) [30] are often used in practice. The drawback of these approaches is that they are designed around a linearized operating point and far deviations from this point will cause the system to destabilize. A method which provides a larger region of stability is one wherein a outer loop is defined for the attitude control and an inner loop for the body angular rate control [9], [31]. The drawback of this type of control is the difficulty presented when trying to prove full closed loop stability. Finally, nonlinear control techniques such as; feedback linearization, backstepping, and sliding mode control are proposed in [32]–[34]. Although these methods provide good solutions to the attitude control problem, they are all model dependent and as such certain parameters of the quadrotor UAV must be known. A Proportional-Derivative (PD) like controller based upon quaternon feedback is proposed in [35]. This controller requires no knowledge of the system and can provide Global Asymptotic Stability (GAS), and as such this approach is chosen for attitude control in this thesis.

2.3 Localization Using UWB Measurements

UWB systems are wireless communication systems that occupy a bandwidth greater than 25% of the centre frequency or an absolute bandwidth of 500MHz or greater [36]. These devices are then suited very well for time based ranging algorithms as the lower bound on the variance of the measurement (Cramer-Rao Lower Bound) is a function that is inversely proportional to the effective bandwidth of the ranging channel [37]. Further, due to the high bandwidth of UWB signals they occupy both high and low frequencies providing these signals great ability to penetrate solid objects [38].

For time based localization two main methods exist; Time of Flight (ToF), and Time Difference of Arrival (TDoA) [38]. For a TDoA scheme all anchor nodes must share a synchronized clock [39], but work is being done to determine a method where a synchronized clock is not required [40]. A TDoA scheme is best suited for systems wherein multiple targets exist, as each target broadcasts a message to all anchors and the time difference between reception at each anchor compared to a reference anchor is used to calculate the position of the target.

As only one target will be tracked a TDoA method is unnecessarily complicated, so a ToF method is implemented. There exist several different ways to determine the position of a target

from direct/geometric methods [39] or statistical methods [38], [41], [42], as well as from iterative methods that utilize the distance measurements [43]. In the present thesis, a direct method is utilized.

2.4 UAV Position Control

Autonomous flight of the quadrotor UAV is now possible as both the attitude and position have been estimated. Much research with respect to position control of the quadrotor has been done and many differing methods described [43]–[51]. These methods range from the utilization of neural networks, feedback linearization, sliding mode control, to hierarchical control design with inner and outer loop control strategies. Methods of interest include [49], wherein a framework is laid out for separate position and attitude control design which if certain conditions are fufilled, Almost Global Asymptotic Stability (AGAS) is guaranteed. Position controllers of this class are often utilized due to their simplicity and configurability. Further, a partial backstepping approach has been propsed in [48], where the desired angular velocity and system thrust are designed based upon position and velocity errors. This controller relies upon a fast convergence of the true angular velocity to the desired angular velocity. A complete backstepping approach, generating the appropriate thrust and torque inputs has been proposed for the position control of a VTOL-UAV in [51]. The above mentioned papers assume the position and linear velocity of the VTOL-UAV are are available for feedback without sensor specification.

Systems that utilize UWB signals for UAV position control are described in [50], [52]. In [52], a method is proposed where accelerometer and gyroscope data is fused with UWB measurements through an EKF to produce a reliable position estimate. In [50], a Gauss Newton method is utilized to determine the position from UWB measurements. The focus for the position controllers described later will be based on the work of [49] and [51].

2.5 Thesis Contributions

The thesis contributions are as follows:

- A method for determining the optimal position for ‘N’ anchor positions based on a covariance matrix based cost function is described in Chapter 6
- A method for determining the optimal number of anchor nodes though a dual minimization is proposed in Chapter 6
- A partial state observer utilizing UWB measurements and accelerometer data is given in Chapter 6
- A simple position tracking controller utulizing UWB position measurements is shown in Chapter 8 based on the method described in [49]
- A rigorous position tracking controller similar to the work of [23] is described in Chapter 9

Chapter 3

Attitude Representations

When describing the motion of a rigid body in free space it is necessary to obtain its attitude, which consists of the orientation frame $\mathcal{B}$, attached to the UAV, with respect to the inertial frame $\mathcal{I}$. There exist different ways to represent the attitude of a rigid body [53], but only three will be discussed in the following; the direction cosine matrix, the Euler parameters, and the unit quaternion parametrizations.

3.1 Direction Cosine Matrix (Rotation Matrix)

The rotation matrix is the most common way of representing the attitude of a rigid body. It is an over parametrization as nine parameters are needed to describe a rotation, but this comes with the benefit of no singularities and uniqueness at any rotation. The rotation matrix belongs to the special orthogonal group $SO(3)$ defined as

$$SO(3) = \{\mathbf{R} \in \mathbb{R}^{3\times 3} \mid \mathbf{R}\mathbf{R}^T = I_{3\times 3},\, \det(\mathbf{R}) = 1\}.$$

This matrix is obtained through the projection of the axes of frame $\mathcal{B}$ onto the frame $\mathcal{I}$ as follows:

$${}^{\mathcal{I}}\mathbf{R}_{\mathcal{B}} = \begin{pmatrix} \hat{x}_{\mathcal{B}} \cdot \hat{x}_{\mathcal{I}} & \hat{x}_{\mathcal{B}} \cdot \hat{y}_{\mathcal{I}} & \hat{x}_{\mathcal{B}} \cdot \hat{z}_{\mathcal{I}} \\ \hat{y}_{\mathcal{B}} \cdot \hat{x}_{\mathcal{I}} & \hat{y}_{\mathcal{B}} \cdot \hat{y}_{\mathcal{I}} & \hat{y}_{\mathcal{B}} \cdot \hat{z}_{\mathcal{I}} \\ \hat{z}_{\mathcal{B}} \cdot \hat{x}_{\mathcal{I}} & \hat{z}_{\mathcal{B}} \cdot \hat{y}_{\mathcal{I}} & \hat{z}_{\mathcal{B}} \cdot \hat{z}_{\mathcal{I}} \end{pmatrix}. \tag{3.1}$$

This matrix can now be used to express vectors from one frame in the other frame, *e.g.,* the accelerometer measurement $a_{\mathcal{B}} \in \mathbb{R}^3$ can then be brought from the body-attached frame to the inertial frame as follows

$$a_{\mathcal{I}} = \mathbf{R} a_{\mathcal{B}}.$$

.

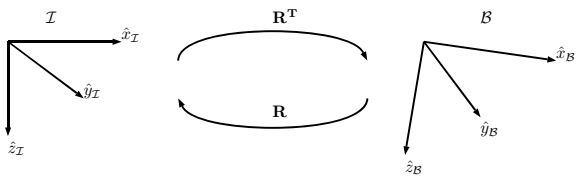

FIGURE 3.1: Rotation of $\mathcal{B}$ with respect to $\mathcal{I}$

3.2 Euler Angles

The most intuitive method for attitude parametrization is that of the Euler angles. This method parametrizes the attitude with three angles, (ϕ, θ, ψ) known as the roll, pitch and yaw. These angles represent three successive rotations about the x_h, y_h and z_h axes. A rotation about the $\hat{x}$, $\hat{y}$, and the $\hat{z}$ axis are shown below

$$\begin{aligned}
\mathbf{R}_{\hat{x}}(\phi) &= \begin{pmatrix} 1 & 0 & 0 \\ 0 & \cos\phi & -\sin\phi \\ 0 & \sin\phi & \cos\phi \end{pmatrix} \\
\mathbf{R}_{\hat{y}}(\theta) &= \begin{pmatrix} \cos\theta & 0 & \sin\theta \\ 0 & 1 & 0 \\ -\sin\theta & 0 & \cos\theta \end{pmatrix} \\
\mathbf{R}_{\hat{z}}(\psi) &= \begin{pmatrix} \cos\psi & -\sin\psi & 0 \\ \sin\psi & \cos\psi & 0 \\ 0 & 0 & 1 \end{pmatrix}.
\end{aligned}$$

As the orthogonal base vector is altered after each rotation, it is possible to represent any orientation by rotating about only two axes. This is only true if successive rotations do not take place about the same axis. For example performing 3 rotations in the $z - x - z$ order results in the following rotation matrix.

$$\mathbf{R} = \mathbf{R}_{\hat{z}}(\psi)\mathbf{R}_{\hat{y}}(\theta)\mathbf{R}_{\hat{z}}(\phi) = \begin{pmatrix} c\phi c\psi - s\phi s\psi c\theta & -c\phi s\psi c\theta - s\phi c\psi & s\psi s\theta \\ s\phi c\psi c\theta + c\phi s\psi & c\phi c\psi c\theta - s\phi s\psi & -c\psi s\theta \\ s\phi s\theta & c\phi s\theta & c\theta \end{pmatrix}, \tag{3.2}$$

for small rotations about $\mathbf{R} = \mathbf{I}_{3\times 3}$, this matrix is given as

$$\mathbf{R} = \begin{pmatrix} 1 & -\psi - \phi & 0 \\ \phi + \psi & 1 & -\theta \\ 0 & \theta & 1 \end{pmatrix}. \tag{3.3}$$

From this, it is evident that, it is impossible to represent a small rotation about the $\hat{y}$ axis, from the orientation $\mathbf{R} = \mathbf{I}_{3\times 3}$. This problem is known as gimbal lock, and causes the rotation matrix to undergo a large change in an infinitesimal amount of time, this issue arises for rotations of $\pm\pi$ about the $\hat{y}$ axis as well.

3.3 Unit Quaternion Representation

The unit quaternion representation of an attitude is a four element parametrization defined on the space

$$\mathbb{Q} = \{Q \in \mathbb{R}^4 \mid |Q| = 1\},$$

as

$$Q = \begin{pmatrix} q_0 \\ q_1 \\ q_2 \\ q_3 \end{pmatrix} = \begin{pmatrix} \cos(\gamma/2) \\ \sin(\gamma/2)\hat{k}_1 \\ \sin(\gamma/2)\hat{k}_2 \\ \sin(\gamma/2)\hat{k}_3 \end{pmatrix} = \begin{pmatrix} q_0 \\ q \end{pmatrix}, \tag{3.4}$$

where γ is a rotation about the unit vector $\mathbf{k} := [\hat{k}_1 \ \hat{k}_2 \ \hat{k}_3]^T$. As the name indicates the unit quaternion follows the restriction $q_0^2 + q^T q = 1$. The composition of two rotations described by two quaternions Q_1 and Q_2 is given by

$$Q_1 \odot Q_2 = \begin{pmatrix} q_{0_1} q_{0_2} - q_1^T q_2 \\ q_{0_1} q_2 + q_{0_2} q_1 + S(q_1) q_2 \end{pmatrix}, \tag{3.5}$$

The unit quaternion ($Q_I = [1\ 0\ 0\ 0]^T$) is the identity element, such that

$$Q \odot Q^{-1} = Q^{-1} \odot Q = \begin{pmatrix} 1 \\ 0 \\ 0 \\ 0 \end{pmatrix},$$

where

$$Q^{-1} = \begin{pmatrix} q_0 \\ -q \end{pmatrix}. \tag{3.6}$$

For a given vector $v \in \mathbb{R}^3$, where $v_{\mathcal{I}} = \mathbf{R} v_{\mathcal{B}}$ one can write

$$\overline{v}_{\mathcal{I}} = Q \odot \overline{v}_{\mathcal{B}} \odot Q^{-1}, \tag{3.7}$$

where Q is the unit-quaternion associated with the rotation matrix $\mathbf{R}$ and $\overline{v}_{\mathcal{I}} = \begin{bmatrix} 0 & v_{\mathcal{I}}^T \end{bmatrix}^T$ and $\overline{v}_{\mathcal{B}} = \begin{bmatrix} 0 & v_{\mathcal{B}}^T \end{bmatrix}^T$. Furthermore, the nine element rotation matrix can be can be expressed with the unit quaternion through the Rodriguez map $\mathcal{R}(Q) : \mathbb{Q} \mapsto SO(3)$

$$\mathcal{R}(Q) = \mathbf{I}_{3\times 3} + 2 q_0 S(q) + S(q)^2, \tag{3.8}$$

with $S(q)$ being the skew-symmetric matrix on $\mathbb{R}^3$ defined as

$$S(q) := \begin{bmatrix} 0 & -q_3 & q_2 \\ q_3 & 0 & -q_1 \\ -q_2 & q_1 & 0 \end{bmatrix}. \tag{3.9}$$

The unit quaternion parametrization only requires a 4-element vector, making it computationally efficient for real world applications. It comes with the drawback that it is a non-unique representation of the attitude, since $\mathbf{R}$ can be represented by either Q or $-Q$ as evident from eq. 3.8. This ambiguity can be avoided by choosing the appropriate equations of motion as shown in [26].

Chapter 4

Mathematical Model

4.1 Model Definition

The motion of a quadrotor UAV can be broken into two main categories: translational motion, and rotational motion. The translational dynamics are given by

$$\sum_1 := \left\{ \begin{array}{l} \dot{\mathbf{p}} = \mathbf{v} \\ \dot{\mathbf{v}} = g\hat{\mathbf{e}}_3 - \frac{\mathcal{T}}{m}\mathbf{R}^T\hat{\mathbf{e}}_3, \end{array} \right. \tag{4.1}$$

where $\hat{\mathbf{e}}_3 := [0\ 0\ 1]^T$ and $\mathbf{p}$ and $\mathbf{v}$ are respectively the position and linear velocity of the center of mass of the rigid body expressed in the inertial frame $\mathcal{I}$. The mass of the UAV is denoted m, the thrust by $\mathcal{T}$. The matrix $\mathbf{R}$ describes the rotation of the body attached frame $\mathcal{B}$ with respect to the inertial frame $\mathcal{I}$. The rotational dynamics of the rigid body are given by

$$\sum_2 := \left\{ \begin{array}{l} \dot{Q} = \frac{1}{2}\left[\begin{array}{c} -q^T \\ q_o\mathbf{I}_{3\times 3} + S(q) \end{array} \right]\Omega \\ I_b\dot{\Omega} = -S(\Omega)I_b\Omega + \boldsymbol{\tau}_a \end{array} \right. , \tag{4.2}$$

where Ω is the rigid body angular velocity espressed in the body-attached frame $\mathcal{B}$, $Q := [q_o\ q]$ is the unit-quaternion associated to the rotation matrix $\mathbf{R}$, I_b is the inertial matrix of the rigid body with respect to the body-attached frame, and $\boldsymbol{\tau}_a$ is the control torque vector applied to the rigid body. From figure. 4.1 it is possible to define the reaction torques $f_i,\ i \in \{1,2,3,4\}$, produced by the 4 rotors as

$$\begin{aligned} f_1 &:= \frac{db}{\sqrt{2}}\left(\overline{w}_1^2 + \overline{w}_2^2\right) \\ f_2 &:= \frac{db}{\sqrt{2}}\left(\overline{w}_2^2 + \overline{w}_3^2\right) \\ f_3 &:= \frac{db}{\sqrt{2}}\left(\overline{w}_3^2 + \overline{w}_4^2\right) \\ f_4 &:= \frac{db}{\sqrt{2}}\left(\overline{w}_4^2 + \overline{w}_1^2\right). \end{aligned} \tag{4.3}$$

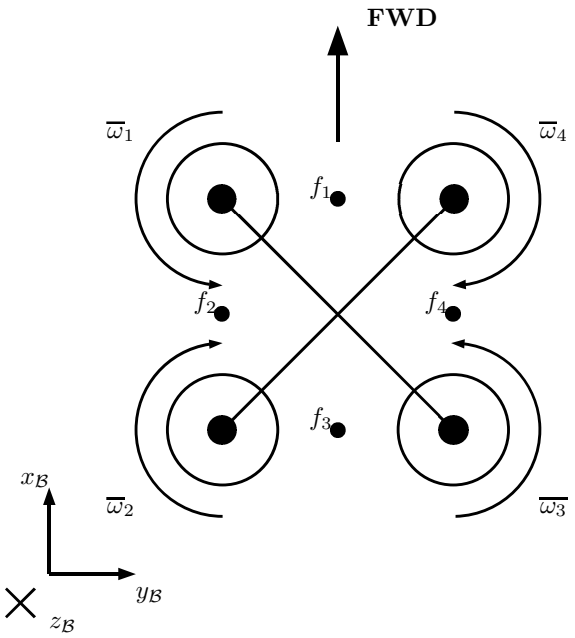

FIGURE 4.1: Quadrotor diagram

These reactive torques can then be used to define torques around the body-attached axes as well as the total system thrust $\mathcal{T}$ as

$$\begin{aligned} \mathcal{T} &:= \frac{b}{2}\sum_{i=1}^{4} f_i \\ \boldsymbol{\tau}_a &:= \begin{bmatrix} f_2 - f_4 \\ f_1 - f_3 \\ \kappa(\overline{\omega}_1^2 + \overline{\omega}_3^2 - \overline{\omega}_2^2 - \overline{\omega}_4^2) \end{bmatrix}. \end{aligned} \tag{4.4}$$

Where d is the distance between the rotor and center of mass, b and κ are the propeller constants and $\overline{\omega}_i$, $i = 1 \dots 4$, is the speed of propellor i. These torques can be related to rotor speed through

$$\mathbb{T} := \begin{bmatrix} \mathcal{T} & \tau_1 & \tau_2 & \tau_3 \end{bmatrix}^T = \mathbf{M} \begin{bmatrix} \overline{\omega}_1^2 & \overline{\omega}_2^2 & \overline{\omega}_3^2 & \overline{\omega}_4^2 \end{bmatrix}^T = \mathbf{M}\overline{\boldsymbol{\omega}}, \tag{4.5}$$

with

$$\mathbf{M} := \begin{bmatrix} b & b & b & b \\ -\frac{db}{\sqrt{2}} & \frac{db}{\sqrt{2}} & \frac{db}{\sqrt{2}} & -\frac{db}{\sqrt{2}} \\ \frac{db}{\sqrt{2}} & \frac{db}{\sqrt{2}} & -\frac{db}{\sqrt{2}} & -\frac{db}{\sqrt{2}} \\ \kappa & \kappa & \kappa & \kappa \end{bmatrix}. \tag{4.6}$$

Given the thrust and torques, one can obtain the rotor speeds as follows:

$$\overline{\boldsymbol{\omega}} = \mathbf{M}^{-1}\mathbb{T}.$$

For this system, there is no need to include the dynamic equations for the DC outrunner motors as the true rotor speed is regulated by the Electronic Speed Controllers (ESCs).

A depiction of each type of rotation motion is shown in Fig. 4.2. The roll motion is achieved

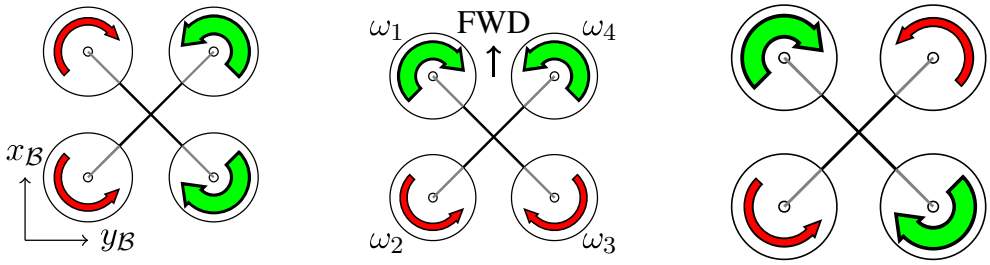

(A) Roll (B) Pitch (C) Yaw

FIGURE 4.2: Rotor speeds related to rotational motion

through the differential of $\overline{w}_{1,2}$ and $\overline{w}_{3,4}$, pitch motion is achieved through the differential of $\overline{w}_{1,4}$ and $\overline{w}_{2,3}$, and yaw action is achieved through the differential of $\overline{w}_{1,3}$ and $\overline{w}_{2,4}$. By configuring the quadrotor in an 'X' configuration all four rotors are required to create any form of rotational motion, this is desirable over a cross configuration where only two rotors are used for roll or pitch motions. This configuration will help create a more stable platform while also increasing available torque around both $x_{\mathcal{B}}$ and $y_{\mathcal{B}}$ axes by a factor of $\sqrt{2}$.

The complete dynamics of the quadrotor from position to rotor velocities are given by

$$\begin{aligned}
\dot{\mathbf{p}} &= \mathbf{v} \\
\dot{\mathbf{v}} &= g\hat{\mathbf{e}}_3 - \frac{\mathcal{T}}{m}\mathbf{R}^T\hat{\mathbf{e}}_3 \\
\dot{Q} &= \frac{1}{2}\begin{bmatrix} -q^T \\ q_o\mathbb{I}_{3\times 3} + S(q) \end{bmatrix}\Omega \\
I_b\dot{\Omega} &= -S(\Omega)I_b\Omega + \boldsymbol{\tau}_a \\
\overline{\boldsymbol{\omega}} &= \mathbf{M}^{-1}\mathbb{T}.
\end{aligned} \tag{4.7}$$

Symbol	Definition
m	Mass of airframe
g	Gravity constant $9.81m/s^2$
$\mathcal{T}$	Thrust applied by rotors
$\mathbf{p} = [x_{\mathcal{I}},\ y_{\mathcal{I}},\ z_{\mathcal{I}}]^T$	Inertial referenced position
$\mathbf{R}^T$	Rotation from $\mathcal{I}$ to $\mathcal{B}$
S(·)	Skew-symmetric matrix
Ω	Body referenced angular velocity
$\mathbf{I}_{\times 3}$	3×3 identity matrix
$\mathbf{I}_b$	Body referenced inertial matrix of airframe
$\boldsymbol{\tau}_a$	Applied airframe torques
$\overline{\omega}_i$	Speed of rotor i
b	Proportionality constant relating thrust to rotor velocity
d	Distance from body referenced origin to rotor
κ	Proportionality constant relating rotor reactive torque to rotor velocity

TABLE 4.1: Mathematical model parameters

Symbol	Parameter	Value
C_T	Thrust coefficient	0.1223
C_P	Power coefficient	0.0494
ρ	Air density (15 °C)	$1.225\,\mathrm{kg/m^3}$
D	Diameter of rotor	$0.2540\,\mathrm{m}$
n	Speed of rotor	$\mathrm{rev/s}$

TABLE 4.2: Propeller aerodynamic coefficients

4.2 Parameters Identification

4.2.1 Mass

The mass of the quadrotor is found using a digital scale, the mass is found to be $1.342\,\mathrm{kg}$.

4.2.2 Propeller Aerodynamics

The steady-state thrust generated by a propeller while hovering (*i.e.* negligable translational motion) in free air can be modelled using momentum theory [54] as

$$f_i = C_T \rho n^2 D^4 = b\overline{\omega}_i^2, \tag{4.8}$$

and the reactive torque generated by this same rotor is given as

$$Q_i = \frac{C_P \rho n^2 D^5}{2\pi} = \kappa \overline{\omega}_i^2, \tag{4.9}$$

with variables listed in Table 4.2. The values are calculated based on the propeller values: diameter = 10in, pitch = $4.7\mathrm{in/rev}$. Using these values, it is then possible to determine the propeller thrust and torque coefficients, respectively, as

$$\begin{aligned} b &= \frac{C_T \rho D^4}{4\pi^2} = 1.5796 \times 10^{-5} \\ \kappa &= \frac{C_P \rho D^4}{8\pi^3} = 2.5792 \times 10^{-7}, \end{aligned} \tag{4.10}$$

4.2.3 Inertia Matrix

For the purposes of this experiment, the drone is assumed to have a diagonal inertia matrix, which is a reasonable assumption as the drone is symmetrical about the z-axis. Under this assumption, it is possible to utilze the method described in [55] to determine the moments of inertia around the three axes. This is accomplished by hanging the drone from a fixed point and allowing the drone to swing freely about the desired axis. The motion can be described using the Lagrangian approach.
The kinetic energy is given by

$$T = \frac{1}{2} I_{interest} \dot{\theta}^2 + \frac{1}{2} m l^2 \dot{\theta}^2,$$

Parameter	Description	Value
m	Mass	$1.342\,\mathrm{kg}$
d	Distance to rotor	$0.259\,\mathrm{m}$
b	Thrust coefficient	$1.5796 \times 10^{-5}\,\mathrm{N \cdot s^2/rad^2}$
κ	Reactive torque coefficient	$2.5792 \times 10^{-7}\,\mathrm{N \cdot m \cdot s^2/rad^2}$
$I_{x_\mathcal{B}}$	Roll inertia	$0.0147\,\mathrm{kg \cdot m^2}$
$I_{y_\mathcal{B}}$	Pitch inertia	$0.0126\,\mathrm{kg \cdot m^2}$
$I_{z_\mathcal{B}}$	Yaw inertia	$0.0231\,\mathrm{kg \cdot m^2}$

TABLE 4.3: Quadrotor physical parameters

with potential energy

$$V = mgl(1 - \cos\theta),$$

which gives the Lagrangian

$$L = T - V = \frac{1}{2} I_{interest}\dot{\theta}^2 + \frac{1}{2} ml^2\dot{\theta}^2 - mgl(1 - \cos\theta).$$

Using the Euler-Largrange equation

$$\frac{d}{dt}\left(\frac{\delta L}{\delta \dot{\theta}}\right) - \frac{\delta L}{\delta \theta} = 0,$$

the second order dynamics are determined as

$$\left(I_{interest} + ml^2\right)\ddot{\theta} + mgl\sin\theta = 0.$$

Under the small angle approximation (*i.e.* $\sin\theta \approx \theta$), this can be rewritten as

$$\left(I_{interest} + ml^2\right)\ddot{\theta} + mgl\theta = 0, \tag{4.11}$$

from which the natural frequency $\omega_{n_{interest}}$ is determined

$$\omega_{n_{interest}} = \sqrt{\frac{mgl}{I_{interest} + ml^2}}, \tag{4.12}$$

which can then be re-arranged to determine $I_{interest}$ from the value of $\omega_{n_{interest}}$ determined by experiments

$$I_{interest} = \frac{mgl}{\omega^2_{n_{interest}}} - ml^2. \tag{4.13}$$

Results from the Fast-Fourier Transforms (FFT) are used to determine $\omega_{n_{interest}}$. This value is utilized in eq. 4.13 to determine the values for I_x, I_y, I_z, which are are given in Table4.3.

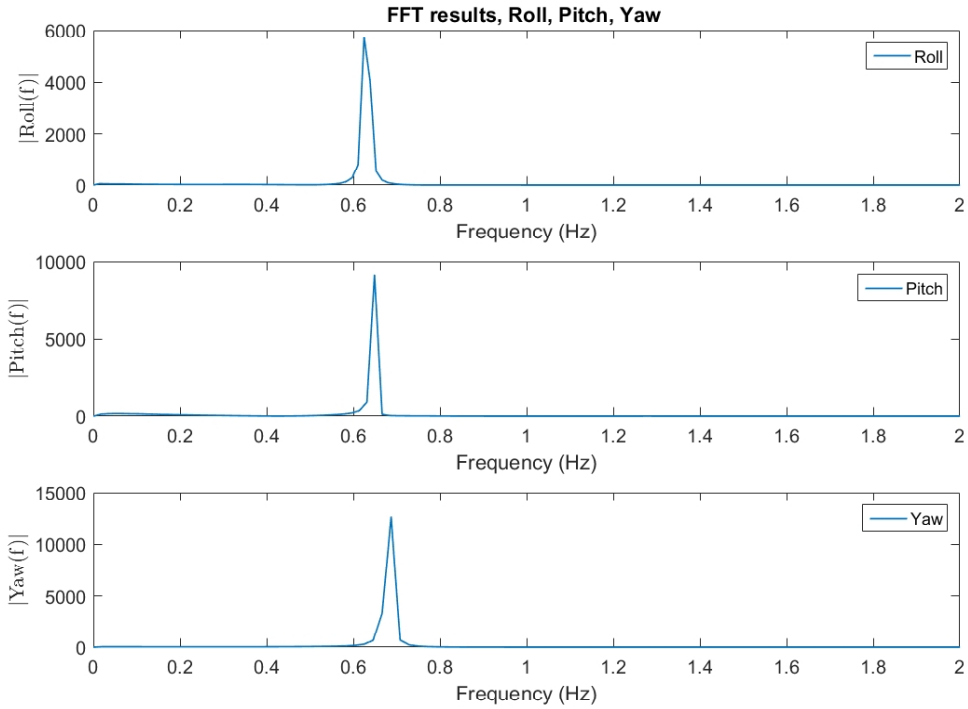

FIGURE 4.3: Results from roll, pitch and yaw experiments

Chapter 5

Attitude Estimation using IMU measurements

As the attitude of a rigid body is not a directly measurable value, it must be estimated through some form of observer. Popular methods for this reconstruction include static estimation[12], kalman filtering[56], and complementary filtering [18], [57]. All methods herein rely on the assumptions:

1. The quadrotor is near hover *i.e.* $\mathbf{a}_{\mathcal{B}} \approx -g\mathbf{R}^T\hat{\mathbf{e}}_3$
2. Two non-colinear vectors can be measured with their inertial counterparts known

5.1 Static Estimation

Utilizing a widely available Inertial Measurement Unit (IMU), it is possible to measure, the acceleration in the body frame $\mathbf{a}_{\mathcal{B}}$ and the magnetic field in the body frame $\mathbf{m}_{\mathcal{B}}$.

These vectors are utilized as their inertial counterparts are readily available as $\mathbf{a}_{\mathcal{I}} = [0\ 0\ g]^T$ and $\mathbf{m}_{\mathcal{I}}$ to be found from available resources such as [58]. As the vectors $\mathbf{a}_{\mathcal{B}}$ and $\mathbf{m}_{\mathcal{B}}$ are non-colinear ($S(\mathbf{a}_{\mathcal{B}})\mathbf{m}_{\mathcal{B}} \neq 0$) it is then possible to define a third vector

$$\mathbf{w}_{\mathcal{B}} = S(\mathbf{a}_{\mathcal{B}})\mathbf{m}_{\mathcal{B}},$$

likewise

$$\mathbf{w}_{\mathcal{I}} = S(\mathbf{a}_{\mathcal{I}})\mathbf{m}_{\mathcal{I}},$$

where for all three of these vectors the relationship $\mathbf{u}_{\mathcal{B}} = \mathbf{R}^T\mathbf{u}_{\mathcal{I}}$ holds. Arranging these vectors side by side results in

$$\left[\ \mathbf{a}_{\mathcal{B}}\ \vdots\ \mathbf{m}_{\mathcal{B}}\ \vdots\ \mathbf{w}_{\mathcal{B}}\ \right] = \mathbf{R}^T\left[\ \mathbf{a}_{\mathcal{I}}\ \vdots\ \mathbf{m}_{\mathcal{I}}\ \vdots\ \mathbf{w}_{\mathcal{I}}\ \right], \tag{5.1}$$

which can be solved for $\mathbf{R}^T$

$$\mathbf{R}^T = \left[\ \mathbf{a}_{\mathcal{B}}\ \vdots\ \mathbf{m}_{\mathcal{B}}\ \vdots\ \mathbf{w}_{\mathcal{B}}\ \right] \cdot \left[\ \mathbf{a}_{\mathcal{I}}\ \vdots\ \mathbf{m}_{\mathcal{I}}\ \vdots\ \mathbf{w}_{\mathcal{I}}\ \right]^{-1}.$$

Although this method is analytically simplistic, in real time implementations calculating the inverse or a matrix is a computationally heavy task, and should be avoided if at all possible. Further this method offers no form of filtering for the noisy measurements and as such will not produce a reliable result. Due to these pitfalls, methods that instead rely on the rotational dynamics of the quadrotor, as well as IMU measurements implemented to produce much more reliable results.

5.2 Complemetary Filtering

A more reliable method relying on the quadrotor attitude dynamics eq. 4.2 is that of the complementary filter [57]. This type of filtering is more reliable than that of Kalman filtering as it does not rely on a linearization of the system around some operating condition, and instead uses the complete non-linear dynamics of the system. This form of estimator includes measurements from a gyroscope readily available in IMUs. This estimator will also account for a slow varying bias that most gyroscope are inherently susceptible to. Let us define the measured angular velocity as:

$$\Omega_{meas} := \Omega + \mathbf{b}, \tag{5.2}$$

where Ω is the true angular velocity and $\mathbf{b}$ is a slow time varying offset bias. Let us define the following unit vectors:

$$\begin{array}{cc} \mathbf{u}_{\mathcal{B}} := \mathbf{a}_{\mathcal{B}}/g & \mathbf{v}_{\mathcal{B}} := \mathbf{m}_{\mathcal{B}}/\|\mathbf{m}_{\mathcal{I}}\| \\ \mathbf{u}_{\mathcal{I}} := \hat{\mathbf{e}}_3 & \mathbf{v}_{\mathcal{I}} := \mathbf{m}_{\mathcal{I}}/\|\mathbf{m}_{\mathcal{I}}\| \end{array}. \tag{5.3}$$

The observer is then given by

$$\begin{cases} \dot{\hat{\mathbf{R}}} = \hat{\mathbf{R}} S\left(\Omega_{meas} - \hat{\mathbf{b}} + \sigma_{\mathbf{R}}\right) \\ \dot{\hat{\mathbf{b}}} = -k_I \sigma_{\mathbf{R}} \\ \sigma_{\mathbf{R}} = k_1 S(\mathbf{u}_{\mathcal{B}})\hat{\mathbf{u}}_{\mathcal{B}} + k_2 S(\mathbf{v}_{\mathcal{B}})\hat{\mathbf{v}}_{\mathcal{B}}, \end{cases} \tag{5.4}$$

where $\hat{\mathbf{u}}_{\mathcal{B}}$ and $\hat{\mathbf{v}}_{\mathcal{B}}$ are given by

$$\hat{\mathbf{u}}_{\mathcal{B}} = \hat{\mathbf{R}}^T \mathbf{u}_{\mathcal{I}} \quad \hat{\mathbf{v}}_{\mathcal{B}} = \hat{\mathbf{R}}^T \mathbf{v}_{\mathcal{I}}. \tag{5.5}$$

It is easily seen that the innovation term $\sigma_{\mathbf{R}}$ will vanish when the estimated attitude matches the true attitude of the VTOL UAV. It can also be seen that the term $\hat{\mathbf{b}}$ is the integral of this innovation term, which may lead to a drift over time due to the presence of measurement noise and constant biases in the innovation term. Moreover, the magnetometer measurements are often non-reliable and may deteriorate the performance of the aforementioned attitude observer. These problems are mitigated in the following conditioned observer.

5.3 Conditioned Attitude Observer

In a similar fashion to the prior observer we define the following vectors:

$$\begin{array}{cc} \mathbf{u}_{\mathcal{B}} := -\frac{\mathbf{a}_{\mathcal{B}}}{g}, & \mathbf{v}_{\mathcal{B}} := \frac{\boldsymbol{\pi}_{\mathbf{u}_{\mathcal{B}}} \mathbf{m}_{\mathcal{B}}}{\|\boldsymbol{\pi}_{\mathbf{u}_{\mathcal{I}}} \mathbf{m}_{\mathcal{I}}\|} \\ \mathbf{u}_{\mathcal{I}} := \hat{\mathbf{e}}_3, & \mathbf{v}_{\mathcal{I}} := \frac{\boldsymbol{\pi}_{\mathbf{u}_{\mathcal{I}}} \mathbf{m}_{\mathcal{I}}}{\|\boldsymbol{\pi}_{\mathbf{u}_{\mathcal{I}}} \mathbf{m}_{\mathcal{I}}\|} \end{array}, \tag{5.6}$$

where $\boldsymbol{\pi}_x$ is the orthogonal projection of a vector v onto the plane orthogonal to x, defined as $\boldsymbol{\pi}_x := \|x\|^2 \mathbb{I}_{3\times 3} - xx^T, \forall x \in \mathbb{R}^3$. Letting $x = \hat{\mathbf{e}}_3$ results in the matrix

$$\boldsymbol{\pi}_x = \begin{bmatrix} 1 & 0 & 0 \\ 0 & 1 & 0 \\ 0 & 0 & 0 \end{bmatrix},$$

which ensures that only the x and y components of $\mathbf{m}_{\mathcal{I}}$ remain. Further using this projection with the vector $x = a_{\mathcal{B}}/g$, ensures that only the projections of $\mathbf{m}_{\mathcal{B}}$ onto the plane orthogonal to $\mathbf{R}^T\hat{\mathbf{e}}_3$ remain. These new vectors can then be compared to help determine the yaw angle of the rigid body. Through these projections, coupling of the yaw and pitch angles can be mitigated. Pitch and roll estimates are now more heavily influenced by the accelerometer data, which can provide a good direct estimate. The conditioned observer is given by [18]

$$\begin{cases} \dot{\hat{\mathbf{R}}} = \hat{\mathbf{R}}S(\Omega_{meas} - \hat{\mathbf{b}} + \boldsymbol{\sigma}_{\mathbf{R}}),\ \mathbf{R}(0) \in SO(3) \\ \dot{\hat{\mathbf{b}}} = -k_b\left(\hat{\mathbf{b}} - \text{sat}_{\Delta}(\hat{\mathbf{b}})\right) + \boldsymbol{\sigma}_{\mathbf{b}},\ \|\hat{\mathbf{b}}(0)\| < \Delta \\ \boldsymbol{\sigma}_R := k_1 S(\mathbf{u}_{\mathcal{B}})\hat{\mathbf{u}}_{\mathcal{B}} + k_2\mathbf{u}_{\mathcal{B}}\hat{\mathbf{u}}_{\mathcal{B}}^T S(\mathbf{v}_{\mathcal{B}})\hat{\mathbf{v}}_{\mathcal{B}} \\ \boldsymbol{\sigma}_b := -k_3 S(\mathbf{v}_{\mathcal{B}})\hat{\mathbf{v}}_{\mathcal{B}} - k_4 S(\mathbf{u}_{\mathcal{B}})\hat{\mathbf{u}}_{\mathcal{B}}, \end{cases} \tag{5.7}$$

with $\text{sat}_{\Delta}(\cdot)$ being the classical saturation function defined as $\text{sat}_{\Delta}(x) := x\min\left(\frac{\Delta}{\text{abs}(x)}, 1\right)$. This version of the observer alters the proportional innovation term $\sigma_{\mathbf{R}}$ in a way that further helps to decouple roll and yaw angles by multiplying the term influenced by the magnetic field by the accelerometer measurement vector. The $\dot{\hat{\mathbf{b}}}$ term remains the same as the complementary filter when $\|\hat{\mathbf{b}}\| < \Delta$, if this estimation grows too large the dynamics of $\hat{\mathbf{b}}$ now include a $-\hat{\mathbf{b}}$ term which is used to minimize the effects of integral windup. The term Δ must be chosen based upon real life measurements otherwise the observer will not track the true attitude (Δ too small) or the effects of the integral windup of the previous observer will not be mitigated (Δ too large). For more details on the effects and minimization of integral windup the reader is refered to [59]. The rate at which the desaturation of $\hat{\mathbf{b}}$ is determined by the gain k_b, the proportional innovation term gains are k_1 and k_2, and the integral innovation gains are k_3 and k_4. As long as the gain k_3 is greater than k_4 this observer shows asymptotic convergence of $(\hat{\mathbf{R}}(t), \hat{\mathbf{b}}(t))$ to $(\mathbf{R}(t), \mathbf{b}(t))$ for almost all initial conditions (see Theorem 1 [18]).

5.4 Quaternion Version and Discretization

As working with the full rotation matrix is often inefficient and computationally expensive, the observer described in eq. 5.7 may be rewritten as:

$$\begin{cases} \dot{\hat{Q}} = \frac{1}{2}A(\hat{\Omega})\hat{Q},\ \hat{Q}(0) \in \mathcal{Q} \\ \dot{\hat{\mathbf{b}}} = -k_b\left(\hat{\mathbf{b}} - sat_{\Delta}(\hat{\mathbf{b}})\right) + \boldsymbol{\sigma}_{\mathbf{b}},\ \|\hat{\mathbf{b}}(0)\| < \Delta \\ \boldsymbol{\sigma}_R := k_1 S(\mathbf{u}_{\mathcal{B}})\hat{\mathbf{u}}_{\mathcal{B}} + k_2\mathbf{u}_{\mathcal{B}}\hat{\mathbf{u}}_{\mathcal{B}}^T S(\mathbf{v}_{\mathcal{B}})\hat{\mathbf{v}}_{\mathcal{B}} \\ \boldsymbol{\sigma}_b := -k_3 S(\mathbf{v}_{\mathcal{B}})\hat{\mathbf{v}}_{\mathcal{B}} - k_4 S(\mathbf{u}_{\mathcal{B}})\hat{\mathbf{u}}_{\mathcal{B}} \\ \hat{\Omega} := \Omega_{meas} - \hat{\mathbf{b}} + \boldsymbol{\sigma}_{\mathbf{R}} \\ A(\hat{\Omega}) := \begin{bmatrix} 0 & -\hat{\Omega}^T \\ \hat{\Omega} & -S(\hat{\Omega}) \end{bmatrix}, \end{cases} \tag{5.8}$$

where the Rodrigues formula is used to determine the dynamics of $\hat{Q}$. Utilizing the Euler discretization method, one obtains

$$\hat{Q}_{k+1} = \exp\left(\frac{T}{2}A(\hat{\Omega}_k)\right)\hat{Q}_k,$$

where, when noting that $e^{\mathbf{X}} = \sum_{i=0}^{\infty} \frac{1}{i!}\mathbf{X}^i$ and $A(\Omega_k)^2 = -\|\Omega_k\|^2\mathbb{I}_{4\times4}$ it is seen that the final discretized system is given by:

$$\begin{cases} \hat{Q}_{k+1} = \left(\cos\left(\frac{T\|\Omega_k\|}{2}\right)\mathbf{I}_{4\times4} + \frac{T}{2}\text{sinc}\left(\frac{T\|\Omega_k\|}{2}\right)A(\hat{\Omega}_k)\right)\hat{Q}_k \\ \hat{\mathbf{b}}_{k+1} = -T\left(k_b\left(\hat{\mathbf{b}}_k - sat_\Delta(\hat{\mathbf{b}}_k)\right) + \boldsymbol{\sigma}_{\mathbf{b},k}\right) + \hat{\mathbf{b}}_k, \end{cases} \tag{5.9}$$

which can then be easily implemented on a standard 8-bit microcontroller.

5.5 Simulations and Implementation Results

The gains and parameters chosen for the simulation of the observer (5.8) are chosen as

$$k_1 = 2.0,\ k_2 = k_1/6,\ k_3 = k1/32,\ k_4 = k2/32,\ k_b = 20,\ \Delta = 0.05. \tag{5.10}$$

The gain k_1 is chosen larger than the gain k_2, as the measurement of the gravity vector is assumed to be better conditioned than the measurement of the magnetic field, both gains k_1 and k_2 are chosen quite large to ensure fast convergence of the estimated attitude to the true attitude. The integral gains k_3 and k_4 are chosen to be very small relative to the gains k_1 and k_2 to reduce the integral windup effects. A large value for k_b is chosen so that any integral windup effects are eliminated as quickly as possible without affecting the observer negatively. Finally, the upper bound on the $\hat{\mathbf{b}}$ estimate (Δ) is chosen based on experimental values, wherein the quadrotor was placed stationary and the gyroscope values measured and averaged. Two simulations are shown; in the first the initial attitude estimation is taken as $\hat{Q}(0) = [0\ 1\ 0\ 0]^T$ corresponding to a completely inverted attitude, *i.e.* the worst possible scenario, in the second the initial condition is set as $\hat{Q}(0) = [0.707\ 0.707\ 0\ 0]^T$ corresponding to a roll angle of $\sim 90^\circ$. For both simulations the true attitude is fixed as $Q = [1\ 0\ 0\ 0]^T$, and the initial condition of $\hat{\mathbf{b}}$ is given as $\hat{\mathbf{b}}(0) = [0\ 0\ 0]^T$. Noise values for both simulations are as follows: $\sigma^2_{mag} = 0.125\text{G}^2$, $\sigma^2_{gyro} = 0.023\text{rad}^2/\text{s}^2$, $\sigma^2_{accel} = 0.012\text{m}^2/\text{s}^4$ with a constant gyro bias of $\mathbf{b} = [0.004\ -0.02\ 0.01]^T$. The gains for the real time implementation of the quaternion estimator are chosen to be the same as those chosen for the simulations, as these choices provided excellent results.

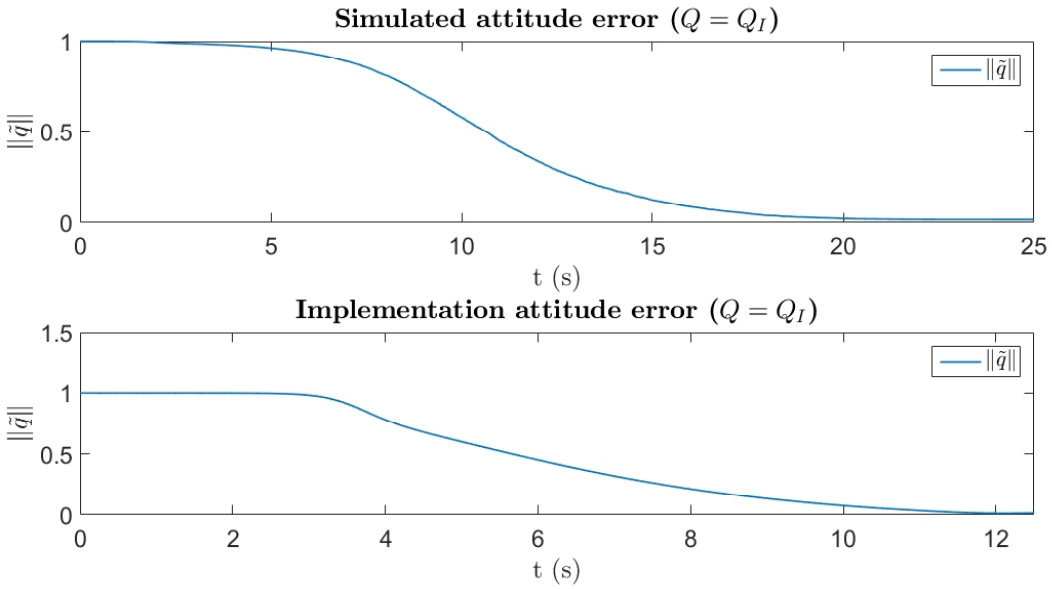

FIGURE 5.1: $\hat{Q}$ simulation and implementation results for $\hat{Q}_0 = [0\ 1\ 0\ 0]$

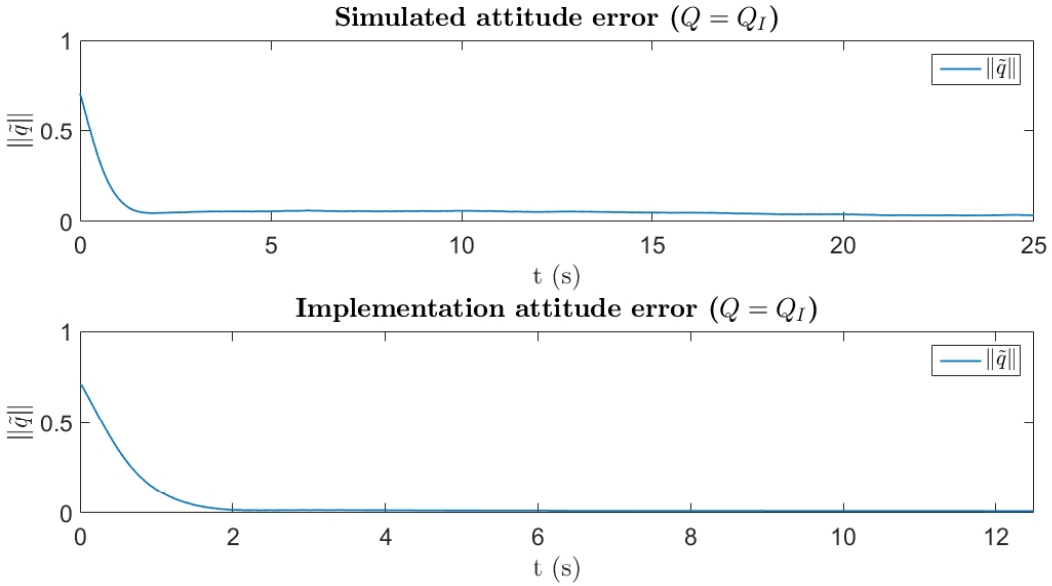

FIGURE 5.2: $\hat{Q}$ simulation and implementation results for $\hat{Q}_0 = [0.707\ 0.707\ 0\ 0]$

From both simulation and implementation results it is evident that, even from large initial conditions and considerable sensor noise, the observer will converge quickly to the true attitude. Small errors are present in both simulation and implementation results, these errors are primarily present in the yaw angle estimation, and are due to the unknown Electromagnetic Interference (EMI) present in both simulations and implementation. Over a longer time period, these errors vanish and the observer produces a more accurate estimation of the true attitude.

Chapter 6

Position and Linear Velocity Estimation using UWB Measurements and Kalman Filtering

Many methods for determining the position of a target node in a wireless network exist [60], each of which will carry its own advantages and disadvantages. For the purposes of indoor positioning one wishes to obtain the highest possible accuracy as there are many obstacles in the area that must be avoided. For this reason, a time based raging process is often chosen as it offers much greater accuracy over Received Signal Strength (RSS) methods in indoor environments [61]. The inaccuracy in RSS methods is largely due to the presence of multi-path propagation as well as unknown sources of interference in the environment. These unknown parameters in the environment cause the normal propagation model [61] to be heavily altered and therefore no longer reliable (see [62] for WLAN reference). Further improvements to the accuracy of the system can be made if the time based ranging method chosen has a very large bandwidth, as the Cramer-Rao lower bound on the variance of the distance measurement (lowest measurement variance possible) is inversely proportional to the bandwidth of the selected method [63]. Considering these factors, a system implemented with UWB sensors will provide good results, often with precisions in the sub $10cm$ range.

6.1 Time of Flight Ranging method

The ranging method chosen is a Time of Flight (ToF) method. With this type of ranging method, measurements of distance occur directly between the target node and an individual anchor node. By performing measurements in this manner the clock synchronization required by Time Difference of Arrival (TDoA) methods can be eliminated through a double-sided two way messaging scheme such as the one described in [64]. In this type of ranging method information about the target and anchors clock are shared in the payload of the transmitted messages. With this information it is then possible to accurately account for the clock offset between the two nodes. This method can be accomplished with either 3 or 4 messages between the nodes, as the 4 message method requires simpler calculations better suited for low power microcontrollers [65] and offers more precise results. This method results in a ToF measurement defined as:

$$\hat{T}_{prop} = \frac{2(t^T_{Rx2} - t^A_{Tx2}) + (t^A_{Rx1} - t^T_{Tx1}) + (t^A_{Rx3} - t^T_{Tx3})}{4} + \eta, \tag{6.1}$$

with subscripts Rx and Tx denoting sequential receive and transmit times respectively, superscripts A and T denoting anchor and tag measurements, and η being an additive Gaussian noise. Assuming the clock drift is constant throughout the complete measurement time and appears as $t^T_{Rxi} := t^T_{Rxi} + \delta^T$ at the tag node and $t^A_{Rxi} := t^A_{Rxi} + \delta^A$, this will also be accounted for in this method as in the numerator it will appear as

$$2(\delta^T - \delta^A) + (\delta^A - \delta^T) + (\delta^A - \delta^T),$$

which is clearly equal to zero. This ToF estimation can then easily be converted to a distance

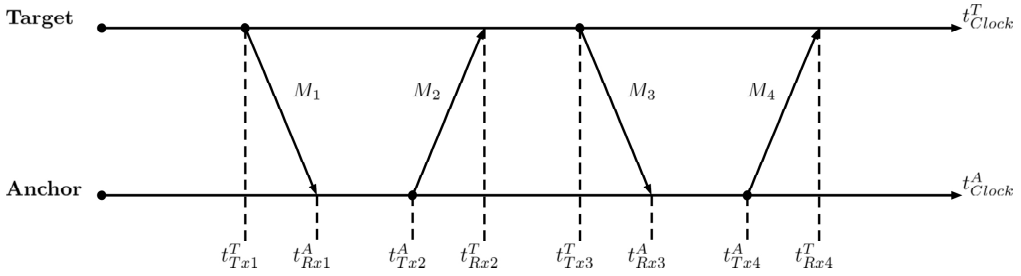

FIGURE 6.1: Four message two way ranging scheme

through

$$\hat{d} = c\hat{T}_{prop} = d + \eta_d, \tag{6.2}$$

with $c = 3 \times 10^8 m/s$ being the speed of light.

6.2 Static Positioning Algorithm

Due to the minimal computational power available on the micro-controllers utilized, a simple method of static position estimation is implemented. The distance equation given in 6.1 can be rewritten into the classical form of a sphere as

$$\hat{d}_i = \sqrt{(x_i - x)^2 + (y_i - y)^2 + (z_i - z)^2} + \eta_i = |\mathbf{z}_i - \mathbf{p}| + \eta_i, \tag{6.3}$$

with $\mathbf{z}_i = [x_i\ y_i\ z_i]^T$ being the position of the i^{th} anchor and $\mathbf{p} = [x\ y\ z]^T$ being the position of the target node (Drone). Using four anchors one has [39]

$$\begin{aligned}
\hat{d}_1^2 &= (x_1 - x)^2 + (y_1 - y)^2 + (z_1 - z)^2 + \eta_1 \\
\hat{d}_2^2 &= (x_2 - x)^2 + (y_2 - y)^2 + (z_2 - z)^2 + \eta_2 \\
\hat{d}_3^2 &= (x_3 - x)^2 + (y_3 - y)^2 + (z_3 - z)^2 + \eta_3 \\
\hat{d}_4^2 &= (x_4 - x)^2 + (y_4 - y)^2 + (z_4 - z)^2 + \eta_4,
\end{aligned} \tag{6.4}$$

after subtracting one of the 4 equations from the others, *e.g.* $\{\hat{d}_2^2, \hat{d}_3^2, \hat{d}_4^2\} - \hat{d}_1^2$, one gets

$$2 \begin{bmatrix} \mathbf{z}_2 - \mathbf{z}_1 \\ \mathbf{z}_3 - \mathbf{z}_1 \\ \mathbf{z}_4 - \mathbf{z}_1 \end{bmatrix} \mathbf{p} = \begin{bmatrix} \hat{d}_1^2 - \hat{d}_2^2 \\ \hat{d}_1^2 - \hat{d}_3^2 \\ \hat{d}_1^2 - \hat{d}_4^2 \end{bmatrix} + \begin{bmatrix} \mathbf{z}_2^T\mathbf{z}_2 - \mathbf{z}_1^T\mathbf{z}_1 \\ \mathbf{z}_3^T\mathbf{z}_3 - \mathbf{z}_1^T\mathbf{z}_1 \\ \mathbf{z}_4^T\mathbf{z}_4 - \mathbf{z}_1^T\mathbf{z}_1 \end{bmatrix} + \begin{bmatrix} \eta_{12} \\ \eta_{13} \\ \eta_{14} \end{bmatrix}, \tag{6.5}$$

or similarly in matrix form as

$$\mathbf{Ap} = \mathbf{b}_{meas} + \mathbf{b}_{const} + \boldsymbol{\eta}, \tag{6.6}$$

which is then solved using the LS approach

$$\mathbf{p} = \left(\mathbf{A}^T\mathbf{A}\right)^{-1}\mathbf{A}^T\left(\mathbf{b}_{meas} + \mathbf{b}_{const}\right). \tag{6.7}$$

Taking notice of the noise term in eq. 6.6, as this term is a combination of 2 measurement variances some assumptions are made:

1. ToA measurement variances are independant of one another [39]
2. Line of sight environment ensures $\sigma_x = \sigma_y = \sigma_z = \sigma$, as shown in [66]
3. Clock offsets are accounted for through 2 way ranging method (above and [64])

from item 1 above it is clear that the addition of these variances is possible. As the position estimation is corrupted by the noise term given, the goal now is to minimize the effect of this on the position estimate. This minimization is handled twofold through: optimal positioning of anchor nodes, and the introduction of a Kalman Filter utilizing system dynamics and available measurements.

6.2.1 Optimal Anchor Positioning

From the distance equations given in eq. 6.1 and 6.3, the function f_i can be defined as:

$$f_i(\mathbf{z}_i, \mathbf{p}, \hat{T}_{prop}) := \sqrt{(x_i - x)^2 + (y_i - y)^2 + (z_i - z)^2} - c \cdot \hat{T}_{prop}, \tag{6.8}$$

With the addition of more anchor nodes the vector form of this is

$$\begin{bmatrix} f_1 \\ f_2 \\ \vdots \end{bmatrix} = \begin{bmatrix} \sqrt{(x_1 - x)^2 + (y_1 - y)^2 + (z_1 - z)^2} - c \cdot \hat{T}_{prop_1} \\ \sqrt{(x_2 - x)^2 + (y_2 - y)^2 + (z_2 - z)^2} - c \cdot \hat{T}_{prop_2} \\ \vdots \end{bmatrix}, \tag{6.9}$$

then taking the derivative of this vector with respect to each of the variables $\{\mathbf{p}, \hat{T}_{prop}\}$, results in a $N \times 4$ matrix defined as A

$$A := \begin{bmatrix} \frac{x_1 - x}{\|\mathbf{z_A} - \mathbf{p}\|} & \frac{y_1 - y}{\|\mathbf{z_1} - \mathbf{p}\|} & \frac{z_1 - z}{\|\mathbf{z_1} - \mathbf{p}\|} & -1 \\ \frac{x_2 - x}{\|\mathbf{z_2} - \mathbf{p}\|} & \frac{y_2 - y}{\|\mathbf{z_2} - \mathbf{p}\|} & \frac{z_2 - z}{\|\mathbf{z_2} - \mathbf{p}\|} & -1 \\ \vdots & \vdots & \vdots & \vdots \end{bmatrix}, \tag{6.10}$$

utilizing the method described in [66], the covariance matrix of the measurements is extracted

$$C_{\mathbf{p}} = \sigma^2\left(A^T A\right)^{-1}. \tag{6.11}$$

This covariance matrix has a direct relationship to a metric known as dilution of precision [66](depicted in Fig.6.2.1), which will be large with poor anchor placement and much smaller with improved anchor placement. By minimizing the covariance matrix, the dilution of precision will be minimized, and the optimal anchor positions determined. This minimization must be

accomplished over the entire space where the target will be located and as such leads to the cost function

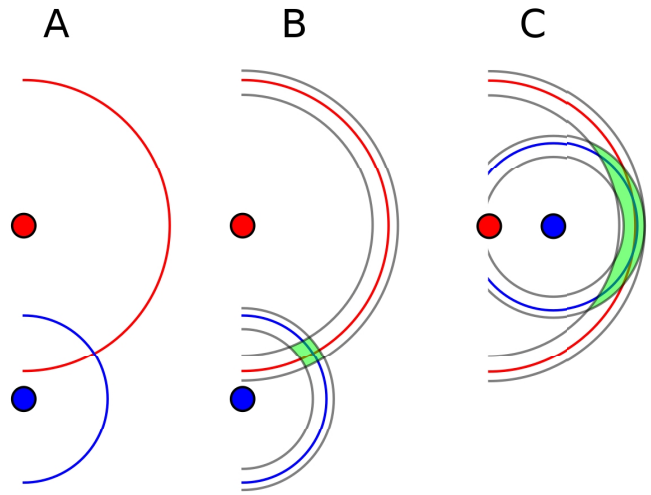

FIGURE 6.2: 2 Dimensional DOP, with respect to anchor node placement [67]

$$F(\mathbf{p}, \mathbf{z}_i) := \frac{1}{D} \iiint_D \|C_\mathbf{p}\|_F \quad \forall i \in \{1, \ldots, N\}, \tag{6.12}$$

for 3-Dimensions, where D is defined as the space wherein the target will lie, similarly for 2-Dimensions this cost function is

$$F(\mathbf{p}, \mathbf{z}_i) := \frac{1}{D} \iint_D \|C_\mathbf{p}\|_F \quad \forall i \in \{1, \ldots, N\}. \tag{6.13}$$

For both scenarios 'N' is the number of base stations utilized.
In either scenario, the cost function is a nonlinear combination of a large number of variables. As it is not possible to find an analytic solution numerical methods must be employed. Many methods to achieve this minimization exist [68]. For this experiment, the Matlab "fmincon" function which relies on a interior point method such as those described in [69], and provides a local minimum solution is used. As the solution given by this is only a local, multiple initial conditions must be tried to ensure that the solution is the smallest local minimum. These minimizations are carried out for both the 2-Dimensional and 3-Dimensional cases, with practical results compared to theoretical results for the 2-dimensional case. It is evident for the case where the base stations are placed in a diamond shape that the magnitude of the covariance matrix grows quite large in the corners showing the sub-optimal placement of the anchor nodes. In the areas where the covariance matrix grows large, the measurements become quite unreliable, and as such this set of anchor placements should not be utilized. As well, the cost function results for the two placements were measured by placing the target node in multiple positions around the predefined area an taking a number of measurements at each position, these results are shown in Table. 6.1.

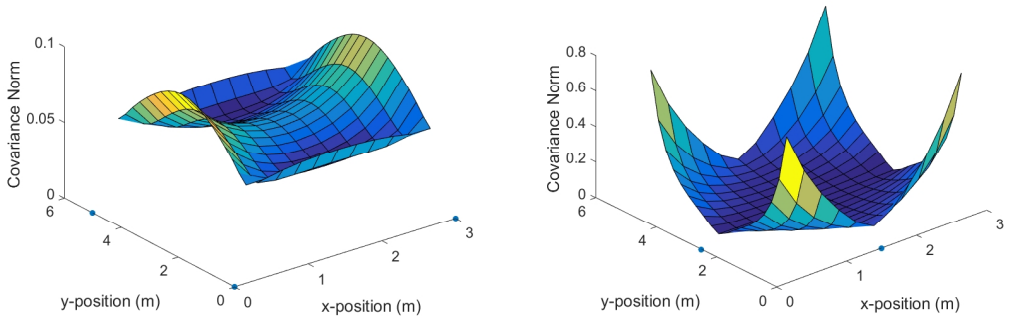

(A) 2-D covariance matrix magnitude 4 anchors, placed in 4 corners

(B) 2-D covariance matrix magnitude 4 anchors, placed in a diamond shape

FIGURE 6.3: Comparison of optimal and sub-optimal anchor placements

Anchor Config	Cost Function Value m^{-2}		Percent Error
	Calculated	measured	
diamond	2.81	2.78	1.1%
square	1.21	1.39	14.8%

TABLE 6.1: Cost function results, real vs estimated ($3m \times 5m$ $area, \sigma = 0.06m$)

It can be seen that the value of the measured cost functions match closely the calculated values with a discrepancy due mainly due to inaccurate values of σ used in simulations. As well, any number 'N' of anchors may be used, and the goal is to find a reasonable solution for the number of anchors. As such, another optimization problem is defined through the new cost function

$$\begin{aligned} F(\mathbf{p}, \mathbf{z}_i, N) := & \left\{ \frac{1}{D} \iiint_D \|C_{\mathbf{p}}\|_F \right\} N \\ & \forall i \in \{1, \ldots, N\} \\ & N \in \mathbb{Z}_+, \end{aligned} \tag{6.14}$$

which results in the dual minimization where $N \in \mathbb{Z}_+$ minimizes

$$N = \arg\min_{N \in \mathbb{Z}_+} \left\{ \min_{\forall i \in [1,N]} \left(\frac{1}{D} \iiint_D \|C_{\mathbf{p}}\|_F \right) N \right\}. \tag{6.15}$$

This computation is again done numerically and results in a local optimum number of $N = 8$ for a $10 \times 10 \times 10m$ cube

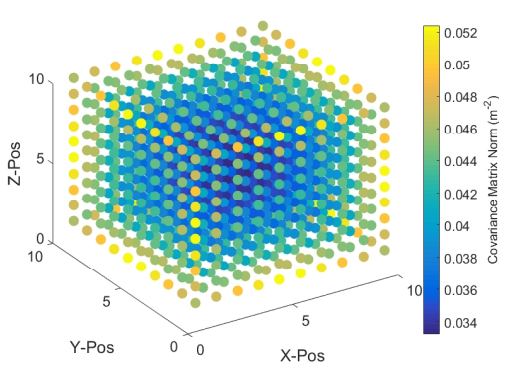

(A) 3-D covariance matrix magnitude 8 anchors placed on each corner

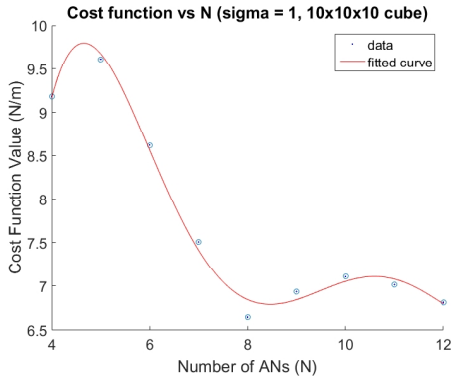

(B) Cost function (eq. 6.14) vs N, showing local minima at N = 8 ($\sigma = 1$)

6.3 Kalman Filtering For Position and Velocity Estimates

To further reduce the effects of the measurement noise a Kalman filter utilizing the translational dynamics of the quadrotor is implemented

$$\begin{aligned} \dot{\mathbf{p}} &= \mathbf{v} \\ \dot{\mathbf{v}} &= \mathbf{u}, \end{aligned} \tag{6.16}$$

where

$$\mathbf{u} := g\hat{\mathbf{e}}_3 + \mathbf{R}\mathbf{a}_{\mathcal{B}}, \tag{6.17}$$

with $\mathbf{a}_{\mathcal{B}}$ being the accelerometer measurement provided by the IMU. Discretizing the model in 6.16 gives:

$$\mathbf{x_{k+1}} = \begin{bmatrix} 1 & T & 0 & 0 & 0 & 0 \\ 0 & 1 & T & 0 & 0 & 0 \\ 0 & 0 & 1 & T & 0 & 0 \\ 0 & 0 & 0 & 1 & 0 & 0 \\ 0 & 0 & 0 & 0 & 1 & 0 \\ 0 & 0 & 0 & 0 & 0 & 1 \end{bmatrix} \mathbf{x_k} + \begin{bmatrix} T^2/2 & 0 & 0 \\ 0 & T^2/2 & 0 \\ 0 & 0 & T^2/2 \\ T & 0 & 0 \\ 0 & T & 0 \\ 0 & 0 & T \end{bmatrix} \mathbf{u} \tag{6.18}$$

$$\mathbf{y}_k = \begin{bmatrix} 1 & 0 & 0 & 0 & 0 & 0 \\ 0 & 1 & 0 & 0 & 0 & 0 \\ 0 & 0 & 1 & 0 & 0 & 0 \end{bmatrix} \mathbf{x_k}, \tag{6.19}$$

or like-wise

$$\mathbf{x_{k+1}} = \mathbf{\Phi x_k} + \mathbf{B}\mathbf{u}_k \tag{6.20}$$

$$\mathbf{y_k} = \mathbf{C x_k}, \tag{6.21}$$

with $\mathbf{x}_k := \left[\mathbf{p}_k^T \ \mathbf{v}_k^T\right]^T$ and $\mathbf{y}_k = \mathbf{p}_k$. The Kalman Filter update equations are given by [15]

$$\begin{aligned}
\hat{\mathbf{x}}_\mathbf{k}^- &= \mathbf{\Phi x_{k-1}} + \mathbf{Bu_k} \\
\mathbf{P_k}^- &= \mathbf{\Phi P_{k-1} \Phi^T} + \mathbf{Q} \\
\mathbf{K_k} &= \mathbf{P_k^- C^T}(\mathbf{C P_k^- C^T} + \mathbf{R})^{-1} \\
\hat{\mathbf{x}}_\mathbf{k} &= \hat{\mathbf{x}}_\mathbf{k}^- + \mathbf{K_k}(\mathbf{y}_k - \mathbf{C}\hat{\mathbf{x}}_\mathbf{k}^-) \\
\mathbf{P_k} &= \mathbf{P_k^-} - \mathbf{K_k C P_k^-},
\end{aligned} \tag{6.22}$$

with process and measurement covariance matrices (Q ad R) defined from measurements preformed in the lab, taking the positive definite form of

$$\mathbf{Q} = \begin{bmatrix}
\sigma_{wx}^2 T^3/3 & \sigma_{wx}^2 T^2/2 & 0 & 0 & 0 & 0 \\
\sigma_{wx}^2 T^2/2 & \sigma_{wx}^2 T & 0 & 0 & 0 & 0 \\
0 & 0 & \sigma_{wy}^2 T^3/3 & \sigma_{wy}^2 T^2/2 & 0 & 0 \\
0 & 0 & \sigma_{wy}^2 T^2/2 & \sigma_{wy}^2 T & 0 & 0 \\
0 & 0 & 0 & 0 & \sigma_{wz}^2 T^3/3 & \sigma_{wz}^2 T^2/2 \\
0 & 0 & 0 & 0 & \sigma_{wz}^2 T^2/2 & \sigma_{wz}^2 T
\end{bmatrix} \tag{6.23}$$

$$\mathbf{R} = \begin{bmatrix}
\sigma_{vx}^2/T & 0 & 0 \\
0 & \sigma_{vy}^2/T & 0 \\
0 & 0 & \sigma_{vz}^2/T
\end{bmatrix}. \tag{6.24}$$

6.3.1 Simulation Results

From experiments performed it was found that $\sigma_{v_x} = \sigma_{v_y} = \sigma_{v_z} = \sigma_v = 10cm$, so this value is chosen for simulations as well as real-time applications. Further, as the drone with all intents will be a "slowly-moving" target, a value of $\sigma_{w_x} = \sigma_{w_y} = \sigma_{w_z} = \sigma_v = 1.5m$ is chosen to help prevent overshoot and divergence of the Kalman filter. Simulations are performed for a target moving along the path

$$\begin{aligned}
x_{true} &= 1.5 + 1.5\sin(\tfrac{2\pi t}{100}) \\
y_{true} &= 2.5 + 1.5\cos(\tfrac{2\pi t}{100}) \\
z_{true} &= 1.25 + 1.5/2\cos(\tfrac{\pi t}{100}).
\end{aligned}$$

Noise on the accelerometer is modelled as $\eta_{accel} \sim N(0, 0.25m^2/s^4)$. Two simulations are performed, in the first the distance measurement is corrupted by a noise modeled as $\eta_{di} \sim N(0, 0.1m^2)$ (similar to real life values), and in the second the the distance measurement is affected by the same type of noise but instead $\sigma_{d_i}^2 = 1m$. In both simulations,four anchor nodes were placed in the optimal positions determined from simulations performed in the last section.

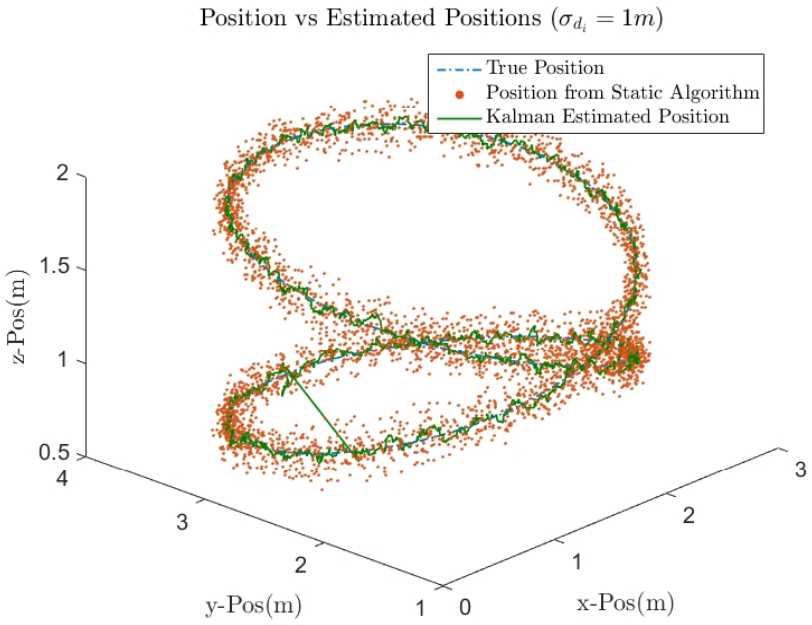

FIGURE 6.5: Kalman filtering flight path simulation results, $\sigma_d = 1m$

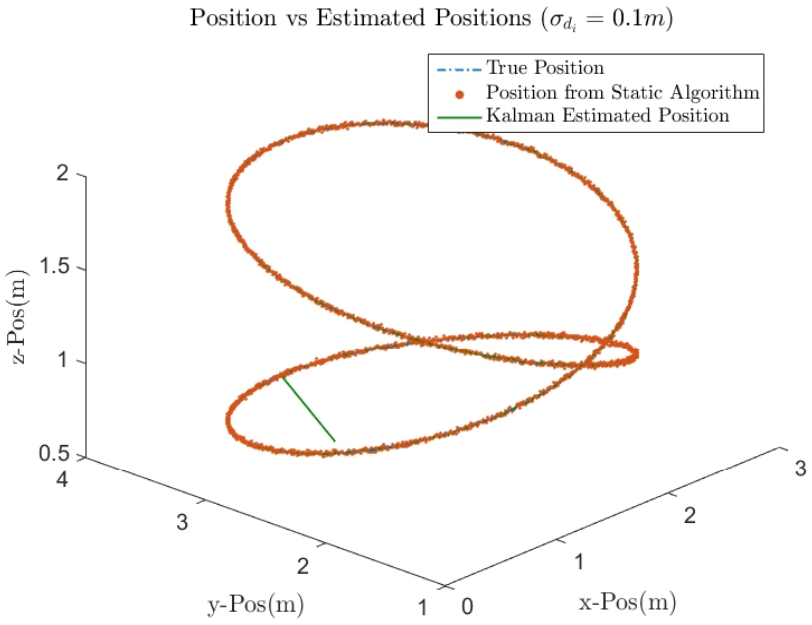

FIGURE 6.6: Kalman filtering flight simulation results, $\sigma_d = 0.1m$

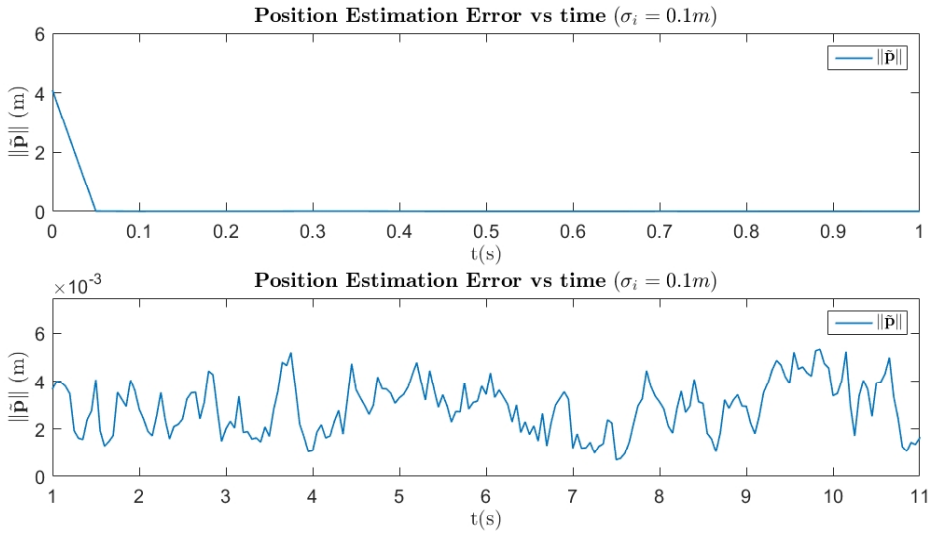

FIGURE 6.7: Position estimation error simulation results, $\sigma_d = 0.1m$

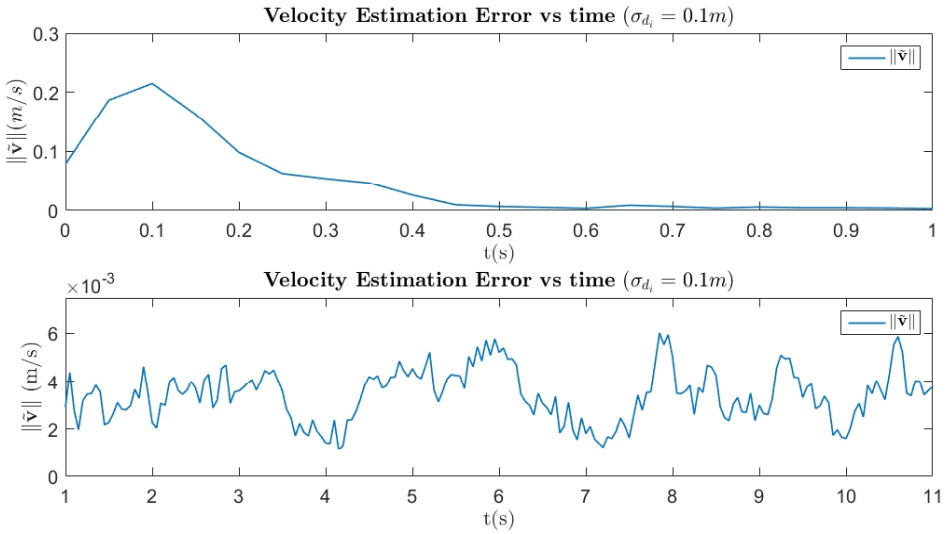

FIGURE 6.8: Velocity estimation error simulation results, $\sigma_d = 0.1m$

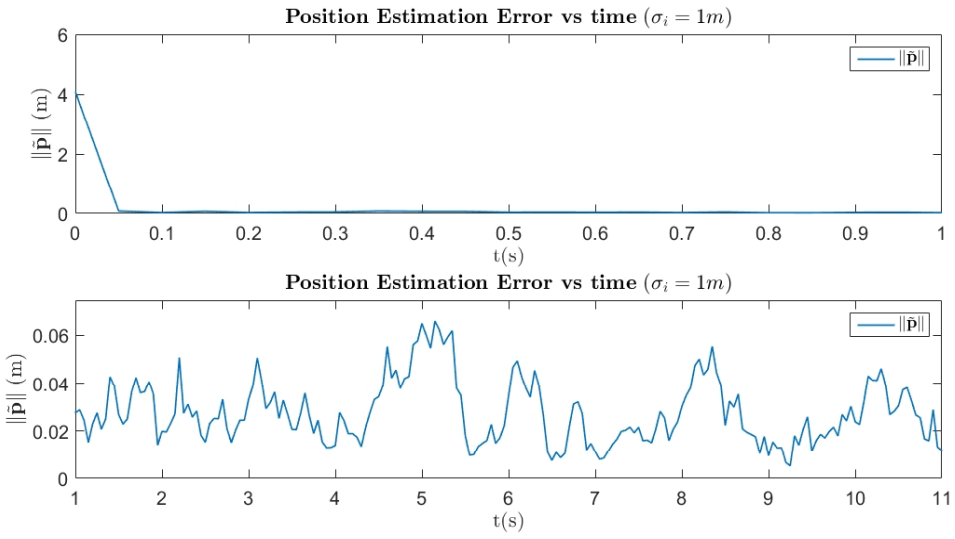

FIGURE 6.9: Position estimation error simulation results, $\sigma_d = 1m$

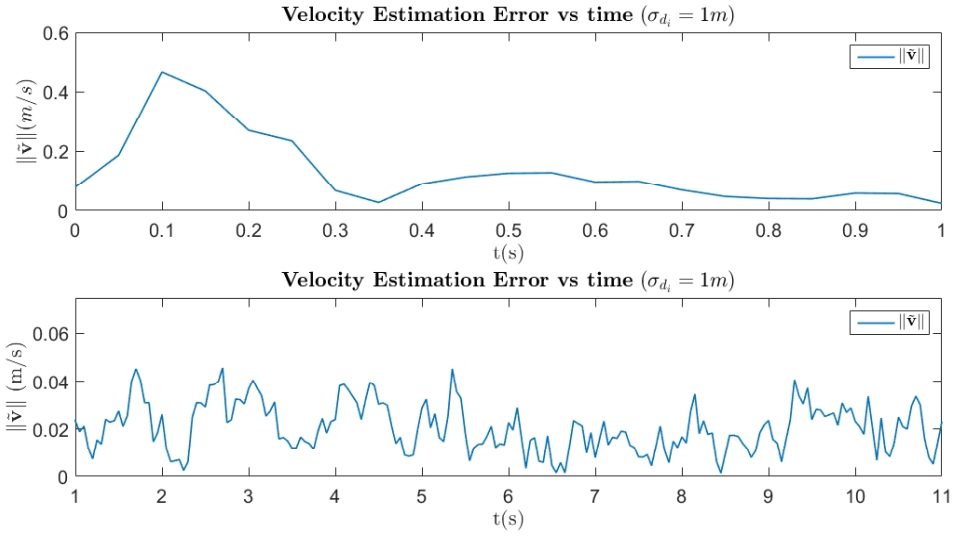

FIGURE 6.10: Velocity estimation error simulation results, $\sigma_d = 1m$

6.3.2 Implementation Results

To test the implementation of this filter, a circle is traced out by attaching the drone to a center point and moving around that circle at an approximately steady pace. The circle to be traced is defined as

$$\begin{aligned} x &= 1.5 + 1.066\cos(2\pi\frac{t}{10.75})\ (m) \\ y &= 2.5 + 1.066\sin(2\pi\frac{t}{10.75})\ (m) \\ z &\approx 2.2\ (m). \end{aligned} \tag{6.25}$$

As shown, the estimator produces good results for both the position and velocity, with some discrepancies in the estimated position and velocity due to misconfiguration of anchor nodes, as well as the imprecise nature of this experiment.

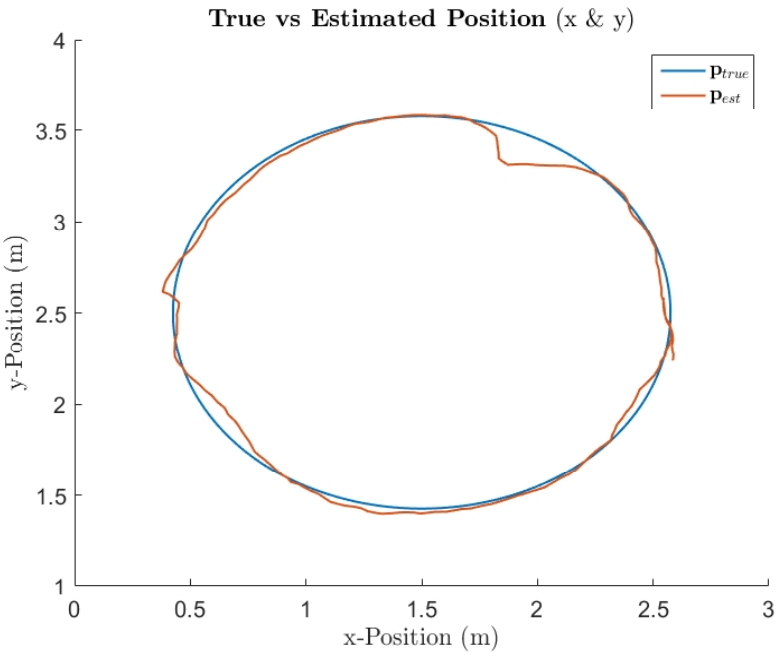

FIGURE 6.11: Kalman filter estimated position, circle test

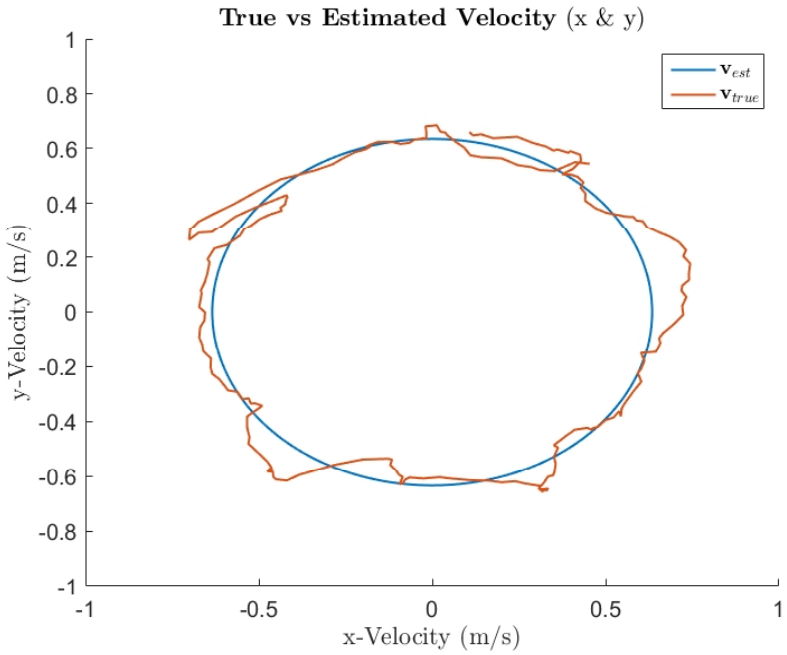

FIGURE 6.12: Kalman filter estimated velocity, circle test

Chapter 7

Experimental Setup

The experimental platform consists of UWB sensors used to estimate position and velocity of the quadrotor UAV in the inertial frame, and the quadrotor UAV itself.

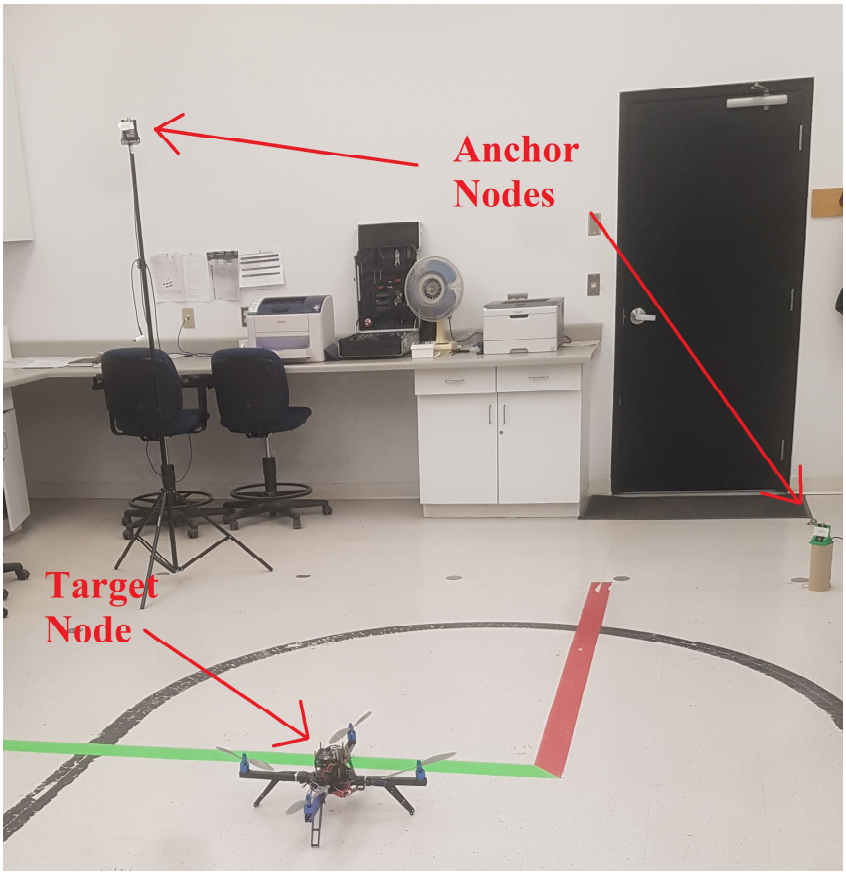

FIGURE 7.1: Full experimental platform showning 2 UWB anchor positions

7.1 Quadrotor UAV

Currently a large number of open-source platforms for quadrotor UAVs exist. Each of these platforms will have their own advantages and disadvantages depending on the type of research conducted. A comparative study of some open-source projects can be found in [70]. The experimental platform chosen for this research is the Arducopter [71] platform previously available

from 3DR robotics [72]. The setup uses the standard Arducopter hardware, with software written using the Arduino C/C++ language.

7.1.1 General Overview

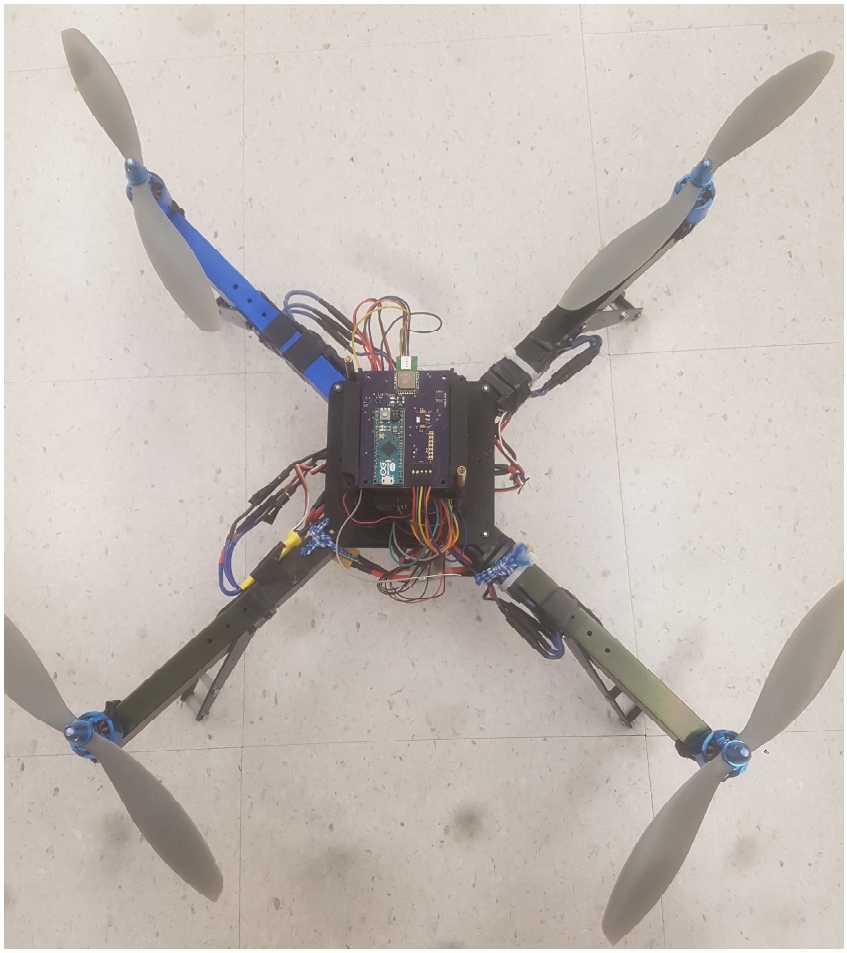

FIGURE 7.2: Quadrotor experimental platform

Shown in fig. 7.2, the Arducopter quadrotor consists of a cross frame of 4 aluminium arms with fibreglass landing legs on each. The motor controllers and ESCs are attached along each arm. Notably, the blue arm denotes the front left of the quadrotor as this platform is being operated in a 'X' setup. At the center of the 4 arms lies the microcontroller and IMU that make flight of this platform possible. Included in Fig. 7.2 is the UWB which is designed in a way that it can be easily attached or removed from the Arducopter platform. Further details of each Arducopter component are discussed in this section and the UWB positioning system in the next.

7.1.2 Microcontroller

The main microcontroller on the APM2.5 control board responsible for the control of the experimental platform is the Amtel AtMega 2560. This is a low-power, 8-bit AVR RISC based microprocessor with 4 USART ports, one hardware Serial Peripheral Interface (SPI), and one

hardware Inter-Integrated Circuit (I^2C) port, each of which is used for communications with peripheral devices. The main loop of this μC is configured to run at 100Hz, meaning controls signals were updated at this rate and data acquisition occurred at this speed as well. The secondary microcontroller responsible for some low level operations as well as programming of the ATMega 2560 is the Amtel ATMega 32U2. This device is responsible for handling radio communications between the users controller and the ArduCopter, it operates on the Ardupilot firmware, as there is no need to alter this.

7.1.3 Inertial Measurement Unit

Included on the APM 2.5 board is an IMU. The IMU on this board contains a 3-axis accelerometer and a 3-axis gyroscope integrated in the MPU6000 [73] as well as a 3-axis magnetometer HMC5883L [74]. Included on the MPU6000 is its own configurable Digital Low Pass Filter (DLPF), with cutoff frequencies ranging from $260Hz \sim 5Hz$ (table 7.1.3) For the purposes of

Accelerometer (Fs = 1kHz)		GyroScope		
Bandwidth(Hz)	Delay(ms)	Bandwidth(Hz)	Delay(ms)	Fs(kHz)
260	0.0	256	0.98	8
184	2.0	188	1.90	1
94	3.0	98	2.80	1
44	4.9	42	4.8	1
21	8.5	20	8.3	1
10	13.8	10	13.4	1
5	19.0	5	18.6	1

TABLE 7.1: Low pass filter configurations for MPU6000

this experiment, the DLPF was configured to have a cut-off frequency of $\sim$ 40Hz to provide good noise filtering. With this configuration it is still capable of detecting high speed manoeuvres, and would always have new data before the 10ms sampling time of the ATMega2560. As well it is possible to configure the output scale of this device depending on which environment it will be operated within. For these experimental trials it was found that a scale of $\pm 4g$ for the accelerometer and $\pm 500^{\circ}/s$ for the gyroscope produced the best results. The magnetometer (HMC5883L), has a full range scale from $\pm$1 Ga to $\pm$8 Ga, as well as automatic and single measurement modes. For automatic mode, the output data rates can be specified from 0.75Hz to 75Hz, in the single measurement mode data rates can be up to 160Hz. For this experiment the full scale reading was set to 1.3Ga as the maximum expected value based on the International Geomagnetic Reference Field (IGRF) for Thunder Bay, Ontario is ~ 541mGa [58], which leaves plenty of room for noise and provides a reasonably accurate result. As the fastest automatic mode of operation for this device is unable to match the speed of the ATMega2560, it was decided that, this device should operate in the single measurement mode, and an interrupt to the host device would be generated whenever data from the HMC5883L was ready, this allows for sampling speeds of $\sim$ 100Hz (from experiments).

7.1.4 Communications

There are three separate communications modules on the experimental platform namely; RC communications, wireless serial communications, and UWB communications. Each of these

modules serves its own individual function. The RC communications module is responsible for desired control inputs when in manual mode. The wireless serial module is used for real time telemetry and diagnostics during flight, and the UWB module is used for position and velocity estimations (discussed in a later section).

The RC radio transmitter responsible for determining the desired attitude and thrust when operating in manual mode is the Turnigy 9XR [75] digital proportional radio controller paired with ORX DSM2 transceivers. The Turnigy 9XR RC controller is capable of outputting 8 separate PPM channels and 9 PCM channels. For this experiments 6 channels are used namely; roll, pitch, yaw, thrust, arm/disarm switch, and manual/position hold switch. The four channels used for attitude and thrust control output a PPM signal corresponding to a value varying from 1000 to 2000 where 1500 is defined as the midpoint. Each of the yaw, pitch, and roll controls return to this mid-point when released while the thrust control will not. These control values are relayed to the APM25 though the 2.4GHz wireless connection from the ORX DSM2 modules, where the roll, pitch, and yaw values are converted to a desired quaternion through [53]

$$Q_d = \begin{bmatrix} \cos(\phi/2)\cos(\theta/2)\cos(\psi/2) + \sin(\phi/2)\sin(\theta/2)\sin(\psi/2) \\ \sin(\phi/2)\cos(\theta/2)\cos(\psi/2) + \cos(\phi/2)\sin(\theta/2)\sin(\psi/2) \\ \cos(\phi/2)\sin(\theta/2)\cos(\psi/2) + \sin(\phi/2)\cos(\theta/2)\sin(\psi/2) \\ \cos(\phi/2)\cos(\theta/2)\sin(\psi/2) + \sin(\phi/2)\sin(\theta/2)\cos(\psi/2) \end{bmatrix} \tag{7.1}$$

The desired attitude is used to determine the control law that generates the control torques used together with the desired thrust to extract the rotor speeds as per e.q. 4.5). Differing from the roll and pitch inputs, the yaw input is handled as a desired angular velocity rather than a desired angle, so that returning the yaw control to the midpoint will stop the rotation, instead of returning the yaw angle back to 0 $^\circ$.

The wireless serial module responsible for telemetry is a USB Zigbee XStick connected to the base station computer and a XBee Series 1 module on the drone [76]. The wireless connection of these two devices operated at 2.4GHz with a serial connection speed configured as 57.6kbaud. This module is used to send information to the base station such as position, attitude, and other diagnostic information. Through a simple Matlab script, it is possible to send new desired positions to the drone, and view real time plots of information received.

7.1.5 Power and Motor Controllers

The entire UAV platform is powered by a 3300mAh 3-Cell LiPo battery, which has a fully charged voltage of 12.4V, and 9.9V when fully discharged. As there is no warning system in place on the experimental platform, it is necessary to keep watch on the battery voltage and to not discharge it past 9.9V as after this it is very dangerous and difficult to recharge the battery. The battery voltage is regulated at $5V$ to operate the two main microcontrollers and the MPU6000 on the APM 2.5, as well this 5V is used to power the attached UWB board (discussed later). This voltage is further down converted to 3.3V to operate the HMC5883L on the APM 2.5, and the DWM1000 module on the UWB boards (discussed later).

The brushless motor and electronic speed controller (ESC) pairs serve as actuators for the drone platform. The ESCs on the drone are controlled by an output PWM signal specified by the ATMega2560 that can vary from 900 to 2100 specifying a pulsewidth of $\sim 0\%$ and $\sim 100\%$ respectively. This PWM signal is used to convert the DC battery voltage to a 3-phase AC signal that is then used to drive the out-runner brushless DC motor at the desired speed. Direct speed

control from these devices is accomplished by measuring the back emf generated in the un-driven coils of the motor.

7.2 UWB Positioning Sensors

The UWB sensor chosen for this project is the DWM1000 UWB module [77]. This device is chosen as it is a fully enclosed UWB communications platform wherein on board registers are accessed through a SPI connection to a host microcontroller. Each of the UWB modules are designed to be exactly the same so that a broken target or broken anchor may easily be replaced with any other module and only a reprogramming is required. For this experiment 4 anchor nodes are placed around a $3 \times 5 \times 2$ rectangular prism wherein the the target node (drone) will move.

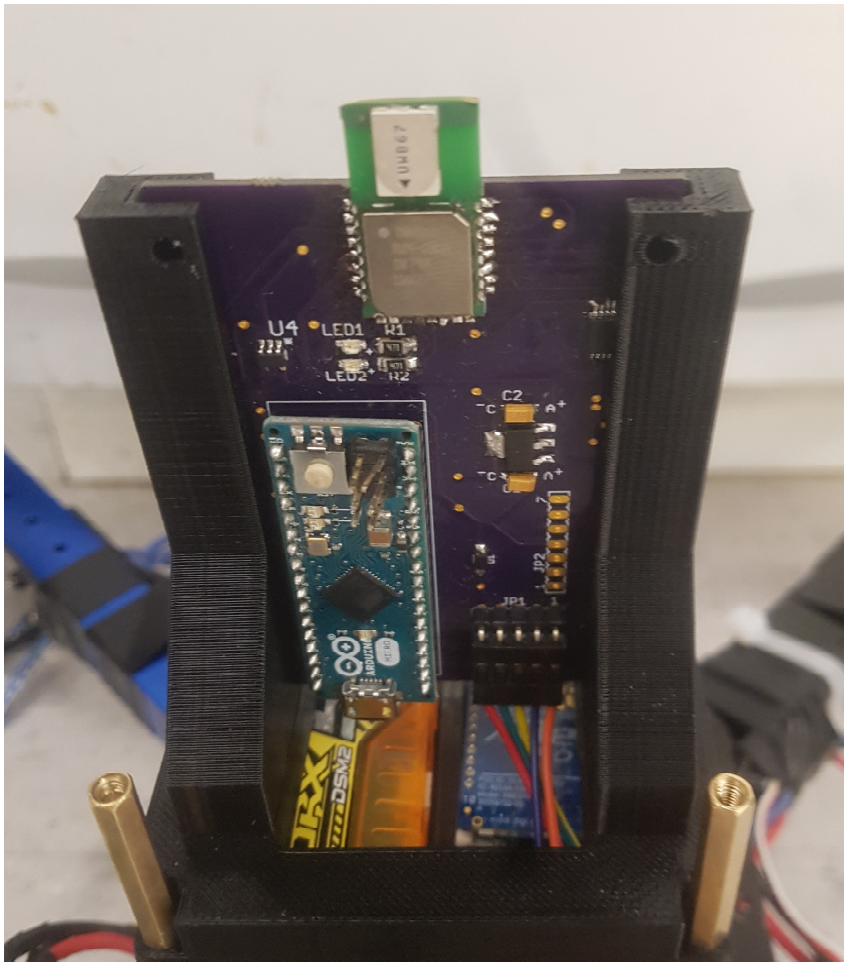

FIGURE 7.3: UWB module mounted on the drone

7.2.1 DWM1000 Module

The DecaWave DWM1000 module is a fully enclosed coherent UWB transceiver, with an integrated antenna, so that no RF design is required. This device communicates to a host microcontroller through the SPI communications protocol. It is capable of a precision up to 10cm,

even at speeds up to 5m/s. Of the available configurations (see [78]) the DWM1000 module was configured to operate at:

- Channel 7 ($\sim 6.5GHz$ centre frequency, $\sim 1GHz$ channel BW)
- $6.8Mbps$ data rate
- $64Mhz$ pulse repetition frequency
- 512 preamble symbols

Through experimental validation these settings provided the most accurate, precise, and reliable distance measurements at the quickest rate possible. It is possible to increase the rate distance measurement by decreasing the number of preamble symbols, but this results in a less accurate distance measurement as mutipath propagation/interference plays a larger role. Although the antennae on the DWM1000 modules are omni-directional they have a more uniform radiation pattern when mounted vertically so all anchor nodes and target node were mounted as such.

7.2.2 Onboard Microcontroller

The controller tasked with handling the UWB communications is a Arduino Micro which utilizes the ATMega32U4 microcontroller. This microcontroller is used to configure the the DWM1000 and handle the localization and ranging procedures. Further, once the UAV position is determined on this device, this information is relayed to the main microcontroller (ATMega2560) through the shared I^2C bus. This secondary microcontroller is utilized as well on the target node to remove the position estimation procedures from the main microcontroller, so that more time is free for position and attitude control.

7.3 Calibration Techniques

As noise and sensor biases are an inherent problem in any real world application, calibration techniques must be employed so that the recovered information is an accurate representation of the real world and therefore useful.

7.3.1 Accelerometer and Gyroscope

As accelerometers and gyroscopes are prone to slowly varying or constant measurement biases it is important to correct for these as best as possible before utilizing this data. To accomplish this, a simple offset correction is utilized assuming these offsets have a constant bias corrupted by an Additive White Gaussian Noise (AWGN), the three step process is given as

1. A set of 'N' data points are taken while the drone is at a known constant orientation (*e.g.* $\mathbf{R} = \mathbf{I}_{3\times 3}$)
2. These data points are compared with expected values to determine the average error
3. The average error is then subtracted from measurements during run-time

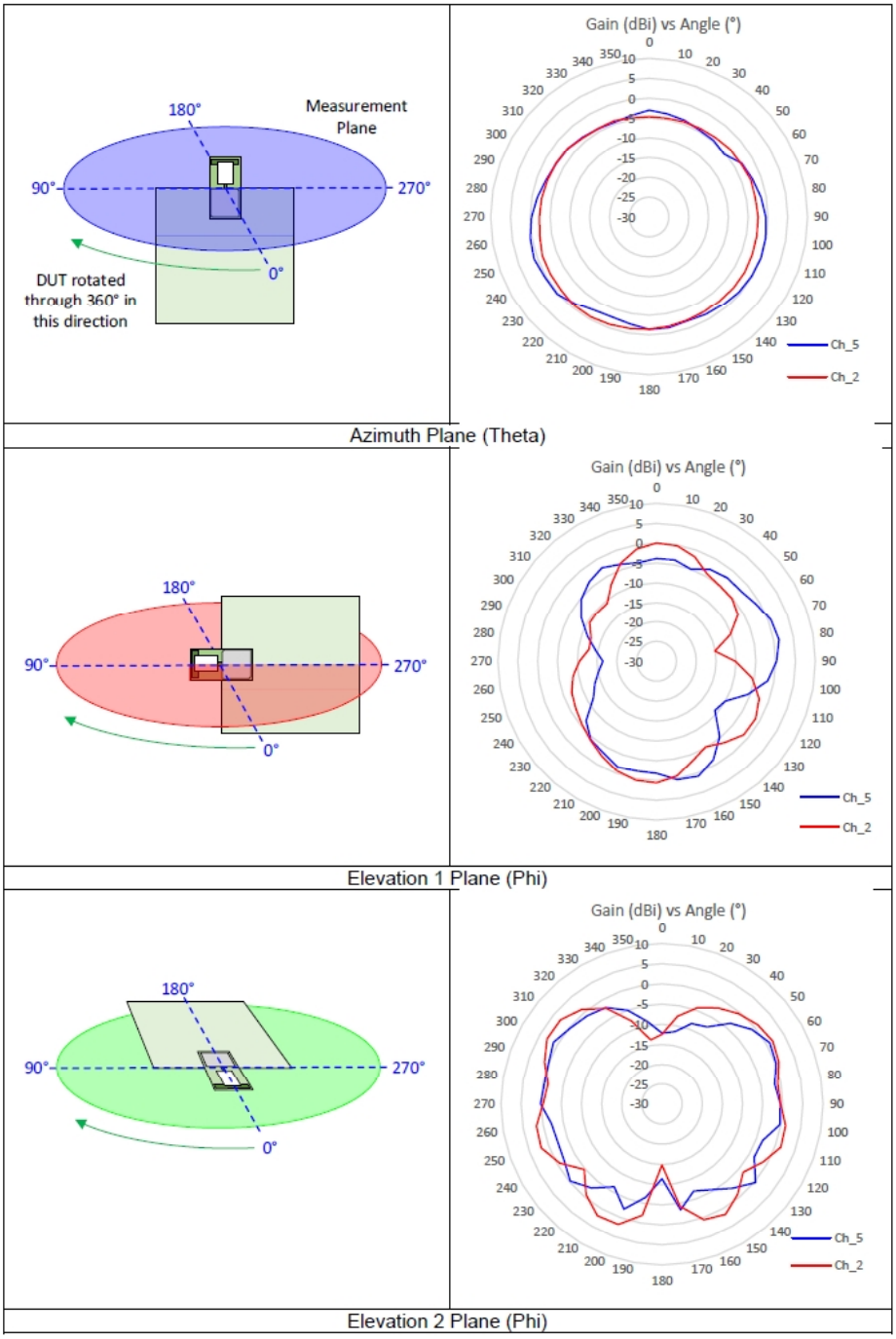

FIGURE 7.4: DWM1000 antenna radiation pattern [79]

Accelerometer Calibration

The accelerometer measures the instantaneous acceleration of the drone in the body frame expressed as

$$\mathbf{a}_{\mathcal{B}} = \mathbf{R}^T \left(\mathbf{a}_{\mathcal{I}} - g\hat{\mathbf{e}}_3 \right) + \mathbf{b}_a + \boldsymbol{\eta}_a, \tag{7.2}$$

where $\mathbf{a}_{\mathcal{I}}$ is the linear acceleration in the inertial frame, $\mathbf{b}_a$ is the constant bias term and $\boldsymbol{\eta}_a$ the AWGN term. While keeping the drone stationary ($\mathbf{a}_{\mathcal{I}} = [0\ 0\ 0]^T$), at the orientation $\mathbf{R} = \mathbf{I}_{3\times3}$ the bias term can be estimated through

$$\hat{\mathbf{b}}_a = \frac{1}{N}\sum_{i=1}^{N} \mathbf{a}_{\mathcal{B}}(i) + g\hat{\mathbf{e}}_3, \tag{7.3}$$

where $\mathbf{a}_{\mathcal{B}}(i)$ denotes the i^{th} measurement of the body-fixed acceleration at rest. The offset term $\hat{\mathbf{b}}_a$ can now be subtracted from measurements during run-time.

Gyroscope Calibration

The gyroscope measures the instantaneous angular velocity of the drone expressed in the body frame expressed as

$$\Omega_{\mathcal{B}} = \Omega + \mathbf{b}_g + \boldsymbol{\eta}_g, \tag{7.4}$$

where $\Omega_{\mathcal{B}}$ is the measured angular velocity in the body frame, Ω is the true angular velocity in the body frame, $\mathbf{b}_g$ is a slow time varying bias term, and $\boldsymbol{\eta}_g$ the AWGN term. The term $\mathbf{b}_g$ can be broken into a constant offset $\mathbf{b}_{g_c}$, as well as a time-varying offset $\mathbf{b}_g(t)$, as

$$\mathbf{b}_g = \mathbf{b}_{g_c} + \mathbf{b}_g(t),$$

by maintaining the drone at the constant orientation $\mathbf{R} = \mathbf{I}_{3\times3}$, with $\Omega = 0$, the term $\mathbf{b}_{g_c}$ can now be estimated through

$$\hat{\mathbf{b}}_{g_c} = \frac{1}{N}\sum_{i=1}^{N} \Omega_{\mathcal{B}}(i), \tag{7.5}$$

where $\Omega_{\mathcal{B}}(i)$ is the i^{th} angular velocity measurement while the UAV is at rest. Although the full term $\mathbf{b}_g$ may be estimated through eq. 5.7 this initial calibration will lower the bound Δ thus improving the performance of the attitude observer.

7.3.2 Propeller Efficiency

As information about propeller thrust coefficients may be imprecise and as propellers often become damaged, it is important to determine the current efficiency of each propeller. This is accomplished by first assuming all propellers are 100% efficient, then performing a flight wherein the quadrotor is held as stationary as possible. From this flight, each rotor speed is recovered and then averaged and compared to the expected data for a hover condition where $\dot{\mathbf{v}} = 0$ *i.e.* $g\hat{\mathbf{e}}_3 = \frac{\mathcal{T}}{m}$. From eq. 4.4 the total thrust is defined as a function of rotor speeds, and under the hover assumption it is also possible to say that each rotor produces $1/4$ of the total thrust, or

$$\frac{mg}{4} = \eta_i b\overline{\omega}_i^2. \tag{7.6}$$

where η_i is the efficiency of the i^{th} rotor. For a perfectly efficient rotor, the left and right hand sides of eq. 7.6 will be exactly matched when $\eta_i = 1$. As this is not the case, this equation can be re-arranged to determine each propeller efficiency as

$$\eta_i = \frac{mg}{4b\overline{\omega}_i^2}. \tag{7.7}$$

The inverse of the efficiency

$$c_i := \tfrac{1}{\eta_i},$$

is then utilized as a multiplier to correct for the efficiency of each propeller. These constants are found for the current propellers to be

$$c_1 = 1.6213 \quad c_2 = 1.6383 \quad c_3 = 1.5961 \quad c_4 = 1.5961. \tag{7.8}$$

Such large discrepancies from $\eta_i = 1$ may be due to uncertainties in propeller modelling and propeller speed.

7.3.3 Magnetometer Calibration

The magnetometer provides a measurement of of the ambient magnetic field which is defined by

$$\mathbf{m}_{\mathcal{B}} = \mathbf{D}\mathbf{R}^T\mathbf{m}_{\mathcal{I}} + \mathbf{b}_m + \boldsymbol{\eta}_m, \tag{7.9}$$

where, $\mathbf{D}$ is the distortion of the measured field, $\mathbf{m}_{\mathcal{I}}$ is the earth magnetic field at the current location, η_m an AWGN term, and $\mathbf{b}_m$ is a disturbance modelled as

$$\mathbf{b}_m = \boldsymbol{\varrho} + I_{batt}\boldsymbol{\lambda}, \tag{7.10}$$

with I_{batt} being the instantaneous current sourced from the battery, $\boldsymbol{\lambda}$ a constant 3×1 vector multiplier relating the current to an induced magnetic field, and $\boldsymbol{\varrho}$ a constant 3×1 vector of the magnetic field offsets.

Distortion ($\mathbf{D}$) and $\boldsymbol{\varrho}$ Estimate

Utilizing the method described in [24] where the distortion matrix is given by

$$\mathbf{D} = \begin{bmatrix} \epsilon_x & 0 & 0 \\ \epsilon_y \sin\delta_x & \epsilon_y \cos\delta_x & 0 \\ \epsilon_z \sin\delta_y \cos\delta_z & \epsilon_z \sin\delta_z & \epsilon_z \cos\delta_y \cos\delta_z \end{bmatrix} \quad \mathbf{b}_m = \begin{bmatrix} \varrho_x \\ \varrho_y \\ \varrho_z \end{bmatrix}, \tag{7.11}$$

which is true under the assumption that while the motors are off, $I_{batt} \approx 0$. In the above, the ϵ variables describe constant scaling offsets, and the variables related to δ correspond to the sensor misalignment angles. Disregarding the AWGN term and assuming $I_{batt} = 0$, eq. 7.9 can be rearranged as

$$\mathbf{R}^T\mathbf{m}_{\mathcal{I}} = \mathbf{D}^{-1}\left(\mathbf{m}_{\mathcal{B}} - \boldsymbol{\varrho}\right) \tag{7.12}$$

Taking the norm of both sides of eq. 7.12, this can be rewritten as

$$\begin{aligned} C_1 m_{\mathcal{B}_x}^2 + C_2 m_{\mathcal{B}_x} m_{\mathcal{B}_y} + C_3 m_{\mathcal{B}_x} m_{\mathcal{B}_z} + C_4 m_{\mathcal{B}_y}^2 + C_5 m_{\mathcal{B}_y} m_{\mathcal{B}_z} \\ + C_6 m_{\mathcal{B}_z}^2 + C_7 m_{\mathcal{B}_x} + C_8 m_{\mathcal{B}_y} + C_9 m_{\mathcal{B}_z} = C_{10}, \end{aligned} \tag{7.13}$$

where $\|\mathbf{m}_{\mathcal{I}}\|$ is the norm of the inertially referenced magnetic field and C_i, $i \in \{1, \ldots, 10\}$ are functions of the parameters ϵ, δ, ϱ. Which, may be given, by first taking note that

$$\mathbf{D}^{-1} = \begin{bmatrix} D_1 & 0 & 0 \\ D_2 & D_3 & 0 \\ D_4 & D_6 & D_6 \end{bmatrix}, \tag{7.14}$$

where

$$\begin{aligned} D_1 &= \frac{1}{\epsilon_x} \\ D_2 &= -\frac{\tan\delta_x}{\epsilon_x} \\ D_3 &= \frac{1}{\epsilon_y \cos\delta_x} \\ D_4 &= \frac{\tan\delta_x \tan\delta_z - \tan\delta_y \cos\delta_y}{\epsilon_x \cos\delta_y} \\ D_5 &= -\frac{\tan\delta_z}{\epsilon_y \cos\delta_x \cos\delta_y} \\ D_6 &= \frac{\epsilon_x \cos\delta_y}{\cos\delta_z}. \end{aligned} \tag{7.15}$$

Then the 10 coefficients, $C_1, \ldots, C_{10}$, given as functions of $D_1, \ldots, D_6$ are as following:

$$\begin{aligned} C_1 &= D_1^2 + D_2^2 + D_4^2 \\ C_2 &= 2D_2D_3 + 2D_4D_5 \\ C_3 &= 2D_4D_6 \\ C_4 &= D_3^2 + D_5^2 \\ C_5 &= 2D_5D_6 \\ C_6 &= D_6^2 \\ C_7 &= -2\varrho_x\left(D_1^2 + D_2^2 + D_4^2\right) - 2\varrho_y\left(D_2D_3 + D_4D_5\right) - 2\varrho_z D_4D_6 \\ C_8 &= -2\varrho_x\left(D_2D_3 + D_4D_5\right) - 2\varrho_y\left(D_3^2 + D_5^2\right) - 3\varrho_z D_5D_6 \\ C_9 &= -2\varrho_x D_4D_6 - 2\varrho_y D_5D_6 - 2\varrho_z D_6^2 \\ C_{10} &= \|m_{\mathcal{I}}\|^2 - \varrho_x^2\left(D_1^2 + D_2^2 + D_4^2\right) - \varrho_y^2\left(D_3^2 + D_5^2\right) - \varrho_z^2 D_6^2 + 2\varrho_x\left(D_1 + D_2 + D_3\right) \\ &\quad + 2\varrho_y\left(D_3 + D_5\right) - 2\varrho_z D_6 - 2\varrho_x\varrho_y\left(D_2D_3 + D_4D_5\right) - 2\varrho_x\varrho_z D_4D_6 - 2\varrho_y\varrho_z D_5D_6. \end{aligned} \tag{7.16}$$

The C_i values are determined by taking a large number (N) of samples then using a least squares estimator on the equation

$$\mathbb{X}\mathbb{C} = \mathbb{W}, \tag{7.17}$$

where

$$\mathbb{X} = \begin{bmatrix} m_{\mathcal{B}_x}^2(1) & m_{\mathcal{B}_x}(1)m_{\mathcal{B}_y}(1) & \cdots & m_{\mathcal{B}_z}(1) \\ m_{\mathcal{B}_x}^2(2) & m_{\mathcal{B}_x}(2)m_{\mathcal{B}_y}(2) & \cdots & m_{\mathcal{B}_z}(2) \\ \vdots & \vdots & \ddots & \vdots \\ m_{\mathcal{B}_x}^2(N) & m_{\mathcal{B}_x}(N)m_{\mathcal{B}_y}(N) & \cdots & m_{\mathcal{B}_z}(N) \end{bmatrix} \quad \mathbb{C} = \begin{bmatrix} C_1/C_{10} \\ C_2/C_{10} \\ \vdots \\ C_9/C_{10} \end{bmatrix} \quad \mathbb{W} = \begin{bmatrix} 1 \\ 1 \\ \vdots \\ 1 \end{bmatrix},$$

then $\mathbb{C}$ is determined by

$$\mathbb{C} = \left(\mathbb{X}^T\mathbb{X}\right)^{-1}\mathbb{X}^T\mathbb{W}. \tag{7.18}$$

These values of C_i are then used to determine the 6 elements of the distortion matrix $\mathbf{D}$. This matrix $\mathbf{D}$ is then used to generate the corrected body referenced magnetic field through

$$\mathbf{m}_{\mathcal{B}_{corr}} = \mathbf{R}^T\mathbf{m}_{\mathcal{I}} = \mathbf{D}^{-1}\left(\mathbf{m}_{\mathcal{B}} - \boldsymbol{\varrho}\right). \tag{7.19}$$

Without this correction, the measured magnetic field will vary greatly in size, and as well the distortion will cause large errors in the attitude estimation (see figure 7.8).

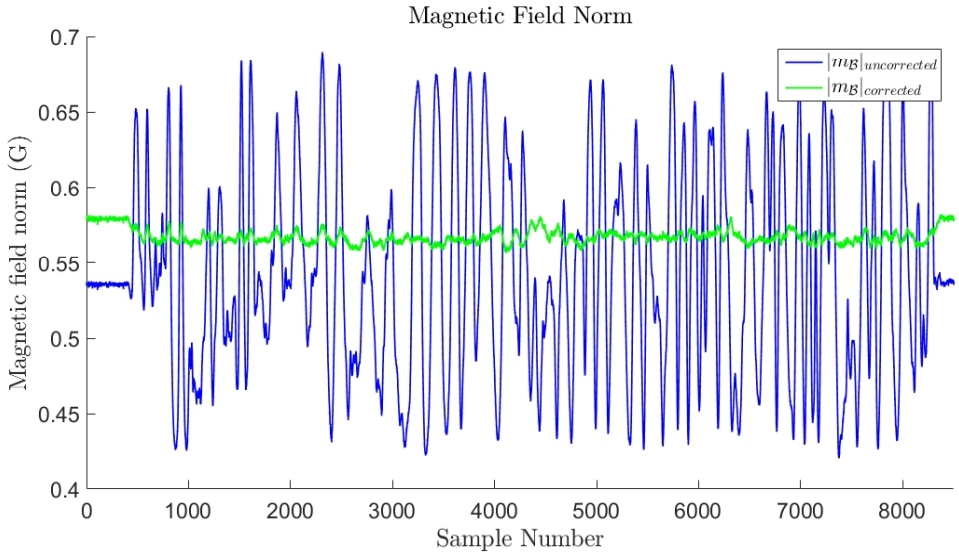

FIGURE 7.5: Corrected vs uncorrected magnetic field norm

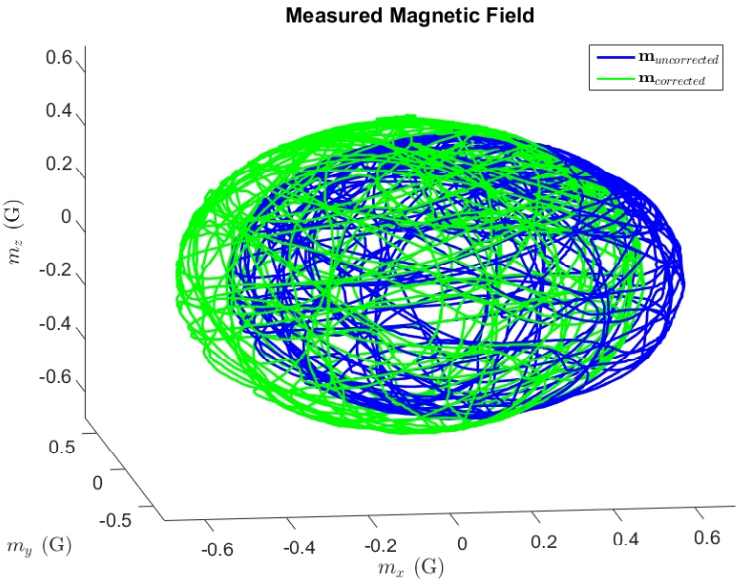

FIGURE 7.6: Corrected vs uncorrected magnetic field

λ Estimate

While the motors of the quadrotor UAV are operating the battery will source current and thus a magnetic field will be created. This induced magnetic field will heavily affect the magnetic field measured by the magnetometer and will in turn affect the attitude estimation. To mitigate the effects of this magnetic field a correcting factor $\boldsymbol{\lambda}$ is introduced. The correlation between the

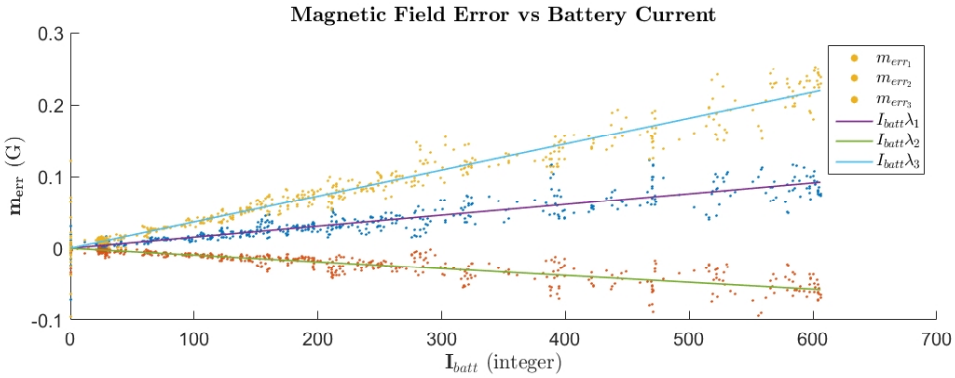

FIGURE 7.7: Magnetic field error versus measured current, $\mathbf{R} = \mathbf{I}_{3\times3}$

induced magnetic field and the battery current is assumed as approximately linear, and the correcting term can be assumed constant. With this, the measured magnetic field can be represented as

$$\mathbf{m}_{meas} = \mathbf{m}_0 + I_{batt}\boldsymbol{\lambda}, \tag{7.20}$$

where $\mathbf{m}_0$ is the expected magnetic field, which, for $\mathbf{R} = \mathbf{I}_{3\times3}$ is $\mathbf{m}_0 = \mathbf{m}_{\mathcal{I}}$, $\boldsymbol{\lambda}$ is the unknown scaling factor for each axis and I_{batt} the instantaneous current drawn from the battery. The term $\boldsymbol{\lambda}$ can then be estimated by increasing the rotor speeds from 0 to the maximum value while measuring both, the instantaneous battery current and magnetic field. The error is then determined as

$$\mathbf{m}_{error} \approx \boldsymbol{\lambda} I_{batt} = \mathbf{m}_0 - \mathbf{m}_{meas}. \tag{7.21}$$

In Figure.7.7 the plot of the magnetic error vs the battery current shows the approximately linear relationship between the two.

By taking this set of data points and arranging them into two vectors: $\bar{\mathbf{I}}_{batt} \in \mathbb{R}^{1\times N}$ and $\overline{\mathbf{m}}_{error} \in \mathbb{R}^{3\times N}$. A least squares estimate of $\boldsymbol{\lambda}$ can be determined as

$$\boldsymbol{\lambda} = \left(\bar{\mathbf{I}}_{batt}^T \bar{\mathbf{I}}_{batt}\right)^{-1} \bar{\mathbf{I}}_{batt}^T \overline{\mathbf{m}}_{error}, \tag{7.22}$$

where $\bar{\mathbf{I}}_{batt}$ and $\overline{\mathbf{m}}_{error}$ are the measured vectors of battery current and magnetic field error respectively. The error due to the battery current causes a large error in the attitude estimation if not compensated for. If not compensated for the yaw angle will drift causing the position control to fail.

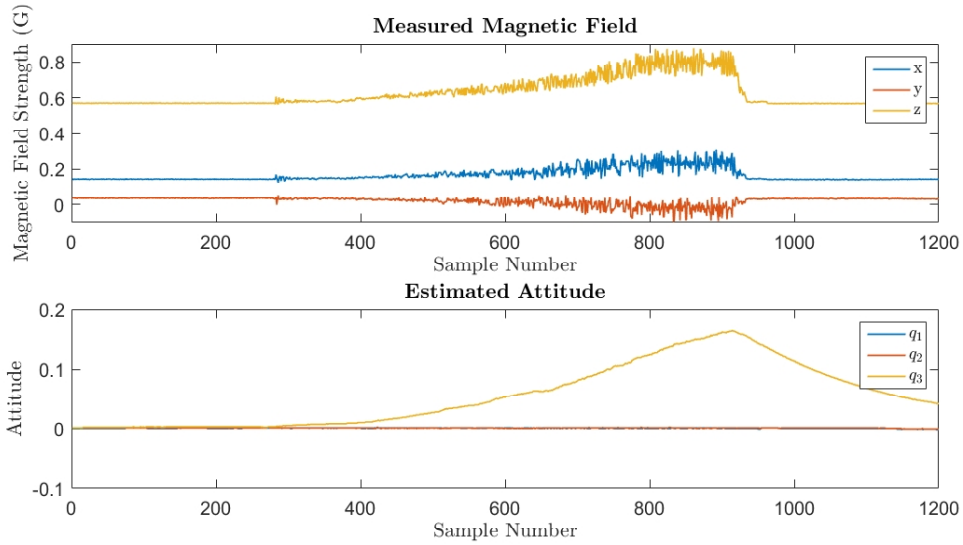

FIGURE 7.8: Induced magnetic field and corresponding attitude error

7.3.4 UWB Antenna Delay Calibration

As exact parameters of the antenna are unknown, the time delay induced by the signal being received at and travelling through the antenna is also unknown. Due to the high precision of this system, this unknown delay may cause drastic errors in the distance estimation and as such must be accounted for. To account for this delay, the target node is set at a known distance from the anchor node and a set of measurements are taken, the error can then be modelled as

$$t_{error} = t_{meas} - t_{expected}, \tag{7.23}$$

where $t_{expected}$ is determined from

$$t_{expected} = \frac{d_{true}}{c},$$

with both d_{true} and c known, the average error can then be determined. This process is completed for all anchors communicating with the target node, the average errors are then stored in the target node and subtracted during runtime.

Chapter 8

Position Control Using Simplified Approach

The translational and rotational dynamics of the quadrotor UAV are given by

$$\begin{aligned} \dot{\mathbf{p}} &= \mathbf{v} \\ \dot{\mathbf{v}} &= g\hat{\mathbf{e}}_3 - \frac{\mathcal{T}}{m}\mathbf{R}^T\hat{\mathbf{e}}_3 \\ \dot{Q} &= \frac{1}{2}\begin{bmatrix} -q^T \\ q_o\mathbf{I}_{3\times 3} + S(q) \end{bmatrix}\Omega \\ I_b\dot{\Omega} &= -S(\Omega)I_b\Omega + \boldsymbol{\tau}_a. \end{aligned} \tag{8.1}$$

As the position of the VTOL UAV is not directly controllable, it must be controlled indirectly through the total system thrust and the orientation of the device. This can be done in a number of ways, due to the complex nature of this process, a simplified controller is introduced. This controller will be broken into three segments:

1. Point Mass Position Controller
2. Attitude Extraction Map
3. Attitude Controller

8.1 Virtual Control Design for Translational Dynamics

The simplified block diagram of the full quadrotor control system is shown in Fig.8.1, the virtual control ($\boldsymbol{\mu}_d$) is generated by the position control block. This virtual control is then used to specify a desired orientation and thrust, which in turn controls the position of the VTOL UAV. Choosing

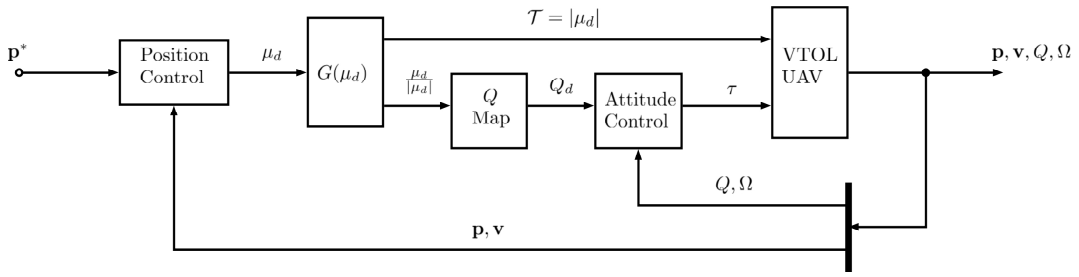

FIGURE 8.1: Block diagram of simplified position controller

the desired reference as $\mathbf{r}(t)$, we can then define the position error as

$$\tilde{\mathbf{p}} := \mathbf{p} - \mathbf{r}(t),$$

and the velocity error as

$$\tilde{\mathbf{v}} := \mathbf{v} - \dot{\mathbf{r}}(t),$$

defining the system acceleration

$$\boldsymbol{\mu} := g\hat{\mathbf{e}}_3 - \frac{\mathcal{T}}{m}\mathbf{R}^T\hat{\mathbf{e}}_3.$$

The translational error dynamics can be rewritten as

$$\begin{aligned} \dot{\tilde{\mathbf{p}}} &= \tilde{\mathbf{v}} \\ \dot{\tilde{\mathbf{v}}} &= \boldsymbol{\mu} - \ddot{\mathbf{r}}(t). \end{aligned} \tag{8.2}$$

Moreover, defining the acceleration error as

$$\tilde{\boldsymbol{\mu}} := \boldsymbol{\mu} - \boldsymbol{\mu}_d,$$

the translational dynamics can then be written in terms of a desired system acceleration

$$\begin{aligned} \dot{\tilde{\mathbf{p}}} &= \tilde{\mathbf{v}} \\ \dot{\tilde{\mathbf{v}}} &= \boldsymbol{\mu}_d + \tilde{\boldsymbol{\mu}} - \ddot{\mathbf{r}}(t). \end{aligned} \tag{8.3}$$

At this stage, one can design the desired acceleration $\boldsymbol{\mu}_d$ as a virtual control assuming that $\tilde{\boldsymbol{\mu}} = 0$, as follows:

$$\boldsymbol{\mu}_d = -\frac{k_p}{\sqrt{3}}\tanh(\tilde{\mathbf{p}}) - \frac{k_v}{\sqrt{3}}\tanh(\tilde{\mathbf{v}}) + \ddot{\mathbf{r}}(t). \tag{8.4}$$

Consider the following candidate Lyapunov function

$$\mathcal{V} = \frac{k_p}{\sqrt{3}}[1\ 1\ 1]\log(\cosh(\tilde{\mathbf{p}})) + \tilde{\mathbf{v}}^T\tilde{\mathbf{v}}, \tag{8.5}$$

which, in view of (8.3) and (8.4), leads to the following time derivative

$$\dot{\mathcal{V}} = -\frac{k_v}{\sqrt{3}}\tilde{\mathbf{v}}^T\tanh(\tilde{\mathbf{v}}), \tag{8.6}$$

which is negative semi-definite, guaranteeing the boundedness of the states $\tilde{\mathbf{p}}$ and $\tilde{\mathbf{v}}$. Invoking LaSalle invariance principle, it can be seen that $\tilde{\mathbf{p}} \to 0$ as $t \to \infty$ through the following:

$$\dot{\mathcal{V}} = 0 \Rightarrow \tilde{\mathbf{v}} = 0 \Rightarrow \dot{\tilde{\mathbf{v}}} = 0, \tag{8.7}$$

which with 8.3 and 8.4 gives

$$\dot{\tilde{\mathbf{v}}} = 0 = -\frac{\tanh(\tilde{\mathbf{p}})}{\sqrt{3}}, \tag{8.8}$$

or equivalently

$$\tilde{\mathbf{p}} = 0. \tag{8.9}$$

One can also show $\boldsymbol{\mu}_d$ is bounded by

$$\|\boldsymbol{\mu}_d\| \leq \|\frac{k_p}{\sqrt{3}}\tanh(\tilde{\mathbf{p}})\| + \|\frac{k_v}{\sqrt{3}}\tanh(\tilde{\mathbf{v}})\| + \|\ddot{\mathbf{r}}(t)\| \leq k_p + k_v + \delta_r, \tag{8.10}$$

where δ_r is an upper bound on the second derivative of the pre-defined trajectory. If for example, the goal is to achieve position regulation of the VTOL UAV, the reference trajectory will be defined

$$\mathbf{r}(t) = C,$$

and as such $\ddot{\mathbf{r}}(t) = 0$, thus the control will be bounded by $k_p + k_v$.

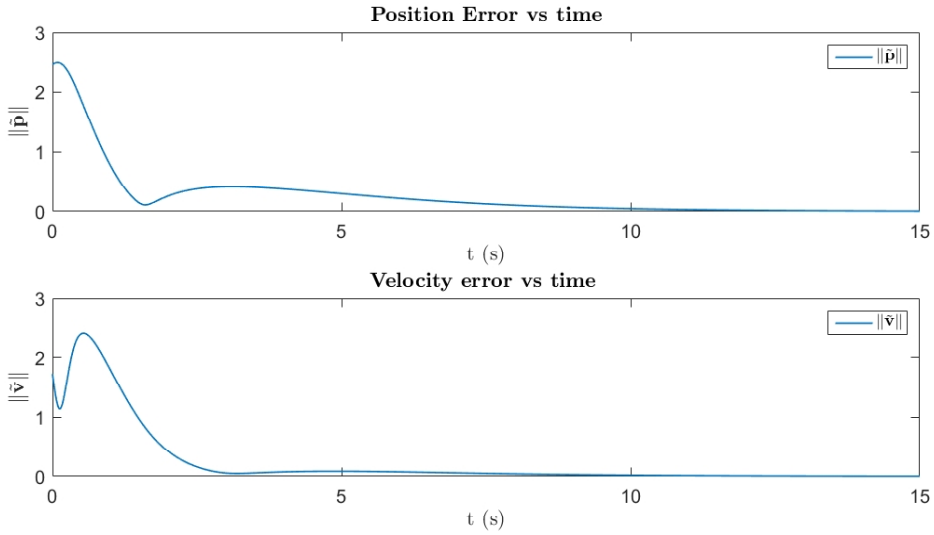

FIGURE 8.2: Simulation results for point mass position controller, $[\tilde{\mathbf{p}}_0^T,\ \tilde{\mathbf{v}}_0^T]^T = [-3\ 1\ 1,\ 1\ 1\ \ -1]^T$

It can be seen from simulation results that the bounded controller will stabilize the position even with a large set of initial conditions.

8.2 Attitude Extraction Map

Now, the thrust and desired attitude can be extracted from the virtual control law $\boldsymbol{\mu}_d$ as per the mapping defined in [51], in which if given two vectors v and u where $\|v\| = \|u\|$ and $u \neq -v$ the mapping that satisfies $\mathbf{R}_d u = v$ can be found through the quaternion relationship

$$\overline{v} = Q_d^{-1} \odot \overline{u} \odot Q_d.$$

From the definition of the quaternion eq. 3.4, and knowing

$$\begin{aligned} u^T v &= \|u\|\|v\|\cos(\gamma) \\ S(v)u &= \|u\|\|v\|\sin(\gamma)\hat{k}, \end{aligned}$$

one can determine, in view of the fact that $\|\mathbf{u}\| = \|\mathbf{v}\|$, the following relationships:

$$\begin{aligned} \cos(\gamma) &= \frac{u^T v}{\|u\|^2} \\ \sin(\gamma) &= \frac{\sqrt{(\|u\|^2 + u^T v)(\|u\|^2 - u^T v)}}{\|u\|^2}. \end{aligned}$$

Applying the double angle relationship $\cos(\gamma) = 1 - 2\sin^2(\gamma/2)$, one obtains

$$\sin(\gamma/2) = \sqrt{\frac{\|u\|^2 - u^T v}{2\|u\|^2}},$$

from which, the vector portion of the quaternion is determined

$$\begin{aligned} q &= \sin(\gamma/2)\hat{k} \\ &= \left(\sqrt{\frac{\|u\|^2 - u^T v}{2\|u\|^2}}\right)\left(\frac{1}{\sqrt{(\|u\|^2 + u^T v)(\|u\|^2 - u^T v)}}\right) S(v)u \\ &= \frac{1}{\|u\|}\sqrt{\frac{1}{2(\|u\|^2 + u^T v)}} S(v)u. \end{aligned} \tag{8.11}$$

Applying the relationship $2\sin(\gamma/2)\cos(\gamma/2) = \sin(\gamma)$, the real portion of the quaternion is found as

$$\begin{aligned} q_o &= \cos(\gamma/2) \\ &= \frac{\sin(\gamma)}{2\sin(\gamma/2)} \\ &= \frac{1}{\|u\|}\sqrt{\frac{\|u\|^2 + u^T v}{2}}. \end{aligned} \tag{8.12}$$

Using (8.11) and (8.12) with

$$\begin{aligned} u &= \frac{g\hat{\mathbf{e}}_3 - \boldsymbol{\mu}_d}{\|g\hat{\mathbf{e}}_3 - \boldsymbol{\mu}_d\|} \\ v &= \hat{\mathbf{e}}_3, \end{aligned}$$

one obtains

$$\begin{aligned} q_{0_d} &= \sqrt{\frac{1}{2}\left(1 + \frac{g - \mu_{d_3}}{\|\boldsymbol{\mu}_d - g\hat{\mathbf{e}}_3\|}\right)} := f_{q_o}(\boldsymbol{\mu}_d) \\ q_d &= \frac{1}{2\|\boldsymbol{\mu}_d - g\hat{\mathbf{e}}_3\| q_o}\begin{bmatrix} \mu_{d_2} \\ -\mu_{d_1} \\ 0 \end{bmatrix} := f_q(\boldsymbol{\mu}_d). \end{aligned} \tag{8.13}$$

Now, since $\boldsymbol{\mu}_d := g\hat{\mathbf{e}}_3 - \frac{\mathcal{T}}{m}\mathbf{R}_d^T\hat{\mathbf{e}}_3$, it is clear that

$$\mathcal{T} = m\|g\hat{\mathbf{e}}_3 - \boldsymbol{\mu}_d\|. \tag{8.14}$$

Therefore,

$$\mathbf{R}_d \frac{g\hat{\mathbf{e}}_3 - \boldsymbol{\mu}_d}{||g\hat{\mathbf{e}}_3 - \boldsymbol{\mu}_d||} = \hat{\mathbf{e}}_3. \tag{8.15}$$

As the term $\|\boldsymbol{\mu}_d - g\hat{\mathbf{e}}_3\|$ appears in the denominator of the desired quaternion, it must be ensured that this term never vanishes. This is achieved through the *a priori* boundedness of $\boldsymbol{\mu}_d$, if the gains k_p and k_v are chosen adequately small, along with the choice of a well bounded desired acceleration. This condition is expressed through

$$0 < \|\boldsymbol{\mu}_d - g\hat{\mathbf{e}}_3\|, \tag{8.16}$$

or, equivalently

$$|\mu_{d_3}| < g, \tag{8.17}$$

from (8.4), one can see that

$$|\mu_{d_3}| \leqslant \frac{k_p + k_v}{\sqrt{3}} + \delta_r \tag{8.18}$$

giving

$$\frac{k_p + k_v}{\sqrt{3}} + \delta_r < g. \tag{8.19}$$

8.3 Attitude Controller

The desired attitude is then used as the setpoint for the attitude controller. The attitude error can be given as

$$\begin{array}{rcl} \tilde{\mathbf{R}} & = & \mathbf{R}\mathbf{R}_d^T \\ & \text{or} & \\ \tilde{Q} & = & Q_d^{-1} \odot Q, \end{array} \tag{8.20}$$

which leads to the error dynamics

$$\begin{aligned} \dot{\tilde{Q}} &= \frac{1}{2}\begin{bmatrix} -\tilde{q} \\ \tilde{q}_o\mathbf{I}_{3\times 3} + S(\tilde{q}) \end{bmatrix}\Omega \\ \mathbf{I}_b\dot{\Omega} &= -S(\Omega)\mathbf{I}_b\Omega + \boldsymbol{\tau}_a. \end{aligned} \tag{8.21}$$

Where the desired angular velocity Ω_d is 0, so that $\tilde{\Omega} = \Omega$. and the control input $\boldsymbol{\tau}$ is determined from the model independant control defined in [35]

$$\boldsymbol{\tau} = -\Gamma\Omega - \alpha_q\tilde{q}, \tag{8.22}$$

where $\Gamma = \Gamma^T > 0$ and $\alpha_q > 0$. Choosing the Lyapunov function candidate

$$\mathcal{V} = \alpha_q\tilde{q}^T\tilde{q} + \alpha_q(\tilde{q}_o - 1)^2 + \frac{1}{2}\Omega^T\mathbf{I}_b^{-1}\Omega \tag{8.23}$$

which has the following time derivative along the trajectories of (8.21):

$$\dot{\mathcal{V}} = \alpha_q\tilde{q}_o\tilde{q}^T\Omega + \alpha_q\tilde{q}^TS(\tilde{q})\Omega - \alpha_q\tilde{q}_o\tilde{q}^T\Omega + \alpha_q\tilde{q}^T\Omega - \Omega^TS(\Omega)\mathbf{I}_b\Omega + \Omega^T\boldsymbol{\tau}, \tag{8.24}$$

which uner the control law (8.22) and the skew-symmetric property $S(u)u = u^TS(u) = 0$, simplifies to

$$\dot{\mathcal{V}} = -\Omega^T\Gamma\Omega \leq 0. \tag{8.25}$$

Showing the boundedness of all signals and asymptotic convergence of Ω to 0 as t goes to ∞. Using LaSalle's invariance principle, one can show that $\tilde{q}$ asymptotically converges to zero.

8.4 Trajectory Generation

With the position control objective satisfied, one seeks to move the VTOL UAV from an initial position $\mathbf{p}_0$ at time t_0, to a final desired position $\mathbf{p}_f$ at time t_f. This should not be attempted through instantaneously altering the position setpoint from $\mathbf{p}_0$ to $\mathbf{p}_f$, as the intermediary trajectory will be undefined, and the flight path of the UAV unknown. Instead a simple trajectory is defined, where, the position, velocity and acceleration of the drone will be specified for all instances of time between t_0 and t_f. The trajectory chosen, as a function of time, is as follows:

$$\mathbf{r}(t) = \begin{bmatrix} 1 \\ 1 \\ 1 \end{bmatrix} \left(a_0 + a_1 t + a_2 t^2 + a_3 t^3 + a_4 t^4 + a_5 t^5\right), \tag{8.26}$$

where, by choosing the boundary conditions

$$\begin{array}{ll} \mathbf{r}(t_0) = \mathbf{p}_0 & \mathbf{r}(t_f) = \mathbf{p}_f \\ \dot{\mathbf{r}}(t_0) = 0 & \dot{\mathbf{r}}(t_f) = 0 \\ \ddot{\mathbf{r}}(t_0) = 0 & \ddot{\mathbf{r}}(t_f) = 0, \end{array} \tag{8.27}$$

and defining

$$T = t_f - t_0,$$

becomes

$$\mathbf{r}(t) = \mathbf{p}_0 + (\mathbf{p}_f - \mathbf{p}_0)\left(10\left(\frac{t}{T}\right)^3 - 15\left(\frac{t}{T}\right)^4 + 6\left(\frac{t}{T}\right)^5\right), \tag{8.28}$$

with

$$\dot{\mathbf{r}}(t) = (\mathbf{p}_f - \mathbf{p}_0)\left(30\left(\frac{t}{T}\right)^2 - 60\left(\frac{t}{T}\right)^3 + 30\left(\frac{t}{T}\right)^4\right), \tag{8.29}$$

and

$$\ddot{\mathbf{r}}(t) = (\mathbf{p}_f - \mathbf{p}_0)\left(60\left(\frac{t}{T}\right) - 180\left(\frac{t}{T}\right)^2 + 120\left(\frac{t}{T}\right)^3\right). \tag{8.30}$$

From this, all translational flight path parameters are defined for all instances of time between t_0 and t_f. Further, by choosing a sufficiently large value of T, one can ensure $\|\ddot{\mathbf{r}}(t)\| = \delta_r$ is sufficiently small to not negatively impact the performance of the controller (8.4). An example of a trajectory with $\mathbf{p}_0 = [0\ 0\ 0]^T$, $\mathbf{p}_f = [1\ 2\ 3]^T$, $t_0 = 0$ and $T = 10$ is shown in Fig.8.3

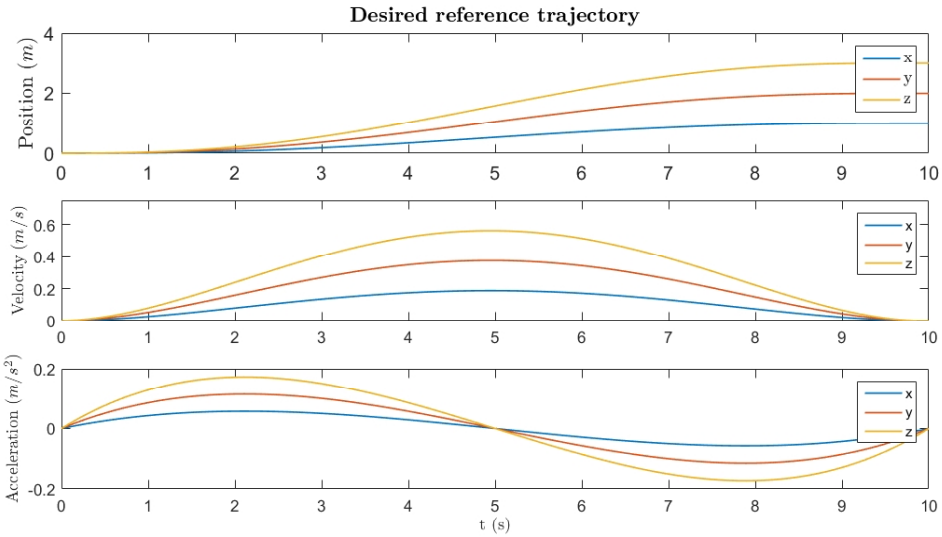

FIGURE 8.3: Generated desired reference trajectory

8.5 Results

8.5.1 Simulation Results

With control specified from the position error to the desired input torques, it is possible to convert these torques to rotor speed through eq. 4.5 which will control the position and orientation of the VTOL UAV. Simulations for a position hold command using this controller are preformed with the initial conditions $\tilde{\mathbf{p}}_0 = [0.1\ -0.2\ 0.2]^T$, $\tilde{\mathbf{v}}_0 = [1\ -0.5\ 0.25]^T$, $\tilde{Q}_0 = [0.98\ 0.04\ 0.13\ 0.05]^T$, $\tilde{\Omega}_0 = [0\ 0\ 0]^T$. These initial conditions are chosen as they represent conditions that are similar to the implementation of a position hold command.

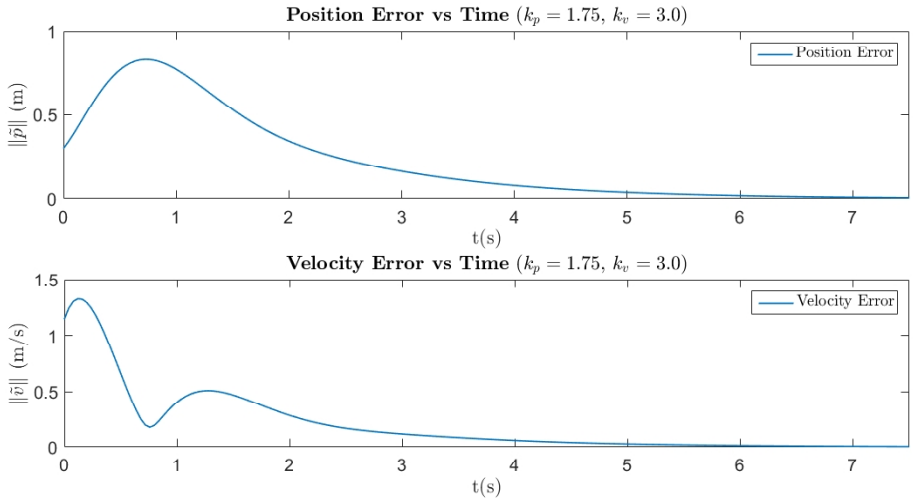

FIGURE 8.4: Simulated position and velocity errors

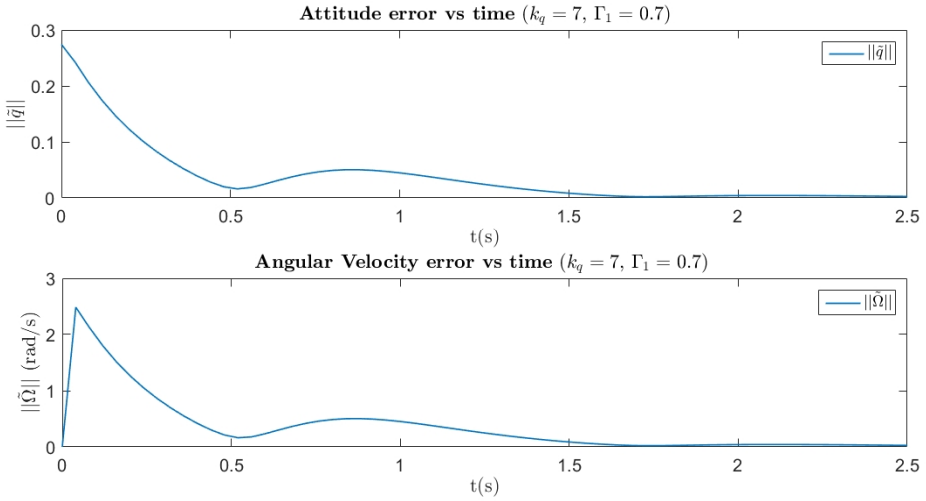

FIGURE 8.5: Simulated orientation and angular velocity errors

8.5.2 Implementation Results

Implementation results for a position hold command, as well as an automatic take-off command and a further trajectory tracking objective have been carried out. For the position hold command, the quadrotor is first held steady in manual flight, control is then taken over by the position control system, and the current position is maintained. Automatic take-off utilizes the trajectory outlined in eq. 8.28, where, the x and y components of the reference trajectory are maintained constant while the final z component is specified as 1.5m. In the final trajectory tracking experiment, the drone is specified to fly to a number of points on the circle centered at $x_c = 1.5, y_c = 2.5$ or radius $r = 0.75$. In this final trajectory tracking experiment, it is shown that the practical controller is capable of following a desired reference with an average position error of $27cm$ and a average velocity error of $6cm/s$. The position error is relatively large due to the small gain k_p chosen, this gain is chosen small to ensure minimal oscillations occur during implementation, as large oscillations could lead to damaging the drone.

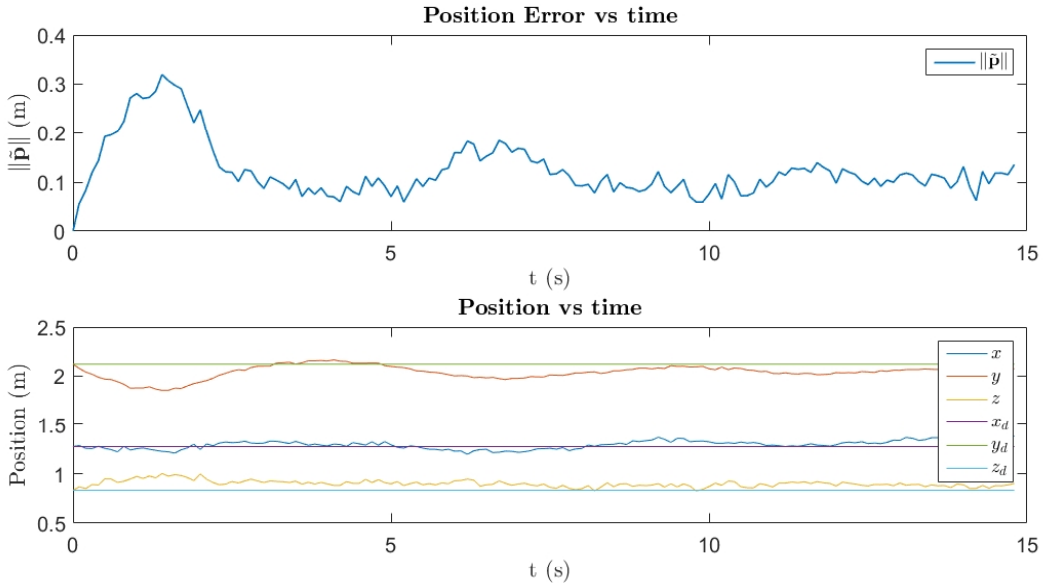

FIGURE 8.6: Position hold implementation results, Position

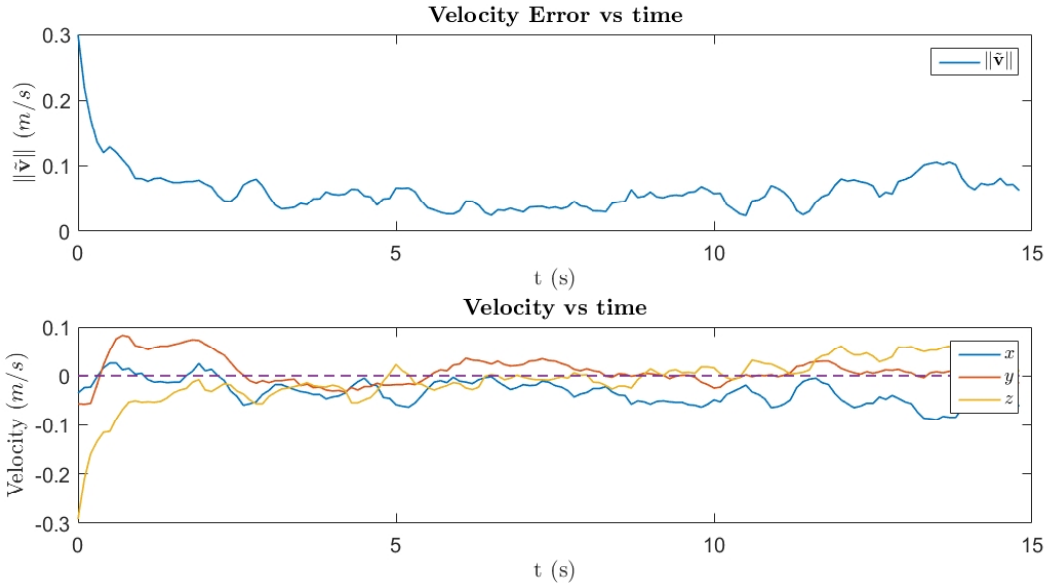

FIGURE 8.7: Position hold implementation results, Velocity

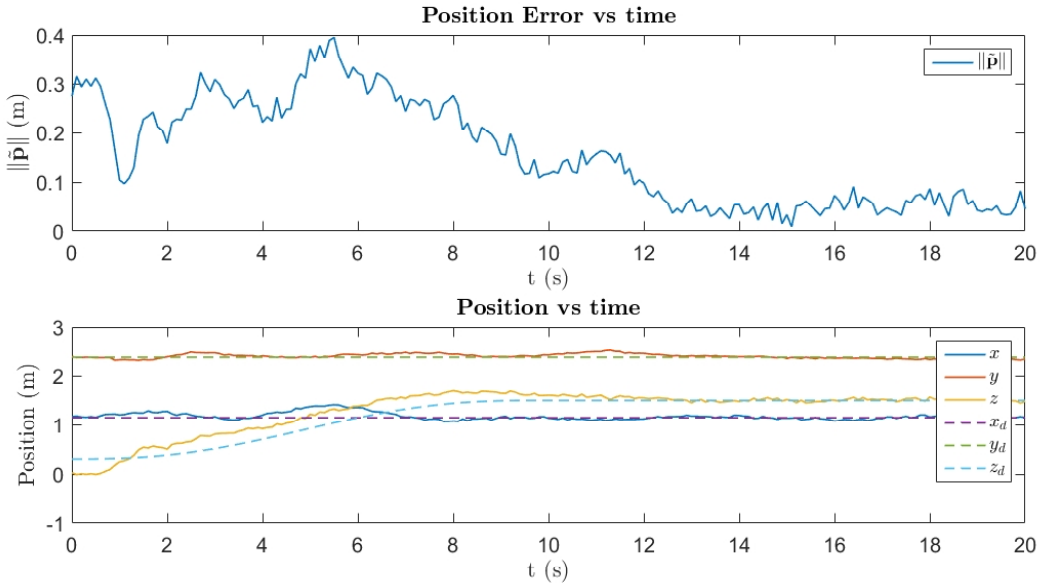

FIGURE 8.8: Automatic take-off implementation results, Position

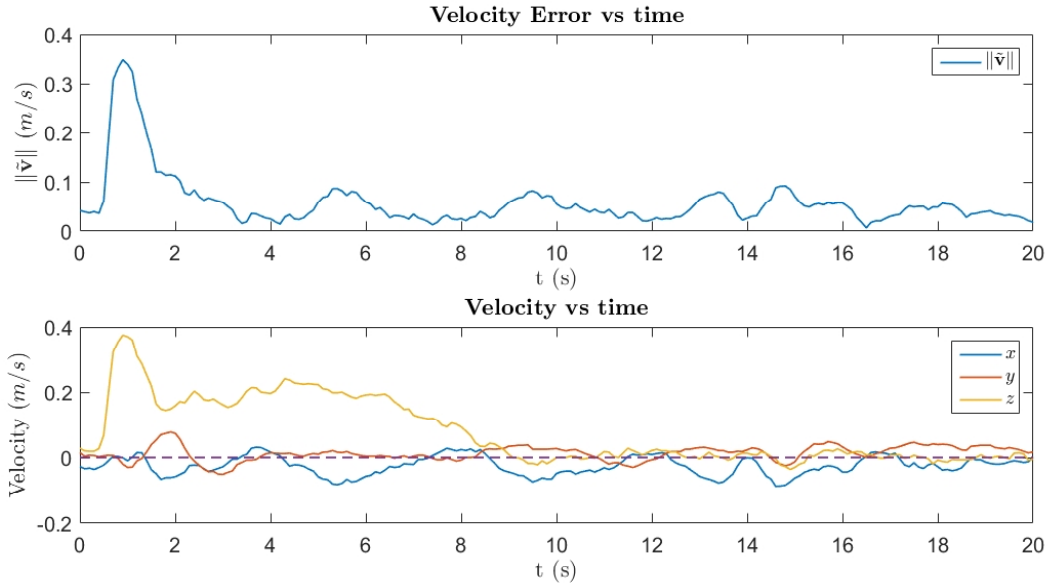

FIGURE 8.9: Automatic take-off implementation results, Velocity

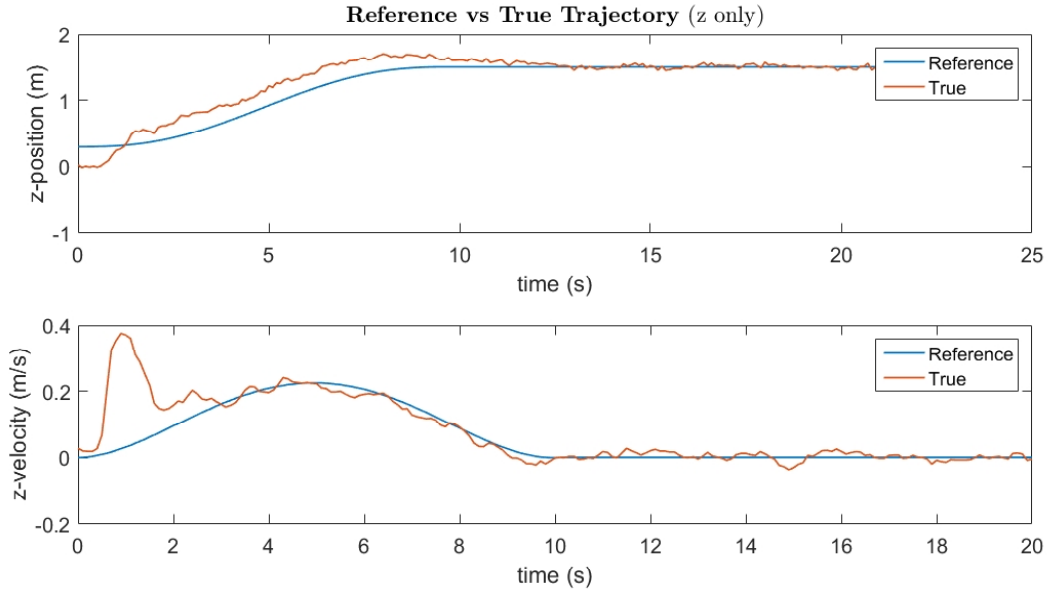

FIGURE 8.10: Automatic take-off implementation results, z-axis trajectory

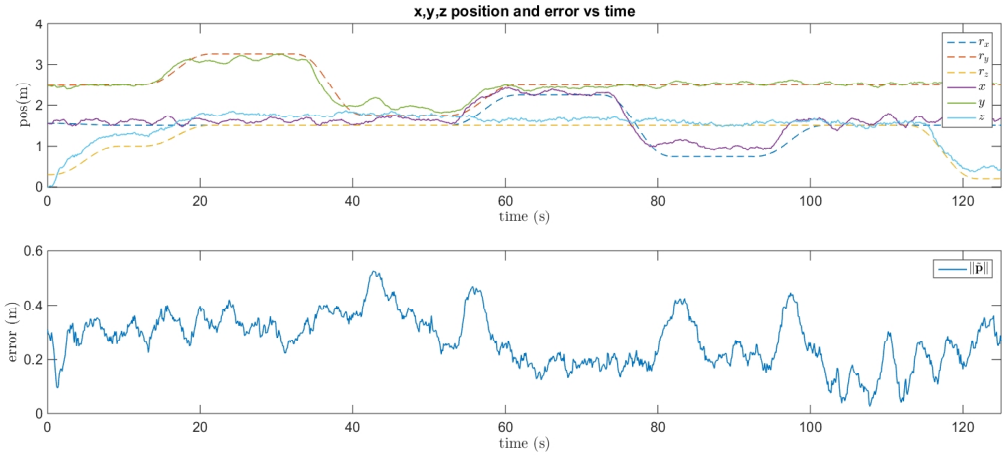

FIGURE 8.11: Trajectory tracking results, position

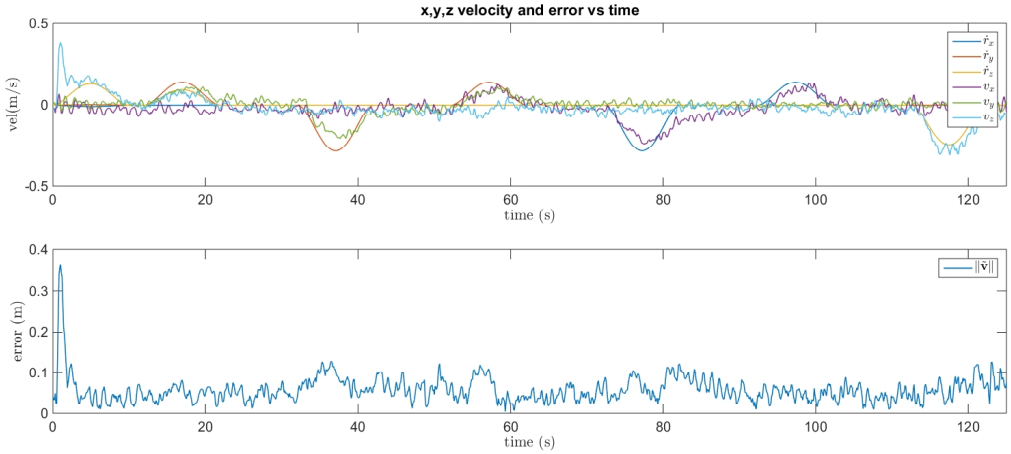

FIGURE 8.12: Trajectory tracking results, velocity

Chapter 9

Position Control Using Backstepping Approach

Due to the assumptions made in Chapter 8, it is not guaranteed that the simplified controller will stabilize the position of the VTOL UAV from any initial conditions. The method in this section is similar to that of the simplified approach as it can be seen as two separate parts; first a desired acceleration designed to drive the UAV to the desired position is determined, from which the thrust and desired attitude are extracted. Thereafter, the control torque is designed for the rotational dynamics, using the extracted orientation. The main difference is that the term $\tilde{\boldsymbol{\mu}}$ is no longer ignored and instead accounted for in the design of the control torques. This approach leads to global stability results which are much stronger than the local stability achieved in the simplified approach presented earlier.

9.1 Mathematical Preliminaries

Bounded Function

Before proceeding with the control design, define the following bounded vector function, for any vector $\mathbf{u} = [u_1 \; u_2 \; u_3]^T \in \mathbb{R}^3$:

$$h(\mathbf{u}) := \frac{1}{\sqrt{3}} \begin{bmatrix} \tanh(u_1) \\ \tanh(u_2) \\ \tanh(u_3) \end{bmatrix}, \tag{9.1}$$

which has the partial derivative

$$\phi_h := \frac{\partial}{\partial \mathbf{u}} h(\mathbf{u}) = \frac{1}{\sqrt{3}} \begin{bmatrix} \operatorname{sech}^2(u_1) & 0 & 0 \\ 0 & \operatorname{sech}^2(u_2) & 0 \\ 0 & 0 & \operatorname{sech}^2(u_3) \end{bmatrix}. \tag{9.2}$$

Let us also define the following function:

$$\begin{aligned} f_{\phi_h}(\mathbf{u}, \mathbf{v}) &:= \frac{\partial}{\partial \mathbf{u}} \phi_h(\mathbf{u}) \mathbf{v} \\ &= \frac{1}{\sqrt{3}} \begin{bmatrix} -2\mathrm{t}_h(u_1)\mathrm{s}_h^2(u_1)v_1 & 0 & 0 \\ 0 & -2\mathrm{t}_h(u_2)\mathrm{s}_h^2(u_2)v_2 & 0 \\ 0 & 0 & -2\mathrm{t}_h(u_3)\mathrm{s}_h^2(u_3)v_3 \end{bmatrix}, \end{aligned} \tag{9.3}$$

where t_h and s_h represent the $\tanh$ and sech functions respectively. Notably, we see that the eigenvalues of $\phi_h(\mathbf{u})$ are the entries of the matrix $\phi_h(\mathbf{u})$ as the function $\text{sech}^2(u_i)$ is bounded from above and below, *i.e.* $0 < \text{sech}(u_i) < 1$ the norm of the matrix $\|\phi_h(\mathbf{u})\|_F$ is bounded by

$$0 < \|\phi_h(\mathbf{u})\|_F < 1, \ \forall \mathbf{u}. \tag{9.4}$$

Attitude Error Dynamics

The quaternion dynamics can be written as

$$\dot{Q} = \frac{1}{2}\begin{bmatrix} -q^T \\ q_o\mathbf{I}_{3\times 3} + S(q) \end{bmatrix}\Omega = \frac{1}{2}A_q\Omega,$$

where $A^TA = \mathbf{I}_{3\times 3}$. This relationship is used with the desired attitude extraction map eq. 8.13, to produce the desired angular velocity

$$\Omega_d = 2A_q^T\frac{d}{dt}\begin{bmatrix} f_{q_o}(\boldsymbol{\mu}_d) \\ f_q(\boldsymbol{\mu}_d) \end{bmatrix}, \tag{9.5}$$

which can be re-written as

$$\Omega_d = M(\boldsymbol{\mu}_d)\dot{\boldsymbol{\mu}}_d, \tag{9.6}$$

where

$$M(\boldsymbol{\mu}_d) = \frac{1}{\|\boldsymbol{\mu}_d - g\hat{\mathbf{e}}_3\|^2 c_1}\begin{bmatrix} -\mu_{d_1}\mu_{d_2} & -\mu_{d_2}^2 + \|\boldsymbol{\mu}_d - g\hat{\mathbf{e}}_3\|c_1 & \mu_{d_2}c_1 \\ \mu_{d_1}^2 - \|\boldsymbol{\mu}_d - g\hat{\mathbf{e}}_3\|c_1 & \mu_{d_1}\mu_{d_2} & -\mu_{d_1}c_1 \\ \mu_{d_2}\|\boldsymbol{\mu}_d - g\hat{\mathbf{e}}_3\| & -\mu_{d_1}\|\boldsymbol{\mu}_d - g\hat{\mathbf{e}}_3\| & 0 \end{bmatrix}, \tag{9.7}$$

with $c_1 = \|\boldsymbol{\mu}_d - g\hat{\mathbf{e}}_3\| + g - \mu_{d_3}$. The attitude error dynamics are given by

$$\dot{\tilde{Q}} = \frac{1}{2}\begin{bmatrix} \tilde{q}^T(\Omega_d - \Omega) \\ \tilde{q}_0(\Omega - \Omega_d) + S(\tilde{q})(\Omega_d - \Omega) \end{bmatrix}. \tag{9.8}$$

9.2 Controller Design

Let us define the following error signals:

$$\begin{aligned} \tilde{\mathbf{p}} &= \mathbf{p} - \mathbf{r}(t) \\ \tilde{\mathbf{v}} &= \mathbf{v} - \dot{\mathbf{r}}(t) \\ \tilde{\boldsymbol{\mu}} &= \boldsymbol{\mu} - \boldsymbol{\mu}_d \\ \tilde{\mathbf{R}} &= \mathbf{R}\mathbf{R}_d^T \\ \tilde{\Omega} &= \Omega - \beta, \end{aligned} \tag{9.9}$$

where $\mathbf{r}(t)$ is some arbitrary reference trajectory, satisfying $\mathbf{r}(t) \in \mathbb{C}^4$ and $\|\ddot{r}(t)\| \leqslant \delta_r$, $\tilde{\boldsymbol{\mu}}$ is the acceleration error with $\boldsymbol{\mu} = g\hat{\mathbf{e}}_3 - \frac{\mathcal{T}}{m}\mathbf{R}^T\hat{\mathbf{e}}_3$ and $\boldsymbol{\mu}_d = g\hat{\mathbf{e}}_3 - \frac{\mathcal{T}}{m}\mathbf{R}_d^T\hat{\mathbf{e}}_3$, and β is a design variable

to be determined later. The full error dynamics can be written as

$$\begin{aligned}
\dot{\tilde{\mathbf{p}}} &= \tilde{\mathbf{v}} \\
\dot{\tilde{\mathbf{v}}} &= \boldsymbol{\mu}_d + \tilde{\boldsymbol{\mu}} - \ddot{\mathbf{r}}(t) \\
\dot{\tilde{Q}} &= \frac{1}{2}\begin{bmatrix} \tilde{q}^T(\Omega_d - \tilde{\Omega} - \beta) \\ \tilde{q}_0(\beta + \tilde{\Omega} - \Omega_d) + S(\tilde{q})(\beta + \tilde{\Omega} + \Omega_d) \end{bmatrix} \\
\mathbf{I}_b\dot{\tilde{\Omega}} &= -S(\Omega)\mathbf{I}_b\Omega - \mathbf{I}_b\dot{\beta} + \boldsymbol{\tau}_a.
\end{aligned} \tag{9.10}$$

Further, the acceleration error can be redefined as a function of the quaternion error $\tilde{q}$ and the total system thrust $u_t := \frac{\mathcal{T}}{m}$ through

$$\begin{aligned}
\tilde{\boldsymbol{\mu}} &= u_t\left(\mathbf{R}_d^T - \mathbf{R}^T\right)\hat{\mathbf{e}}_3 \\
&= u_t\mathbf{R}^T\left(\tilde{\mathbf{R}} - \mathbf{I}_{3\times 3}\right)\hat{\mathbf{e}}_3.
\end{aligned} \tag{9.11}$$

Using the Rodrigues formula (eq. 3.8), one gets

$$\begin{aligned}
\tilde{\boldsymbol{\mu}} &= u_t\mathbf{R}^T\left(2S(\tilde{q})^2 - 2\tilde{q}_0S(\tilde{q})\right)\hat{\mathbf{e}}_3 \\
&= 2u_t\mathbf{R}^TS(\tilde{q})\left(S(\tilde{q}) - \tilde{q}_0\mathbf{I}_{3\times 3}\right)\hat{\mathbf{e}}_3,
\end{aligned} \tag{9.12}$$

from which, we define

$$\begin{aligned}
\bar{q} &= -\left(S(\tilde{q}) - \tilde{q}_0\mathbf{I}_{3\times 3}\right)\hat{\mathbf{e}}_3 \\
&= S(\hat{\mathbf{e}}_3)\tilde{q} + \tilde{q}_0\hat{\mathbf{e}}_3,
\end{aligned} \tag{9.13}$$

giving

$$\begin{aligned}
\tilde{\boldsymbol{\mu}} &= -2u_t\mathbf{R}^TS(\tilde{q})\bar{q} \\
&= -2u_t\mathbf{R}^TS(\bar{q})^T\tilde{q}.
\end{aligned} \tag{9.14}$$

Choosing the following positive definite function:

$$\mathcal{V}_1 = \frac{k_p}{\sqrt{3}}\left[1\ 1\ 1\right]\log(\cosh(\tilde{\mathbf{p}})) + \frac{1}{2}\tilde{\mathbf{v}}^T\tilde{\mathbf{v}} + 2k_q(1 - \tilde{q}_0), \tag{9.15}$$

in view of (9.9), one obtains the following time-derivative:

$$\dot{\mathcal{V}}_1 = k_ph(\tilde{\mathbf{p}})\tilde{\mathbf{v}} + \tilde{\mathbf{v}}^T(\boldsymbol{\mu}_d + \tilde{\boldsymbol{\mu}} - \ddot{\mathbf{r}}(t)) - k_q\tilde{q}^T(\Omega_d - \tilde{\Omega} - \beta). \tag{9.16}$$

Applying the control

$$\boldsymbol{\mu}_d = -k_ph(\tilde{\mathbf{p}}) - k_vh(\tilde{\mathbf{v}}) + \ddot{\mathbf{r}}(t), \tag{9.17}$$

along with the relationships (9.6) and (9.14), equation (9.16) can be written as

$$\dot{\mathcal{V}}_1 = -k_v\tilde{\mathbf{v}}^Th(\tilde{\mathbf{v}}) - k_q\tilde{q}^T\left(M(\boldsymbol{\mu}_d)\dot{\boldsymbol{\mu}}_d + \tfrac{2u_t}{k_q}S(\bar{q})\mathbf{R}\tilde{\mathbf{v}} - \beta - \tilde{\Omega}\right), \tag{9.18}$$

where $\dot{\boldsymbol{\mu}}_d$ is given by

$$\dot{\boldsymbol{\mu}}_d = -k_p\phi_h(\tilde{\mathbf{p}})\tilde{\mathbf{v}} - k_v\phi_h(\tilde{\mathbf{v}})\dot{\tilde{\mathbf{v}}} + \mathbf{r}^{(3)}(t),$$

with

$$\dot{\tilde{\mathbf{v}}} = \tilde{\boldsymbol{\mu}} - k_p h(\tilde{\mathbf{p}}) - k_v h(\tilde{\mathbf{v}}),$$

the expression of $\dot{\mathcal{V}}_1$ becomes

$$\begin{aligned}\dot{\mathcal{V}}_1 = &- k_v \tilde{\mathbf{v}}^T h(\tilde{\mathbf{v}}) - k_q \tilde{q}^T \Big\{ M(\boldsymbol{\mu}_d) \Big[\mathbf{r}^{(3)}(t) - k_p \phi_h(\tilde{\mathbf{p}}) \tilde{\mathbf{v}} - k_v \phi_h(\tilde{\mathbf{v}}) \left(\tilde{\boldsymbol{\mu}} - k_p h(\tilde{\mathbf{p}}) - k_v h(\tilde{\mathbf{v}}) \right) \Big] \\ &+ \tfrac{2u_t}{k_q} S(\overline{q}) \mathbf{R} \tilde{\mathbf{v}} - \beta - \tilde{\Omega} \Big\}.\end{aligned} \tag{9.19}$$

Defining the auxiliary variable β as

$$\beta = M(\boldsymbol{\mu}_d) \Big[\mathbf{r}^{(3)}(t) - k_p \phi_h(\tilde{\mathbf{p}}) \tilde{\mathbf{v}} + k_v k_p \phi_h(\tilde{\mathbf{v}}) h(\tilde{\mathbf{p}}) \Big] + 2u_t S(\overline{q}) \mathbf{R} \tilde{\mathbf{v}} - \Gamma_q \tilde{q}, \tag{9.20}$$

gives

$$\begin{aligned}\dot{\mathcal{V}}_1 = &- k_v \tilde{\mathbf{v}}^T h(\tilde{\mathbf{v}}) - k_q \tilde{q}^T \Gamma_q \tilde{q} - 2u_t k_q k_v \tilde{q}^T M(\boldsymbol{\mu}_d) \phi_h(\tilde{\mathbf{v}}) S(\overline{q}) \mathbf{R} \tilde{q} \\ &- k_q k_v^2 \tilde{q}^T M(\boldsymbol{\mu}_d) \phi_h(\tilde{\mathbf{v}}) h(\tilde{\mathbf{v}}) + k_q \tilde{q}^T \tilde{\Omega}.\end{aligned} \tag{9.21}$$

From the definition of $\boldsymbol{\mu}_d$ and the fact that each element of $\boldsymbol{\mu}_d$ can be bounded by

$$\begin{aligned}|\mu_{d_i}| \leqslant \overline{\mu}_{d_i} = \frac{k_p + k_v}{\sqrt{3}} + \delta_r \\ i = \{1, 2, 3\},\end{aligned} \tag{9.22}$$

we see that u_t can be bounded from above and below as

$$\begin{aligned}0 < \underline{u}_t \leqslant u_t \leqslant \overline{u}_t < \infty \\ \overline{u}_t = g + \delta_r + k_p + k_v \\ \underline{u}_t = g - \delta_r - \tfrac{k_p + k_v}{\sqrt{3}}.\end{aligned}$$

The norm of $M(\boldsymbol{\mu}_d)$ is bounded by

$$\| M(\boldsymbol{\mu}_d) \|_F \leqslant \frac{\sqrt{2}}{\underline{u}_t},$$

as shown in [51]. Furthermore, one has

$$\begin{aligned}\| \mathbf{R} \| &= 1 \\ \| S(\overline{q}) \| &\leqslant 1 \\ \| \phi_h(\cdot) \| &\leqslant 1.\end{aligned}$$

The terms which are not compensated with the auxiliary variable β can be bounded, by using the above bounds and Young's inequality as follows:

$$\begin{aligned} 2u_t k_q k_v \tilde{q}^T M(\boldsymbol{\mu}_d)\phi_h(\tilde{\mathbf{v}})S(\overline{q})\mathbf{R}\tilde{q} &\leqslant \frac{2\sqrt{2}\overline{u}_t k_q k_v}{\underline{u}_t}\tilde{q}^T\tilde{q} \\ k_q k_v^2 \tilde{q}^T M(\boldsymbol{\mu}_d)\phi_h(\tilde{\mathbf{v}})h(\tilde{\mathbf{v}}) &\leqslant \frac{\sqrt{2}k_q k_v^2}{\underline{u}_t}\tilde{q}^T h(\tilde{\mathbf{v}}) \leqslant \frac{\sqrt{2}k_q k_v^2}{\underline{u}_t}\left(\frac{1}{4\epsilon_1}\tilde{q}^T\tilde{q} + \epsilon_1 \tilde{\mathbf{v}}^T h(\tilde{\mathbf{v}})\right), \end{aligned} \tag{9.23}$$

where ϵ_1 is an arbitrary positive constant, using the previous inequalities, one gets

$$\dot{\mathcal{V}}_1 \leqslant -\tilde{\mathbf{v}}^T\left(k_v - \frac{\sqrt{2}k_q k_v^2\epsilon_1}{\underline{u}_t}\right)h(\tilde{\mathbf{v}}) - k_q\tilde{q}^T\left(\Gamma_q - \frac{2\sqrt{2}\overline{u}_t k_v}{\underline{u}_t} - \frac{k_v^2}{2\sqrt{2}\underline{u}_t\epsilon_1}\right)\tilde{q} + k_q\tilde{q}^T\tilde{\Omega}. \tag{9.24}$$

The final Lyapunov function candidate is given by

$$\mathcal{V}_2 = \mathcal{V}_1 + \tilde{\Omega}^T\mathbf{I}_b\tilde{\Omega}, \tag{9.25}$$

which under the following control law

$$\boldsymbol{\tau}_a = S(\Omega)\mathbf{I}_b\Omega + \mathbf{I}_b\dot{\beta} - k_q\tilde{q} - \Gamma_\Omega\tilde{\Omega}, \tag{9.26}$$

leads to

$$\dot{\mathcal{V}}_2 \leqslant -\tilde{\mathbf{v}}^T\left(k_v - \frac{\sqrt{2}k_q k_v^2\epsilon_1}{\underline{u}_t}\right)h(\tilde{\mathbf{v}}) - \tilde{q}^T\left(\Gamma_q - \frac{2\sqrt{2}\overline{u}_t k_v}{\underline{u}_t} - \frac{k_v^2}{2\sqrt{2}\underline{u}_t\epsilon_1}\right)\tilde{q} - \tilde{\Omega}^T\Gamma_\Omega\tilde{\Omega}. \tag{9.27}$$

By choosing

$$\begin{aligned} k_v &> \frac{\underline{u}_t}{\sqrt{2}k_q\epsilon_1} \\ \Gamma_q &> \frac{2\sqrt{2}\overline{u}_t k_v}{\underline{u}_t} + \frac{k_v^2}{2\sqrt{2}\underline{u}_t\epsilon_1}, \end{aligned} \tag{9.28}$$

one can ensure.

$$\dot{\mathcal{V}}_2 \leqslant 0, \tag{9.29}$$

As such, the states $\left(\tilde{\mathbf{p}},\ \tilde{\mathbf{v}},\ \tilde{Q},\ \tilde{\Omega}\right)$ remain bounded for all $t > 0$. Further, the states $\left(\tilde{\mathbf{v}},\ \tilde{q},\ \tilde{\Omega}\right) \to (\mathbf{0},\ \mathbf{0},\ \mathbf{0})$ as $t \to \infty$. Invoking LaSalle invariance, in view of the system (9.9) with the virtual control (9.17), one can conclude that

$$\dot{\tilde{\mathbf{v}}} = 0 = -k_p h(\tilde{\mathbf{p}}) - k_v h(\tilde{\mathbf{v}}) - 2u_t\mathbf{R}^T S(\overline{q})^T\tilde{q}, \tag{9.30}$$

which, with the above

$$-k_p h(\tilde{\mathbf{p}}) = 0, \tag{9.31}$$

or, equivalently

$$\tilde{\mathbf{p}} = 0. \tag{9.32}$$

Satisfying the position control objective and showing global asymptotic stability of the equilibrium point $[\tilde{\mathbf{p}},\ \tilde{\mathbf{v}},\ \tilde{q},\ \tilde{\Omega}] = [\mathbf{0},\ \mathbf{0},\ \mathbf{0},\ \mathbf{0}]$. The main difference between this controller and the simplified controller, is that the assumption $\tilde{\boldsymbol{\mu}} \approx 0$ is no longer required, and as such this controller will be capable of maintaining stability even under large accelerations.

9.3 Results

9.3.1 Simulation Results

Simulations are performed for a trajectory tracking goal with the desired trajectory specified as

$$\mathbf{r}(t) = \begin{bmatrix} 4\cos(\frac{\pi t}{30}) \\ 3\sin(\frac{\pi t}{30}) \\ t/4 \end{bmatrix},$$

satisfying,

$$\|\ddot{\mathbf{r}}(t)\| \leqslant \delta_r = \sqrt{(\tfrac{\pi}{225})^2 + (\tfrac{\pi}{300})^2} \approx 0.055.$$

which ensures that the necessary bound on $\boldsymbol{\mu}_d$ is easily met, as well as $\mathbf{r}(t) \in \mathbb{C}^4$. The control parameters chosen are $k_p = 3.25$, $k_v = 4.75$, $\Gamma_q = \text{diag}(20, 20, 20)$, $k_q = 5$, and $\Gamma_\Omega = \text{diag}(1.5, 1.5, 1.5)$ with initial conditions $\tilde{\mathbf{p}}_0 = [-3\ 0\ 1]^T$, $\tilde{\mathbf{v}}_0 = [0\ 0\ 0]^T$, $Q_0 = [0\ 1\ 0\ 0]^T$, and $\Omega_0 = [0\ 0\ 0]^T$. It can be seen from these simulations that, that even from large initial conditions, the controller is able to achieve its objective.

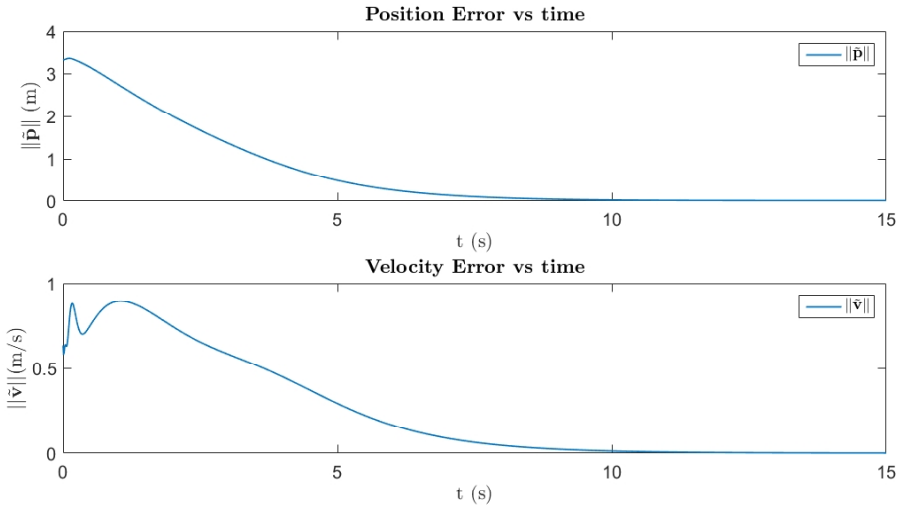

FIGURE 9.1: position and velocity errors vs time, backstepping controller

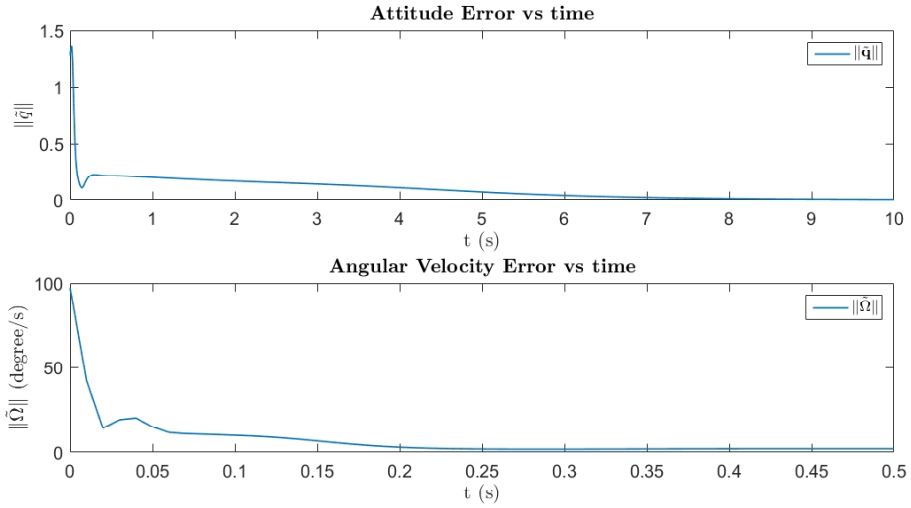

FIGURE 9.2: Attitude error and angular velocity vs time, backstepping controller

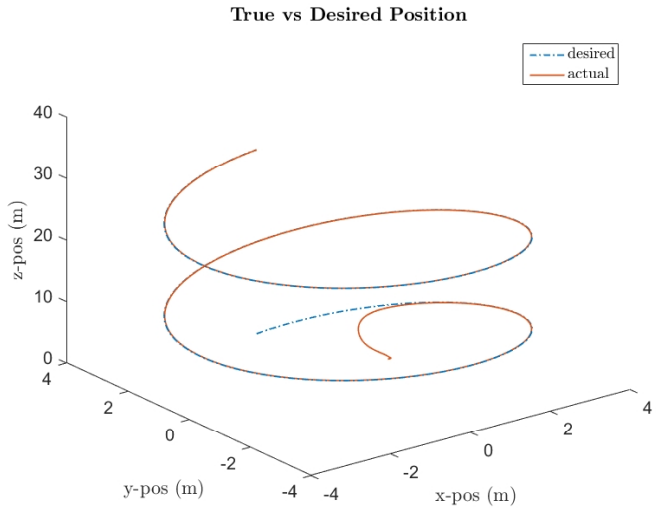

FIGURE 9.3: Desired vs true trajectory, backstepping controller

Chapter 10

Conclusion

In this thesis a complete UWB based system, for position measurement was designed and implemented. A position tracking control scheme, relying on IMU and UWB measurements has been successfully implemented on a quadrotor UAV.

The attitude estimation technique, used in this work, was the conditioned nonlinear complementary filter, as this estimator is computationally efficient for implementation. A method to compensate for the magnetic field induced by the current drawn from the the onboard battery was proposed to improve the performance of the estimation scheme.

A Kalman Filter based position and velocity estimation scheme was implemented using UWB measurements fused with accelerometer data.

As a future work, it would be interesting to design a fully integrated estimation scheem taking the IMU and UWB measurement and providing filtered estimates of the attitude, position and linear velocity. Another interesting work, would be the design of path following strategies with obstacle avoidance techniques, to pave the oath towards fully autonomous navigation systems for quadrotor UAVs

Bibliography

[1] M. W. Mueller and R. D'Andrea, "Critical subsystem failure mitigation in an indoor uav testbed.", in *IROS*, 2012, pp. 780–785.

[2] M. W. Mueller and R. D'Andrea, "Relaxed hover solutions for multicopters: Application to algorithmic redundancy and novel vehicles", *The International Journal of Robotics Research*, vol. 35, no. 8, pp. 873–889, 2016.

[3] D. Bamburry, "Drones: Designed for product delivery", *Design Management Review*, vol. 26, no. 1, pp. 40–48, 2015.

[4] R. L. Finn and D. Wright, "Unmanned aircraft systems: Surveillance, ethics and privacy in civil applications", *Computer Law & Security Review*, vol. 28, no. 2, pp. 184–194, 2012.

[5] K. Munson, *Helicopters and other rotorcraft since 1907*. Macmillan, 1969.

[6] R. Brown, "Planes that go straight up; open new fields for aviation", *Popular Science Monthly*, vol. 126, no. 3, pp. 13–15, 1935.

[7] G. Hoffmann, D. G. Rajnarayan, S. L. Waslander, D. Dostal, J. S. Jang, and C. J. Tomlin, "The stanford testbed of autonomous rotorcraft for multi agent control (starmac)", in *Digital Avionics Systems Conference, 2004. DASC 04. The 23rd*, IEEE, vol. 2, 2004, 12–E.

[8] J. P. How, B. BEHIHKE, A. Frank, D. Dale, and J. Vian, "Real-time indoor autonomous vehicle test environment", *IEEE control systems*, vol. 28, no. 2, pp. 51–64, 2008.

[9] S. Lupashin, M. Hehn, M. W. Mueller, A. P. Schoellig, M. Sherback, and R. D'Andrea, "A platform for aerial robotics research and demonstration: The flying machine arena", *Mechatronics*, vol. 24, no. 1, pp. 41–54, 2014.

[10] A. Abdessameud and A. Tayebi, "Global trajectory tracking control of vtol-uavs without linear velocity measurements", *Automatica*, vol. 46, no. 6, pp. 1053–1059, 2010.

[11] G. Wahba, "A least squares estimate of satellite attitude", *SIAM review*, vol. 7, no. 3, pp. 409–409, 1965.

[12] M. D. Shuster and S. D. Oh, "Three-axis attitude determination from vector observations", *Journal of Guidance, Control, and Dynamics*, vol. 4, no. 1, pp. 70–77, 1981.

[13] F. L. Markley, "Attitude determination using vector observations and the singular value decomposition", *Journal of the Astronautical Sciences*, vol. 36, no. 3, pp. 245–258, 1988.

[14] H. D. Black, "A passive system for determining the attitude of a satellite", *AIAA journal*, vol. 2, no. 7, pp. 1350–1351, 1964.

[15] R. E. Kalman, "A new approach to linear filtering and prediction problems", *Journal of basic Engineering*, vol. 82, no. 1, pp. 35–45, 1960.

[16] F. L. Markley, "Attitude error representations for kalman filtering", *Journal of guidance, control, and dynamics*, vol. 26, no. 2, pp. 311–317, 2003.

[17] I. Bar-Itzhack and Y. Oshman, "Attitude determination from vector observations: Quaternion estimation", *IEEE Transactions on Aerospace and Electronic Systems*, no. 1, pp. 128–136, 1985.

[18] M.-D. Hua, G. Ducard, T. Hamel, R. Mahony, and K. Rudin, "Implementation of a nonlinear attitude estimator for aerial robotic vehicles", *IEEE Transactions on Control Systems Technology*, vol. 22, no. 1, pp. 201–213, 2014.

[19] P. Martin and E. Salaün, "Design and implementation of a low-cost observer-based attitude and heading reference system", *Control Engineering Practice*, vol. 18, no. 7, pp. 712–722, 2010.

[20] R. Mahony, T. Hamel, J. Trumpf, and C. Lageman, "Nonlinear attitude observers on so (3) for complementary and compatible measurements: A theoretical study", in *Decision and Control, 2009 held jointly with the 2009 28th Chinese Control Conference. CDC/CCC 2009. Proceedings of the 48th IEEE Conference on*, IEEE, 2009, pp. 6407–6412.

[21] R. Mahony, T. Hamel, and J.-M. Pflimlin, "Nonlinear complementary filters on the special orthogonal group", *IEEE Transactions on automatic control*, vol. 53, no. 5, pp. 1203–1218, 2008.

[22] M.-D. Hua, "Attitude estimation for accelerated vehicles using gps/ins measurements", *Control Engineering Practice*, vol. 18, no. 7, pp. 723–732, 2010.

[23] A. Roberts and A. Tayebi, "On the attitude estimation of accelerating rigid-bodies using gps and imu measurements", in *Decision and Control and European Control Conference (CDC-ECC), 2011 50th IEEE Conference on*, IEEE, 2011, pp. 8088–8093.

[24] C. C. Foster and G. H. Elkaim, "Extension of a two-step calibration methodology to include nonorthogonal sensor axes", *IEEE Transactions on Aerospace and Electronic Systems*, vol. 44, no. 3, 2008.

[25] M.-D. Hua, K. Rudin, G. Ducard, T. Hamel, and R. Mahony, "Nonlinear attitude estimation with measurement decoupling and anti-windup gyro-bias compensation", *IFAC Proceedings Volumes*, vol. 44, no. 1, pp. 2972–2978, 2011.

[26] J.-Y. Wen and K. Kreutz-Delgado, "The attitude control problem", *IEEE Transactions on Automatic control*, vol. 36, no. 10, pp. 1148–1162, 1991.

[27] N. A. Chaturvedi, A. K. Sanyal, and N. H. McClamroch, "Rigid-body attitude control", *IEEE Control Systems*, vol. 31, no. 3, pp. 30–51, 2011.

[28] S. Bouabdallah, A. Noth, and R. Siegwart, "Pid vs lq control techniques applied to an indoor micro quadrotor", in *Intelligent Robots and Systems, 2004.(IROS 2004). Proceedings. 2004 IEEE/RSJ International Conference on*, IEEE, vol. 3, 2004, pp. 2451–2456.

[29] J. Li and Y. Li, "Dynamic analysis and pid control for a quadrotor", in *Mechatronics and Automation (ICMA), 2011 International Conference on*, IEEE, 2011, pp. 573–578.

[30] E. Reyes-Valeria, R. Enriquez-Caldera, S. Camacho-Lara, and J. Guichard, "Lqr control for a quadrotor using unit quaternions: Modeling and simulation", in *Electronics, Communications and Computing (CONIELECOMP), 2013 International Conference on*, IEEE, 2013, pp. 172–178.

[31] M. Faessler, F. Fontana, C. Forster, E. Mueggler, M. Pizzoli, and D. Scaramuzza, "Autonomous, vision-based flight and live dense 3d mapping with a quadrotor micro aerial vehicle", *Journal of Field Robotics*, vol. 33, no. 4, pp. 431–450, 2016.

[32] H. Voos, "Nonlinear control of a quadrotor micro-uav using feedback-linearization", in *Mechatronics, 2009. ICM 2009. IEEE International Conference on*, IEEE, 2009, pp. 1–6.

[33] S. Bouabdallah and R. Siegwart, "Backstepping and sliding-mode techniques applied to an indoor micro quadrotor", in *Robotics and Automation, 2005. ICRA 2005. Proceedings of the 2005 IEEE International Conference on*, IEEE, 2005, pp. 2247–2252.

[34] T. Madani and A. Benallegue, "Backstepping control for a quadrotor helicopter", in *Intelligent Robots and Systems, 2006 IEEE/RSJ International Conference on*, IEEE, 2006, pp. 3255–3260.

[35] A. Tayebi and S. McGilvray, "Attitude stabilization of a vtol quadrotor aircraft", *IEEE Transactions on control systems technology*, vol. 14, no. 3, pp. 562–571, 2006.

[36] K. Siwiak, "Ultra-wide band radio: Introducing a new technology", in *Vehicular Technology Conference, 2001. VTC 2001 Spring. IEEE VTS 53rd*, IEEE, vol. 2, 2001, pp. 1088–1093.

[37] S. Gezici, Z. Tian, G. B. Giannakis, H. Kobayashi, A. F. Molisch, H. V. Poor, and Z. Sahinoglu, "Localization via ultra-wideband radios: A look at positioning aspects for future sensor networks", *IEEE signal processing magazine*, vol. 22, no. 4, pp. 70–84, 2005.

[38] H. Soganci, S. Gezici, and H. V. Poor, "Accurate positioning in ultra-wideband systems", *IEEE Wireless Communications*, vol. 18, no. 2, 2011.

[39] A. Bensky, *Wireless positioning technologies and applications*. Artech House, 2016.

[40] J. Tiemann, F. Eckermann, and C. Wietfeld, "Atlas-an open-source tdoa-based ultra-wideband localization system", in *Indoor Positioning and Indoor Navigation (IPIN), 2016 International Conference on*, IEEE, 2016, pp. 1–6.

[41] S. Al-Jazzar and J. Caffery, "Ml and bayesian toa location estimators for nlos environments", in *Vehicular Technology Conference, 2002. Proceedings. VTC 2002-Fall. 2002 IEEE 56th*, IEEE, vol. 2, 2002, pp. 1178–1181.

[42] H. Wymeersch, J. Lien, and M. Z. Win, "Cooperative localization in wireless networks", *Proceedings of the IEEE*, vol. 97, no. 2, pp. 427–450, 2009.

[43] J. Yan, C. C. Tiberius, G. J. Janssen, P. J. Teunissen, and G. Bellusci, "Review of range-based positioning algorithms", *IEEE Aerospace and Electronic Systems Magazine*, vol. 28, no. 8, pp. 2–27, 2013.

[44] T. Dierks and S. Jagannathan, "Output feedback control of a quadrotor uav using neural networks", *IEEE transactions on neural networks*, vol. 21, no. 1, pp. 50–66, 2010.

[45] D. Lee, T. C. Burg, B. Xian, and D. M. Dawson, "Output feedback tracking control of an underactuated quad-rotor uav", in *American Control Conference, 2007. ACC'07*, IEEE, 2007, pp. 1775–1780.

[46] S. Bouabdallah and R. Siegwart, "Full control of a quadrotor", in *Intelligent robots and systems, 2007. IROS 2007. IEEE/RSJ international conference on*, Ieee, 2007, pp. 153–158.

[47] J.-J. Xiong and E.-H. Zheng, "Position and attitude tracking control for a quadrotor uav", *ISA transactions*, vol. 53, no. 3, pp. 725–731, 2014.

[48] M.-D. Hua, T. Hamel, P. Morin, and C. Samson, "A control approach for thrust-propelled underactuated vehicles and its application to vtol drones", *IEEE Transactions on Automatic Control*, vol. 54, no. 8, pp. 1837–1853, 2009.

[49] A. Roza and M. Maggiore, "A class of position controllers for underactuated vtol vehicles", *IEEE Transactions on Automatic Control*, vol. 59, no. 9, pp. 2580–2585, 2014.

[50] J. Tiemann, F. Schweikowski, and C. Wietfeld, "Design of an uwb indoor-positioning system for uav navigation in gnss-denied environments", in *Indoor Positioning and Indoor Navigation (IPIN), 2015 International Conference on*, IEEE, 2015, pp. 1–7.

[51] A. Roberts and A. Tayebi, "Adaptive position tracking of vtol uavs", *IEEE Transactions on Robotics*, vol. 27, no. 1, pp. 129–142, 2011.

[52] M. W. Mueller, M. Hamer, and R. D'Andrea, "Fusing ultra-wideband range measurements with accelerometers and rate gyroscopes for quadrocopter state estimation", in *Robotics and Automation (ICRA), 2015 IEEE International Conference on*, IEEE, 2015, pp. 1730–1736.

[53] M. D. Shuster, "A survey of attitude representations", *Navigation*, vol. 8, no. 9, pp. 439–517, 1993.

[54] B. W. McCormick, *Aerodynamics, aeronautics, and flight mechanics*. John Wiley, 1995.

[55] S. J. McGilvray, "Attitude stabilization of a quadrotor aircraft.", 2000.

[56] J. L. Crassidis, F. L. Markley, and Y. Cheng, "Survey of nonlinear attitude estimation methods", *Journal of guidance, control, and dynamics*, vol. 30, no. 1, pp. 12–28, 2007.

[57] R. Mahony, T. Hamel, and J.-M. Pflimlin, "Complementary filter design on the special orthogonal group so (3)", in *Decision and Control, 2005 and 2005 European Control Conference. CDC-ECC'05. 44th IEEE Conference on*, IEEE, 2005, pp. 1477–1484.

[58] (). Igrf, canada, [Online]. Available: `http://geomag.nrcan.gc.ca/calc/mfcal-en.php`.

[59] M.-D. Hua and C. Samson, "Time sub-optimal nonlinear pi and pid controllers applied to longitudinal headway car control", *International Journal of Control*, vol. 84, no. 10, pp. 1717–1728, 2011.

[60] H. Liu, H. Darabi, P. Banerjee, and J. Liu, "Survey of wireless indoor positioning techniques and systems", *IEEE Transactions on Systems, Man, and Cybernetics, Part C (Applications and Reviews)*, vol. 37, no. 6, pp. 1067–1080, 2007.

[61] T. Gigl, G. J. Janssen, V. Dizdarevic, K. Witrisal, and Z. Irahhauten, "Analysis of a uwb indoor positioning system based on received signal strength", in *Positioning, Navigation and Communication, 2007. WPNC'07. 4th Workshop on*, IEEE, 2007, pp. 97–101.

[62] K. El-Kafrawy, M. Youssef, A. El-Keyi, and A. Naguib, "Propagation modeling for accurate indoor wlan rss-based localization", in *Vehicular Technology Conference Fall (VTC 2010-Fall), 2010 IEEE 72nd*, IEEE, 2010, pp. 1–5.

[63] S. Gezici and H. V. Poor, "Position estimation via ultra-wide-band signals", *Proceedings of the IEEE*, vol. 97, no. 2, pp. 386–403, 2009.

[64] Z. Sahinoglu and S. Gezici, "Ranging in the ieee 802.15. 4a standard", in *Wireless and Microwave Technology Conference, 2006. WAMICON'06. IEEE Annual*, IEEE, 2006, pp. 1–5.

[65] D. U. M. Decawave, *2.05*, 2015.

[66] R. B. Langley *et al.*, "Dilution of precision", *GPS world*, vol. 10, no. 5, pp. 52–59, 1999.

[67] (). Dilution of precision, [Online]. Available: https://upload.wikimedia.org/wikipedia/commons/thumb/7/7b/Geometric_Dilution_Of_Precision.svg/1200px-Geometric_Dilution_Of_Precision.svg.png.

[68] T. F. Edgar, D. M. Himmelblau, and L. S. Lasdon, *Optimization of chemical processes*. 2001.

[69] F. A. Potra and S. J. Wright, "Interior-point methods", *Journal of Computational and Applied Mathematics*, vol. 124, no. 1-2, pp. 281–302, 2000.

[70] H. Lim, J. Park, D. Lee, and H. J. Kim, "Build your own quadrotor: Open-source projects on unmanned aerial vehicles", *IEEE Robotics & Automation Magazine*, vol. 19, no. 3, pp. 33–45, 2012.

[71] (), [Online]. Available: http://copter.ardupilot.com/.

[72] (), [Online]. Available: http://3drobotics.com/.

[73] (). Datasheet: Inensense mpu-6000.

[74] (). Datasheet: Hmc5883l, [Online]. Available: http://www.amtel.com/.

[75] (). Rc controller, [Online]. Available: http://www.turnigy9xr.com/.

[76] (). Zigbee wireless transceiver, [Online]. Available: https://www.digi.com/.

[77] (). Dwm1000 uwb module, [Online]. Available: https://www.decawave.com/products/dwm1000-module.

[78] (). Dw1000 datasheet, [Online]. Available: https://www.decawave.com/sites/default/files/resources/dw1000-datasheet-v2.10.pdf.

[79] (). Dwm1000 datasheet, [Online]. Available: https://www.decawave.com/sites/default/files/resources/DWM1000-Datasheet-V1.6.pdf.